POLITECNICO
MILANO 1863

SCUOLA DI INGEGNERIA INDUSTRIALE
E DELL'INFORMAZIONE

Executive Summary of the Thesis

High throughput Time-Domain NIRS device for investigating biological tissues: characterization and first in-vivo tests

Laurea Magistrale in Engineering Physiscs - Ingegneria Fisica

Author: Eliana Colonna

Advisor: Dr. Rebecca Re

Co-advisor: Dr. Lorenzo Spinelli

Academic year: 2020-2021

1. Introduction

Near Infrared Spectroscopy is an efficient technique based on the interaction of light in the range of 600-1000 nm and samples, such as biological tissues, to retrieve their optical coefficients. The latter can be related to the concentration of specific chromophores. In the case of human tissues, the chromophore of interest is the hemoglobin in its two forms: oxygenated (O_2Hb) and deoxygenated (HHb). Continuous wave NIRS (CW-NIRS) is a NIRS regime which is widely used in clinical applications and commercially very spread. It relies on the variation of the light attenuation in order to follow the variation of hemoglobin concentration. However, this modality doesn't provide the capability to retrieve the absolute values of the absorption (μ_a) and scattering (μ_s') coefficients and it is lacking in depth sensitivity. Time domain NIRS (TD-NIRS) overcomes these limitations relying on pulsed light sources and single photon counting detectors. The present work has been conducted on a TD-NIRS device previously developed at Politecnico di Milano. Some modifications have been performed on it to solve some issues resulting in a bad estimation of the optical coefficients. Then, the performances of the new setup have been assessed through standardized protocols and the limits of the machine have been evaluated, along with its operative conditions, by custom made protocols. In particular, the improvement of the device should result in the possibility of sampling at high frequency (>10 Hz) and measure at high source detector distances ($\rho > 3\,cm$), which was not possible with the old setup because of the low S/N at the detectors. A preliminar in-vivo study has been conducted both on the forearm muscles and on the brain cortex to assess the capability of the device.

2. Theoretical background

The pulse entering the surface of the tissue is distorted, delayed and attenuated because of scattering and absorption. To model this interaction, a simplification of the Radiative Transport Equation is used, namely the Diffusion Approximation (DA), valid when the photons undergo multiple scattering in the tissue before being detected. The main condition to be in the DA is to have $\mu_a << \mu_s'$. The theoretical time dependent reflectance curve equation ($R_{th}(\rho, t)$) depends on μ_a and μ_s'.
The experimental reflectance curve ($R_{exp}(\rho, t)$)

is reconstructed thanks to a time correlated single photon counting system (TCSPC). In order to do this, when the laser source emits the light pulse, a reference signal is sent to the board, which receives another signal when the photon arrives at the detector. The delay between the reference signal and the photon arrival is measured and then stored into an histogram of times, based on which the photons distribution of the time of flight (DTOF) is constructed. In the fitting procedure, the μ_a and μ_s' are retrieved in order to minimize the difference between $R_{th}(\rho,t)$ and $R_{exp}(\rho,t)$. The theoretical reflectance curve is the result of the convolution between the solution of the Diffusion Equation for a given geometry and the Instrument Response Function (IRF), which is useful to take into account the non idealities of the instrument. Indeed, in the ideal case, the IRF should be a temporal delta function. Besides the fitting approach, the gating approach can be used to retrieve information about the sample. It relies on the separation of the reflectance curve in temporal windows, called gates, and the analysis the number of photons N arriving in each of them. The photons arriving at late gates have travelled a longer path, thus having more probability to reach deeper positions of the sample. Tasks which involve a physiological response in the tissues under analysis lead to a variation of the absorption coefficient ($\delta\mu_a(\lambda,t)$) with respect to the one related to the baseline reference ($\mu_{a,0}(\lambda,t)$). However, a variation of μ_a can also happen in superficial regions of the biological sample (like the scalp for measurements aimed at studying the hemodynamics in the brain cortex). In order to discriminate the latter from the $\delta\mu_a(\lambda,t)$ happening at the depth of interest, a correction method based on the estimation of the mean partial pathlength travelled by the photons can be performed.

3. TD-NIRS device

Even if a TD-NIRS device was already present in the Department of Physics, its setup has been modified during this thesis work. The previous one presented hardware defeats: the length of the collection bundles and the position of the attenuators disks caused unwanted reflection peaks. The latter were noticeable in the IRF of the system and led to an error in the estimation of μ_a, μ_s'. In order to solve these problems, the attenuation disks of the detector stage have been tilted of $\sim 20°$ and the collection bundles re-designed. To choose the collection bundles, a comparison among graded index (GI) fibers has been performed in terms of efficiency. Given a bundle made of N fibers with core diameter d and length L and section are A, attenuation coefficient α, numerical aperture NA, the efficiency can be computed as follows:

$$\eta = 10^{-\frac{\alpha L}{10}} \pi N A^2 A_{bundle} BPF \tag{1}$$

where BPF is the bundle packing fraction

$$BPF = \frac{N\pi d^2}{4A} \tag{2}$$

The best glass GI fiber bundle in terms of efficiency was compared to the best plastic fiber (POF) one. The features of the best glass fibers were NA=0.24, core/cladding diameter 100/140 μm, attenuation<0.005 dB/m at 800 nm. The features of the best POF were NA=0.3, core/cladding 0.9/1 mm, attenuation <0.2 dB/m (<2 dB/m) 600 nm (800 nm). Comparing configurations that resulted in the same overall diameter of the bundle (3 mm), the simulations have revealed the POF fibers to be more efficient for the red light for optical bundles up to 10 m length. For the IR light, instead, the POF fibers are more efficient with respect to the glass fibers until a length of 1.5 m, due to the higher coefficient of attenuation with respect to the glass fibers. Since to avoid reflection peaks in the IRF the length has to be an integer multiple of 1.25 m, the final bundles have been built with 7 POF fibers leading to a total cross section of 3 mm and 1.25 length. Due to the changes of the collection bundles, the whole system of probes for the interface with the sample have been re-designed during this work as well. Thus, after the modifications the device under analysis is constituted by two laser sources of wavelengths 689±1 nm and 828±1 nm (LDH-P-C PicoQuant GmbH, Berlin, Germany), minimum width 72 ad 96 ps and pulse rate 80 MHz. They are coupled into a step index glass fiber with core/cladding ratio 600/660 μm. After an attenuation stage they are coupled to an optical combiner which delays the IR pulse with respect to the red one. Then, another glass index fiber with the same characteristics as the

one presented before, brings the pulses to the sample. Four graded index plastic fibers bundles collect the pulse from the sample and bring it to the detection stage, composed by a cooled hybrid PMT tube which delivers the electrical signal to the device that performs the TCSPC process.

4. Performance assessment

The performances of the instrument have been assessed through international standardized protocols, such as Basic Instrument Performance (BIP), MEDPHOT and nEUROPt. Custom made protocols have been realized to assess the limits of the instruments in terms of count rate, acquisition time, interfiber distance. It worth remarking that the power arriving at the sample considering a 1.25 m injection fiber is 1.91 mW and 7.94 mW respectively for red and IR.

BIP protocol

The aim of this protocol is to assess the basic performances of the only instrument regardless of the interaction with the sample. First of all the IRF has been evaluated to determine whether the problems of the previous setup were fixed. An important parameter of the IRF is its full width at half maximum (FWHM) since it characterizes the time resolution of the instrument as a whole[1]. The average value of the FWHM for the four channels is $241 \pm 10ps$ for the red pulse and $236 \pm 11ps$ for the IR one. This constitutes an improvement with respect to the old setup of the device. Indeed, before the modifications, the average value for the red and IR pulse was, respectively, $401 \pm 25ps$ and $362 \pm 32ps$.

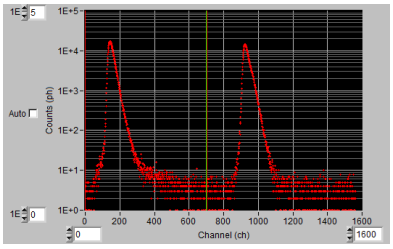

Figure 1: IRF of the instrument. The left peak curve is referred to 690 nm, the right one to 830 nm

Figure 1 shows the red (left) and IR (right) peaks and no undesired reflections are present, thus revealing the effectiveness of the new bundles and position of the attenuators. The responsivity parameter gives information about the magnitude of the measured signal when impinging on a target with a certain number of photons. For this device, the responsivity is in the same order of magnitude of other time domain systems based on hybrid PMT: $10^{-8}m^2sr$. Ideally, each of the channels of the TCSPC system should have the same width: otherwise, this would lead to a variability in the number of collected photons. This feature is assessed through a parameter called Differential Non Linearity (DNL). The values of DNL for the 4 detection channels don't exceed the 7%, an acceptable value that indicates that the channels are uniform among them and thus they don't create any distortion to the DTOF. Another parameter to take into account is the afterpulsing ratio, caused by the emission of positive ions by the PMT few ms after the single-photon pulse. No significative aterpulsing ratio values are found for the device under analysis.

Operating conditions

The rule of thumb to be in the single-photons counting statistics is to keep the detection rate at about 5% of the emitting pulse rate. To evaluate the effective maximum count rate to be in the single photon statistics, a custom measure has been performed. The result of the analysis has provided $8 \cdot 10^6$ counts/s on the total board to have an error $<3\%$ in the estimation of μ_a and μ_s' with respect to the ones retrieved for low count rates (from 0.5 to 4 million counts/s), where the single photons statistics is surely applicable.

The state of the art devices allow a maximum sampling rate of 10 Hz, thus overcoming this limitation would constitute a novelty for the TD-NIRS device under analysis. Decreasing the duration of an acquisition, a smaller number of photons is collected to retrieve the DTOF, thus this curve is affected by a variability due to the noise. The measure is said to be consistent when the coefficient of variation (CV), which is the ratio between the standard deviation of the data and their average value, is $<1\%$. The characterization of the instrument under analysis showed that the minimum acquisition time can be pushed to 50 ms if the count rate is set to $7 \cdot 10^6$ photons/s on the board. This allows to push the sampling frequency up to 20 Hz and

to overcome the sampling frequency of the state of the art device.

MEDPHOT protocol

The MEDPHOT protocol has been designed in order to validate the performaces of photons migration instruments on the basis of the quality of the measurands μ_a and μ_s' [2]. Noise, linearity, accuracy, stability and reproducibility are the evaluated features. All of them have been assessed for a configuration having $\rho = 3\,cm$. Noise assessment is useful to determine, according to the CV value, the minimum count rate for a correct estimation of the optical coefficients. In the case under analysis, to have a CV<1%, 10^5 counts/s on the board are required.

The reproducibility of the instrument has been evaluated through four days. Both the absorption and scattering coefficients don't differ from the average value of the four days more than a 3% factor.

To retrieve stable values of μ_a and μ_s', instead, a warm-up of 125 minutes after turning the instrument on is required. The linearity and accuracy assessments have been made through a set of 32 phantoms labeled from A to D and from 1 to 8 according to their values of reduced scattering and absorption coefficients. Phantoms from A to D span, with steps of 5 cm^{-1}, μ_s' values from 5 to 20 cm^{-1}. Phantoms from 1 to 8 span, with steps of 0.7 cm^{-1}, μ_a values from 0 to 0.49 cm^{-1}. The latter values are referred to 660 nm and will be indicated as nominal. The μ_a and μ_s' referred to 690 nm and 830 nm have been retrieved for a subset of phantoms by another TD-NIRS device (IRF width 200 ps) of the Department of Physics and they will be called conventional. The system shows no coupling effects between the values of μ_a and μ_s' and it has been shown that it is capable to linearly follow linear variations of the optical coefficients. The accuracy has been assessed comparing the values of the optical coefficients retrieved by the TD-NIRS device under analysis with the conventional ones. The latter are not available for the whole set of phantoms. However, the values of the optical indexes for the B series are available and, since this series contains the phantoms which mimics the optical properties of the biological tissues ($\mu_a \sim 0.1\,cm^{-1}$ and $\mu_s' \sim 10\,cm^{-1}$) the relative errors for 690 nm and 830 nm are displayed in table 1 for scattering and absorption.

ϵ(%)						
	B2	B3	B4	B5	B6	B7
$\mu_{a,690}$	-6.2	-5.8	-6.4	-6.2	-6.3	-6.7
$\mu_{a,830}$	-6.3	-4.3	-2.3	0.5	0.5	6.7
$\mu_{s',690}$	-8.6	-13.5	-13.8	-16.9	-16.7	-20.6
$\mu_{s',830}$	-10.0	-13.5	-11.5	-13.9	-11.8	-14.5

Table 1: Relative errors of the measured μ_a and μ_s' at 690 nm and 830 nm with respect to the conventional ones.

Besides the B series, phantoms A2, C2, D2 and D8 have been also characterized. Hence, to give an hint of the accuracy of the total set of phantom, an assumption has been necessary: the scattering coefficient respectively of A2, C2 and D2 has been extended to all the phantom of the corresponding series (A, C, D) and the absorption coefficient of the phantoms from B1 to B8 has been extended to the missing values of the other series from 1 to 8 (e.g. all the phantoms labeled with 1 have been assumed with the same μ_a as B1). The values of accuracy for the entire set of phantoms don't exceed 10% for μ_a and 20% for μ_s'.

Further interfiber distances

As previously mentioned, the minimum number of photons that have to be detected for a correct reconstruction of the optical coefficients is 10^5 photons/s. All the measurements for the MEDPHOT characterization have been performed at $\rho = 3cm$, but, during this thesis project, the capability of having a count rate high enough for the correct estimation for μ_a and μ_s' has been assessed also for higher interfiber distances. Namely, the count rate has been found to be $> 10^5$ for the phantoms from B1 to B6 at $\rho = 4\,cm$ and from B1 to B4 for $\rho = 5\,cm$. Even if the B series is not entirely characterizable by the TD-NIRS instrument at high interfiber distances, the count rate is sufficient for the phantoms that mimic the optical properties of the human tissues (B2, B3). For $\rho = 1\,cm$ and $\rho = 2\,cm$, the minimum count rate is reached with any of the phantoms of the set. A comparison has been made between the optical coefficients retrieved with the interfiber distances from 1 to 5 cm and the conventional values of μ_a and μ_s'. The order of magnitude of the errors is kept under 10% for μ_a and under 20% for μ_s'.

nEUROPt protocol

The most powerful capability of a TD-NIRS instrument is the one to be able to detect, localize and measure the variation of the absorption

coefficient in the human tissues under analysis [3]. To mimic the variation of absorption in a medium, a liquid phantom is used along with a black inclusion used to simulate the perturbation of μ_a. For the characterization of this TD-NIRS instrument capability to detect the change in the absorption value, the attention has been focused on the number of collected photons N and its variation according to the position of the inclusion with respect to the source and detector fibers. The contrast is proportional to the ratio between $N(z)$ and N_0, which is the number of photons arriving at the detector when the inclusion is far enough to consider the phantom homogeneous.

$$C(z) = -\ln \frac{N(z)}{N_0} \tag{3}$$

For the analysis of the data, the gating approach has been used.

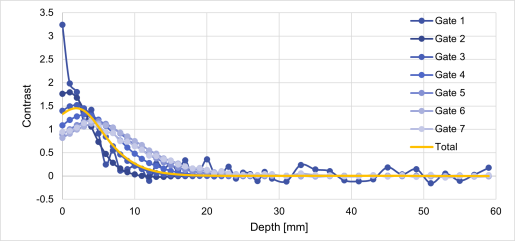

Figure 2: Example of contrast for ρ=3cm. The blue curves represent the contrast for each of the chosen time gates. The yellow curve, instead, represents the contrast computed on a single large gate covering the same time window of the sum of the narrower 7.

Figure 2 is an example of contrast referred to a $500\,mm^3$ inclusion ($\Delta\mu_a = 0.094mm^{-1}$) retrieved at $\rho = 3\,cm$ for 7 different temporal gates of 500 ps width. The yellow curve represents a single gate spanning all the time window that the sum of the 7 gates span. It has been displayed in order to make visible the enhancement offered in the time gating approach. The higher order gates see a non null contrast for higher depths of the black volume than the single gate case.
Late gates refer to photons with a longer time of flight than the ones collected in the early gates. Traveling for a longer path, these photons have more probability to reach higher depths in the sample, thus reporting the presence of deep absorbing objects. In figure 3 this is visible focusing on the depth where the contrast curve settles to 0. The orange curve of the gate 3, for example, shows a null value of contrast from about 15 mm depth, then this depth increases respectively to about 20 and 25 mm for the gates 5 and 7.

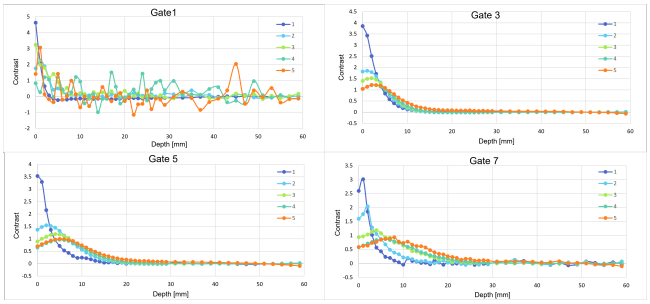

Figure 3: Different gates at all the inter fiber distances.

If the attention is focused on a single gate, for example GATE 3, where none of the curves is noisy, it can be seen that for small depths, the ρ equal to 1 and 2 cm show a better contrast than the bigger ones, while the curves obtained at 4 and 5 cm decay more slowly to 0 going to the increasing direction of the depth axis. Thus, the sensitivity up to 2.5 cm depth is enhanced thanks to the longer ρ configuration that can be used in this TD-NIRS instrument.

5. In-vivo measurements

To assess the capability of the TD-NIRS instrument of following the hemodynamics in real tissues, preliminary measurements have been conducted on a volunteer of the Department of Physics of Politecnico di Milano: an occlusion on the forearm muscle and a motor task to follow the hemodynamics in the brain cortex. For the measurements, the four detectors of the system have been placed to four different distances from the source: from 2 to 5 cm. The sampling rate has been fixed to 20 Hz.
The occlusion protocol consisted in 120 s of baseline acquisition, 180 s of cuff occlusion at a pressure of 250 mmHg and 300 s recovery.

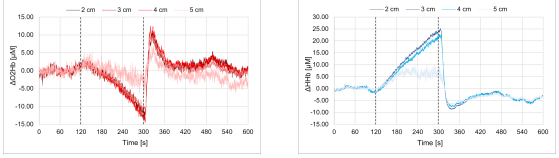

Figure 4: Variations of O_2Hb and HHb with respect to the baseline during the cuff occlusion.

The variation of O_2Hb and HHb (with respect

to the baseline value) related to the occlusion is shown in figure 4. As expected, during occlusion the arterial (venous) blood entrance (exit) in the tissue is inhibited resulting in an decreasing (increasing) of O_2Hb (HHb). All the channels placed at the different interfiber distances are capable of following this trend. As can be seen from figures 4, the detection channel at 5 cm detects a lower variation in the parameters with respect to the other one: placing the detector at high distances from the source increases the probability that the photons have traveled for a longer path and thus have reached an higher depth in the tissue. An ecography imaging performed on the arm, showed the overlapping of different muscles in the position of the probe. This could be the explanation of the different behaviour at higher ρ: the probability to "notice" the underlying muscles is higher at 5 cm. The protocol of the measure performed on the brain (left hemisphere) consisted of 5 repetitions of 20 s baseline, 20 s finger tapping with the right hand, 20 s recovery. For the data analysis, the correction based on the MPP estimation has been applied, in order to discriminate $\delta\mu_a$ in the brain cortex from the one in the superficial layer (1 cm thick) of the head.

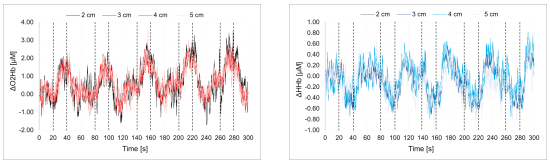

Figure 5: Variations of O_2Hb and HHb with respect to the baseline in the left hemisphere of the brain cortex during motor task performed with the right hand.

Figure 5 left and right show respectively an increase of the O_2Hb concentration in the finger tapping period and a correspondent decrease of HHb. In the time before the exercise the values oscillate around the baseline value, in the time after the exercise the parameters take around 20 s to go back to the 0 variation level. The curves retrieved at all the interfiber distances are well overlapped,thus the TD-NIRS device is capable of consistently retrieve the optical parameters even at long source detector distances. Long baseline acquisitions have been performed both in the arm muscle and in the brain during the resting state. They show, among others, low frequency oscillations, with period of the order of 100 s. Other techniques, such as MRI or electroencephalographic scalp recording have already detected these kinds of low frequency oscillations (LFOs). It has been shown that they give important hints on some physiological parameters that can be studied and related to particular pathologies, such as defeats of the brain autoregulation. This suggests that the present TD-NIRS device, thanks to its large range of sampling frequency, could be a useful tool to study the spectrum of the oscillations.

6. Conclusions

The present study has shown the capability of the TD-NIRS instrument to perform acquisitions at frequencies up to 20 Hz and with an interfiber distance up to 5 cm, overcoming the limits of the state of art. Promising results for the in-vivo measurements have been provided. In the future it might be interesting to have a consistent set of in-vivo measurements to perform an analysis of the spectrum of the oscillations and assess the LFOs.

References

[1] H. Wabnitz, D. R. Taubert, M. Mazurenka, O. Steinkellner, A. Jelzow, R. Macdonald, D. Milej, P. Sawosz, M. Kacprzak, A. Liebert, R. Cooper, J. Hebden, A. Pifferi, A. Farina, I. Bargigia, D. Contini, M. Caffini, L. Zucchelli, L. Spinelli, R. Cubeddu, and A. Torricelli. Performance assessment of time-domain optical brain imagers, part 1: basic instrumental performance protocol. *Journal of Biomedical Optics*, 19(8):1 – 12, 2014. doi: 10.1117/1.JBO.19.8.086010. URL `https://doi.org/10.1117/1.JBO.19.8.086010`.

[2] A. Pifferi A. Torricelli R. Cubeddu H. Wabnitz D. Grosenick M. Möller R. Macdonald J. Swartling T. Svensson S. Andersson-Engels R. L. P. van Veen Henricus J. C. M. Sterenborg J.-M. Tualle H. L. Nghiem S. Avrillier M. Whelan A. Bassi, P. Taroni and H. Stamm. Performance assessment of photon migration instruments: the medphot protocol. *Appl. Opt. 44*, pages 2104–2114, 2005.

[3] H. Wabnitz, A.Jelzow, M. Mazurenka, O. Steinkellner, R. Macdonald, D. Milej, N. Żołek, M. Kacprzak, P. Sawosz, R.Maniewski, A. Liebert, S. Magazov, J. C. Hebden, F. Martelli, P. Di Ninni, G. Zaccanti, A. Torricelli, D. Contini, R. Re, L. M. Zucchelli, L. Spinelli, R. Cubeddu, and A. Pifferi. Performance assessment of time-domain optical brain imagers, part 2: nEUROPt protocol. *Journal of Biomedical Optics*, 19(8):1 – 12, 2014. doi: 10.1117/1.JBO.19.8.086012. URL `https://doi.org/10.1117/1.JBO.19.8.086012`.

POLITECNICO
MILANO 1863

SCUOLA DI INGEGNERIA INDUSTRIALE
E DELL'INFORMAZIONE

High throughput Time-Domain NIRS device for investigating biological tissues: characterization and first in-vivo tests

Tesi di Laurea Magistrale in
Engineering Physics- Ingegneria Fisica

Author: **Eliana Colonna**

Student ID: 944688
Advisor: Dr. Rebecca Re
Co-advisors: Dr. Lorenzo Spinelli
Academic Year: 2020-21

Abstract

This experimental master thesis is based on the Time Domain Near Infrared Spectroscopy (TD-NIRS) technique, which exploits the distribution of the time of flight of the photons after the interaction of a short (tens of ps) light pulse with a biological tissue to retrieve its optical properties (μ_a and μ'_s). As a consequence, it makes possible to determine the absolute values and the changes of concentration of specific chromophores, which are useful tools for the non-invasive access to important physiological information.
The work has been conducted on a high power TD-NIRS device previously developed at Politecnico di Milano with one injection and four detection channels. Its hardware presented some defects that resulted in bad performances of the device, especially in the estimation of the absolute values of the optical coefficients. Thus, it has been modified during this thesis work to correctly determine the absorption and reduced scattering coefficients at source detector distances spanning from 1 to 5 cm and at acquisition frequencies up to 20 Hz, overcoming the capabilities of the state of art devices.
Specifically, at first the principle and theoretical concept that constitute the basis of the technique are provided, along with the theory on which the data analysis is based. Then, the instrument is described in detail, with a special focus on the hardware modifications. The validation of the new setup is provided through the implementation of standard international protocols for diffuse optical instruments: BIP, MEDPHOT and nEUROPt. Through custom made protocols, instead, the limits and the operative conditions of the device are assessed. An example of in-vivo measurement is shown to highlight the capability of the new device to follow the hemodynamics in the brain cortex, as a consequence of a motor stimulation, and in a muscle during a cuff occlusion. Details of the measurements setup and modalities are provided along with promising results and future perspectives.

Keywords: TD-NIRS, hemodynamics, optical properties, functional near infrared spectroscopy, brain cortex, muscle oxydative metabolism.

Abstract in lingua italiana

La presente tesi sperimentale di Laurea Magistrale si basa sulla tecnica di spettroscopia nel vicino infrarosso risolta nel tempo (TD-NIRS), la quale sfrutta la distribuzione del tempo di volo dei fotoni dopo l'interazione di un impulso di luce corto (decine di ps) con un campione, per ricavarne le proprietà ottiche (μ_a e μ'_s). Di conseguenza, la tecnica permette di determinare i valori assoluti e le variazioni delle concentrazioni di specifici cromofori. Nel caso di tessuti biologici, questi ultimi sono utili per accedere in modo non invasivo ad importanti informazioni fisiologiche.
Il lavoro è stato condotto su uno strumento TD-NIRS ad alta potenza precedentemente sviluppato presso il Politecnico di Milano. L'hardware di quest'ultimo presentava alcuni difetti che limitavano la qualità delle sue prestazioni, in particolare la capacità di avere una stima esatta dei valori assoluti dei parametri ottici. Lo strumento, quindi, è stato modificato per ricavare correttamente μ_a e μ'_s a distanza sorgente-detector da 1 a 5 cm e a frequenze di acquisizione fino a 20 Hz, superando le capacità dei dispositivi TD-NIRS esistenti.
Nello specifico, in questa tesi sono forniti i principi teorici alla base della tecnica e dell'analisi dei dati. Lo strumento è poi descritto nel dettaglio, con una particolare attenzione alle modifiche effettuate sull'hardware. La validazione del nuovo setup è realizzata tramite protocolli internazionali standardizzati: BIP, MEDPHOT e nEUROPt. Le condizioni operative e i limiti del dispositivo, invece, sono valutati attraverso protocolli su misura. Una campagna di misure in vivo è stata realizzata per mostrare la capacità del nuovo strumento di seguire l'emodinamica nella corteccia cerebrale e nel tessuto muscolare rispettivamente in seguito ad una stimolazione motoria e un'occlusione arteriosa. Tutti i dettagli relativi a setup, modalità di misura e risultati saranno mostrati con le conseguenti prospettive future.

Parole chiave: TD-NIRS, emodinamica, proprietà ottiche, spettroscopia funzionale nel vicino infrarosso, corteccia cerebrale, metabolismo ossidativo del muscolo.

Contents

Introduction

During the past few decades, non-invasive optical techniques based on diffuse optics have gained the attention of the scientific community. Near Infrared Spectroscopy (NIRS) is one of the most exploited techniques in order to retrieve the optical properties of biological tissues. It relies on the wavelength specific absorption of light (in the range of 600-1000mm) by the chromophores of the tissues under analysis. Among them, hemoglobin is present in two different species: oxygenated (O_2Hb) and deoxygenated (HHb). Continuous wave NIRS (CW-NIRS), widely used in clinical applications thanks to its operative simplicity, exploits the variation of attenuation of light to retrieve changes in the absorption coefficient and, thus, of changes in hemoglobin concentration. However, this modality doesn't provide the capability to retrieve the absolute values of the absorption and scattering coefficients and doesn't present a depth sensitivity, i.e. the ability to distinguish the signal coming from different depths of the sample. Time domain NIRS (TD-NIRS) modality employs pulsed light sources and single photons detectors allowing to overcome the limitations of CW-NIRS. However, even if recent publications showed successful clinical studies performed through TD-NIRS instruments, their popularity has been hindered by their complexity, so they are still mainly used in the research field and less commercially diffused than CW-NIRS devices. The objective of the present work is the improvement of a high power TD-NIRS device previously developed in the Department of Physiscs of Politecnico di Milano. It is based on high power laser sources (in the order of tens of mW) emitting at 690 nm (red) and 830 nm (IR), hybrid photomultipliers and time correlated single photon counting boards for the acquisition. The characterization of the old setup has shown some hardware drawbacks which resulted in the bad estimation of the absorption and reduced scattering coefficients absolute values. They were visible in the Instrument Response Function (IRF) curve, which gives information about how the pulses exiting from the laser heads are widened or distorted travelling in the components of the device. In the old setup, the IRF presented some unwanted reflection peaks next to the main ones corresponding to the red and IR pulse.

The present work is aimed at overcoming the technological limitations of the old setup in order to get a good estimation of the optical coefficients. The effectiveness of the hardware

improvements is evaluated by standard international protocols. Another purpose is to assess the capability of the device under analysis to perform acquisitions at high source-detector distances (until 5 cm), which is the technological novelty of the instrument. Moreover, since the state of the art devices have a maximum frequency of acquisition of 10 Hz, overcoming this limit is another goal of the instrument.

In the first chapter the theoretical basis of the TD-NIRS technique, its working principle relying on the single photon counting detection system and the methods used for the analysis of the acquired data will be described. A method based on time-domain contrast functions and another one based on the estimation of the mean partial pathlength traveled by the photons will be presented: they consitute the key of the increased depth selectivity which is the main advantage of the TD-NIRS.
In the second chapter, a description of the device and its modifications will be provided as well as the process that has lead to the choice of the new components of the device: the collection bundles and, consequently, the probes set. Namely, collection bundles made by graded index fibers of different materials (plastic and glass) will be compared in order to make the best choice in terms of efficiency and dispersion. The probes constitute the interface between the sample and the optical fibers of injection and collection, thus, after changing the design of the latter, it has been necessary to re-design the set of probes for on-phantom and in-vivo measurements. The effectiveness of the improvements will be evaluated in the third chapter through the application of three standard protocols: BIP, MEDPHOT and nEUROPt. To assess the capability of the instrument of performing acquisitions at high frequency and at high interfiber distances, which are the features that make the instrument innovative, custom made protocols will be also shown. Finally, in the last chapter, the results of a preliminar in-vivo study performed on a single subject will be shown, to give an hint of the capabilities of the new device and show what are the related future perspectives.

1 | The TD-NIRS technique

The Near Infrared Spectroscopy (NIRS) is a non-invasive technique used in different fields with the goal of performing a non-destructive analysis of different samples, such as liquids, powders or bulk objects. In the biomedical domain, it is used to test biological samples in order to follow their hemodynamics and monitor their oxidative metabolism. It relies on the fact that light in the range of 600-1000 nm can penetrate deep (in the order of few centimeters) in the tissues and interact with the chromophores that constitute it, determining the change of path followed by the photons caused by scattering and the light attenuation caused by absorption events. The parameters that NIRS is aimed to extract by the study of the optical properties of biological tissues are the concentration of HHb, O_2Hb, tHb, respectively the deoxygenated, oxygenated and total hemoglobin and the tissue oxygen saturation SO_2. The term fNIRS (functional Near Infrared Spectroscopy) is used when the technique is aimed at studying the response of the human brain cortex to specific tasks or following its activity [1].

Three different operating principles are used for the practical applications of NIRS: Continuous wave (CW), FD (Frequency-Domain) and TD (Time-Domain). The present thesis work is based on the last modality, which is the most complex in terms of operating principles and instrumentation, but which has a depth sensitivity independent on the source-detector distance and which is capable of retrieving, even with a single channel, the absolute values of the concentration of the chromophores. Thus it will be the one to be further explained.

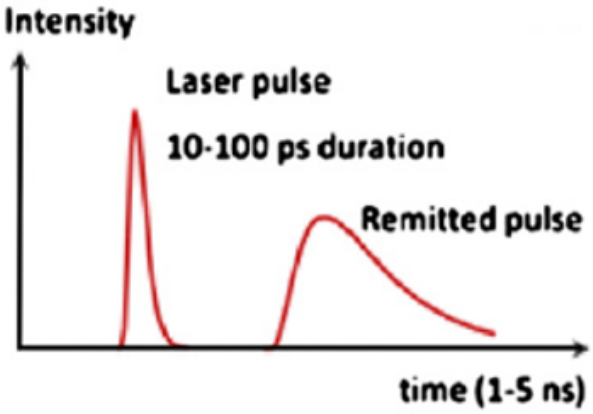

Figure 1.1: Effect of dispersion and attenuation on the original laser pulse [1].

In TD-NIRS, a short light pulse (tens of picoseconds) is injected in the tissue under analysis. Photons interact with the chromophores being scattered and absorbed and then they spread along different directions and reach different depths in the tissue, thus resulting in the broadening, delay and attenuation of the original pulse (fig. 1.1).
To quantify these effects, the Distribution of the Time of Flight (DTOF) of the photons, also known as Temporal Point Spread Function (TPSF), is analysed. The TPSF is retrieved by the histogram of the arrival time of the photons. More details about the latter will be given in section 1.2.1.

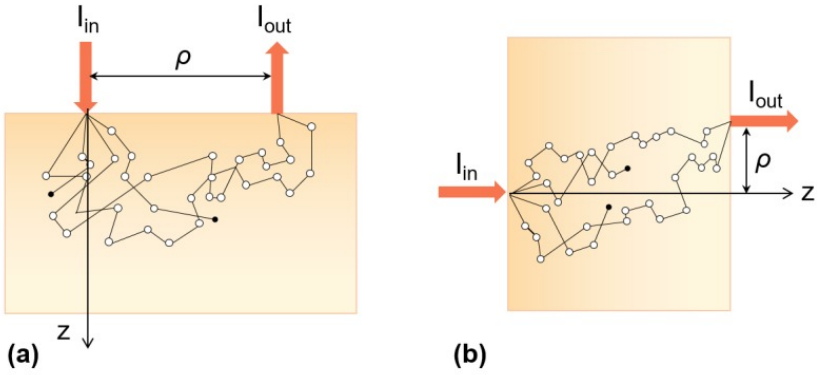

Figure 1.2: Scheme of the reflectance (a) and transmittance (b) modality. The black points represent the absorbers, while the white ones represents the scatterers. ρ is the source-detector distance [2].

The light outcoming from the sample can be collected from a point located in the same surface of injection (fig. 1.2 (a)): this is the case of measurement in refectance mode.

Another alternative is to collect the photons in a point of a surface located at the opposite side of the injection one: this mode is called transmittance mode (fig. 1.2 (b)).

1.1. Theoretical principles

In this section, the theory of scattering and absorption will be presented, then the photon migration in the biological samples will be described through a simplification of the Radative Transport Equation (RTE) and some simulations performed on the basis of the theory will be shown in order to underline the effects of scattering, absorption and measurement configurations in the DTOF.

1.1.1. Absorption

Biological tissues can be modeled as turbid media: they are composed by a background medium in which are dispersed more particles with different refractive index, a specific absorption band and a specific absorption cross section, which determines the amount of power which is absorbed for a given intensity of the incident radiation.
If we assume to have identical absorbers with a concentration τ and a given cross-section σ_a, the absorption coefficient can be defined as:

$$\mu_a = \tau\sigma_a \tag{1.1}$$

This quantity can be linked to the concentration c of a certain chromophore in the following way:

$$\mu_a(\lambda) = \epsilon(\lambda)c \tag{1.2}$$

where $\epsilon(\lambda)$ is the known wavelength dependent molar extinction coefficient [3], related to the capability of the given species to absorb photons.
The absorption effects come from the interaction of light both with the molecules of the background and the dispersed particles.
An absorption mean free path can be defined $l_a = 1/\mu_a$: it is the mean path traveled by a photon before undergoing an absorption event.

1.1.2. Scattering

The heterogeneity of the refractive index inside a medium is due mainly to:

- the presence of dispersed particles with different refractive indexes with respect to the background;

- the fluctuations of the density of the background's constituents.

This heterogeneity determines multiple changes of direction in the path of the photons before arriving at the detectors. Usually, when multiple scattering dominate the propagation of light, the effects of the background's density fluctuation is ignored [4]. If, after the scattering event, the photon preserves its initial energy, the event is called elastic scattering, otherwise it is inelastic. In the frame of photons interacting with the particles of biological tissues, it worth focusing on elastic (or Rayleigh) scattering events. As for the absorption case, the scattering coefficient can be defined as:

$$\mu_s = \gamma\sigma_s \tag{1.3}$$

where γ is the concentration of the scattering particles and σ_s the scattering cross section. In analogy to what has been said for the absorption cross section, the scattering cross section is defined as the ratio between the amount of power that is scattered over the intensity of the incident radiation.
The scattering mean free path can be defined as the length traveled by the photon before being scattered $l_s = 1/\mu_s$.
Besides being described by the μ_s, the scattering processes are also described by the scattering phase function $p(\hat{s}, \hat{s}')$, which is the probability that a photon travelling along a direction $\hat{s}$ is scattered within the solid angle along the direction $\hat{s}'$. In case of having isotropic scattering, the p function only depends on the angle θ between the two directions, hence:

$$p(\hat{s}, \hat{s}') = p(\theta) \tag{1.4}$$

Moreover, when the propagation is dominated by multiple scattering, the g factor can be defined:

$$g =< cos\theta >= 2\pi \int_0^{\pi} cos\theta p(\theta) sin\theta d\theta \tag{1.5}$$

It has been proven that for photons emitted in an infinite non-absorbing homogeneous medium at z=0, given k the order of the scattering event along the z axis (perpendicular to the surface of injection) and z_k the position where the k-th scattering event occurs, the following relation holds:

$$\lim_{k->\infty} < z_k >= \frac{1}{\mu_s}\frac{1}{1-g} \tag{1.6}$$

The previous limit can be seen as a mean free path

$$l_s = \frac{1}{\mu_s(1-g)} \tag{1.7}$$

defined as the inverse of a new optical coefficient. Thus, the reduced scattering coefficient can be defined as:

$$\mu_s' = \mu_s(1-g) \tag{1.8}$$

The size r of the scatterers of the biological tissues is such that $r >> \lambda$ for the near infrared domain. For these kind of particles, $p(\theta = 0) \sim 1$, thus leading to a negligible value of the factor g. In this case, μ_s' becomes an important parameter to describe the scattering properties of the medium [4].

1.1.3. Optical properties of human tissues

Hemoglobin is one of the most present chromophores in the human brain cortex and muscular tissues. Its oxygenation changes according to the task performed by the human brain or to the activity of the muscles. It's possible to keep track of the changes in the concentration of oxygenated and deoxygenated hemoglobin, i.e. following the hemodynamics of the tissue, through their absorption properties.

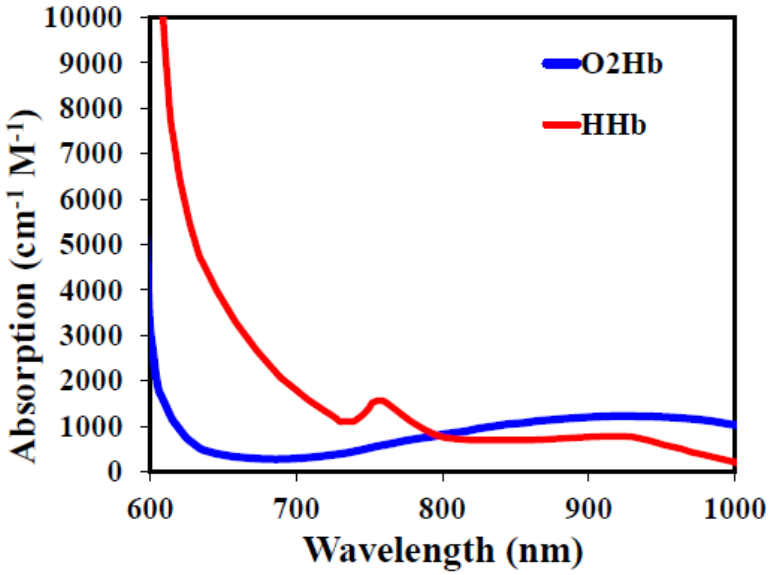

Figure 1.3: Absorption spectra of HHb (red) and O_2Hb (blue). The point where the two curves intersect is called isosbestic point [5].

TD-NIRS technique operates at two wavelengths in the near infrared domain in order to exploit the differences between the absorption spectra of the oxygenated and deoxygenated hemoglobine (fig.1.3). The wavelengths of the chosen sources must be around the isosbestic point (800 nm). The dependence of the concentration of the two specimen on

their λ dependent absorption features can be found starting from eq. 1.2. It is shown in the following relations:

$$\begin{aligned} c_{O_2Hb} &= \frac{\mu_a(\lambda_1)\epsilon_{HHb}(\lambda_2) - \mu_a(\lambda_2)\epsilon_{HHb}(\lambda_1)}{\epsilon_{O_2Hb}(\lambda_1)\epsilon_{O_{HHb}}(\lambda_2) - \epsilon_{O_2Hb}(\lambda_2)\epsilon_{O_{HHb}}(\lambda_1)} \\ c_{HHb} &= \frac{\mu_a(\lambda_2)\epsilon_{O_2Hb}(\lambda_1) - \mu_a(\lambda_1)\epsilon_{O_2Hb}(\lambda_2)}{\epsilon_{O_2Hb}(\lambda_1)\epsilon_{O_{HHb}}(\lambda_2) - \epsilon_{O_2Hb}(\lambda_2)\epsilon_{O_{HHb}}(\lambda_1)} \end{aligned} \tag{1.9}$$

From the values of the concentration of O_2Hb and HHb, the total hemoglobin concentration and the saturation of the tissue can be defined as:

$$c_{tHb} = c_{O_2Hb} + c_{HHb} \tag{1.10}$$

$$SO_2 = \frac{c_{O_2Hb}}{c_{tHb}} \cdot 100 \tag{1.11}$$

The advantage of the TD-NIRS technique is the possibility to retrieve the absolute values of absorption, scattering coefficients and path length of the photons, thus the absolute values of the previously mentioned concentrations. For the other techniques, instead, it's impossible or difficult to retrieve the absolute values and the only possibility is to to detect changes of these quantities [6].

1.1.4. The theory of light propagation in turbid media: RTE and DA approach

The theory on which NIRS is based is the Radiative Transport Equation (RTE), which is basically a balance of energy performed between the variation of the intensity per unit time, per unit of solid angle ad unit of area normal to a certain $\hat{s}$ direction and the variation of intensity due to absorption and scattering events. The resulting equation for the time dependent case is the following one:

$$\frac{1}{v}\frac{\delta}{\delta t}I(\vec{r},t,\hat{s}) + \nabla \cdot [\hat{s}I(\vec{r},t,\hat{s})] + (\mu_t)I(\vec{r},t,\hat{s}) = \mu_s \int_{4\pi} p(\hat{s},\hat{s}')I(\vec{r},t,\hat{s})d\Omega' + \epsilon(\vec{r},t,\hat{s}) \tag{1.12}$$

where v is the speed of light in the medium, μ_t is the sum of the absorption and scattering coefficient, $\epsilon(\vec{r},t,\hat{s})$ is the source and $p(\hat{s},\hat{s}')$ is the probability of a photon moving along the direction $\hat{s}$ to be scattered in the direction $\hat{s}'$. It can be solved first removing the

dependence on the absorption, thus finding the solution for the case of an homogeneous medium with the source term described by a temporal Dirac delta function

$$I(\vec{r}, t, \hat{s})|_{\mu_a=0} \tag{1.13}$$

and then taking into account the μ_a dependence through the Lambert-Beer law.

$$I(\vec{r}, t, \hat{s}) = I(\vec{r}, t, \hat{s})|_{\mu_a=0}\, exp(-\mu_a v t) \tag{1.14}$$

Due to the complexity of the equation, the only way to solve it is via numerical methods or simplifying it through some analytical approximations.
Among them, the most used one for the highly diffusive media, i.e. the media where the photons undergo multiple scattering events, is the Diffusion Approximation. Since absorption would extinguish photons with a long path, thus obstructing the multiple scattering, this approximation is valid only in media where the absorption coefficient is much smaller than the reduced scattering one.
In this frame, the intensity can be assumed to be almost isotropic, thus it can be approximated through the first two terms of the Taylor expansion in terms of the power of $\hat{s}' \cdot \hat{s}$ hence:

$$I(\vec{r}, t, \hat{s}) = \frac{1}{4\pi} \int_{4\pi} I(\vec{r}, t, \hat{s}')\, d\omega + \frac{3}{4\pi} \int_{4\pi} I(\vec{r}, t, \hat{s}') \hat{s}'\, d\omega \cdot \hat{s} \tag{1.15}$$

where the first integral represents the average diffuse intensity (U_d) and the second one represents the diffuse flux vector (F_d).
The other assumptions made to solve eq. 1.12 in the frame of the Diffusive Approximation are:

- the term $p(\hat{s}, \hat{s}')$ is only dependent on the scalar product of the two vectors;
- the variation of the diffuse flux vector is negligible over a length $1/\mu_s'$, namely between two scattering events, with respect to the vector itself.

The previous stated conditions are the true since scattering events tend to randomize the direction of propagation. So, in the diffusion approximation, where the relation $\mu_a << \mu_s'$ holds, they are verified.

As shown in [7], after making these assumptions and then integrating over the solid angle the RTE multiplied by $\hat{s}$, one obtains the Fick's law:

$$F_d(\vec{r}, t) = -4\pi D \nabla U_d(\vec{r}, t) \tag{1.16}$$

and the Diffusion Equation (DE) for an homogeneous infinite non absorbing medium:

$$\left(\frac{1}{v}\frac{\delta}{\delta t} - D\nabla^2\right) U_d(\vec{r},t) = Q(\vec{r},t) \tag{1.17}$$

where D is the diffusion coefficient, generally defined as:

$$D = \frac{1}{3(\mu_a + \mu_s')} \tag{1.18}$$

and that becomes

$$D = \frac{1}{3\mu_s'} \tag{1.19}$$

in diffusive regime (where the scattering is predominant on absorption) and $Q(\vec{r},t)$ is the isotropic source term.
The solution of the DE in a non absorbing medium is the following:

$$U_d(r,t) = \frac{v\, exp\left(\frac{-|r-r'|^2}{4Dvt}\right)}{4\pi(4\pi Dvt)^{\frac{3}{2}}} \tag{1.20}$$

that becomes

$$U_d(r,t) = \frac{v\, exp\left(\frac{-|r-r'|^2}{4Dvt} - \mu_a v\right)}{4\pi(4\pi Dvt)^{\frac{3}{2}}} \tag{1.21}$$

to take into account the absorption contribution through the Lambert-Beer law.
Since the equation that has previously been referred to the case of infinite medium, it's important to consider that in the real case the turbid medium under analysis has a finite volume. The most common model for the real geometries of the samples is a slab limited by two parallel surfaces. The slab is surrounded by another medium (e.g. air) that causes a refractive index mismatch. In order to retrieve the solution in the real case, it's necessary to take into account some boundary conditions.
The most simple boundary conditions that can be taken into account are the zero boundary condition (ZBC) and the extrapolated boundary condition (EBC), which are based on the assumption that the fluence is null respectively at the physical boundaries of the slab or at a distance $z_e = 2AD$ from its boundaries. The reconstruction of the fluence inside the slab is possible through the method of the positive and negative image sources, placed at different positions along the z axis (perpendicular to the surfaces of the slab). Each of the sources gives a contribution to the average diffused intensity inside the slab, then putting together all the contributions of the positive and negative sources, the reflectance and transmittance curves can be retrieved for a slab of thickness s. Most of the acqui-

sitions of the TD-NIRS are performed in reflectance configuration, since the muscle and head are usually too thick to have enough signal going out of the sample in transmittance configurations, so the equation for the reflectance curve in the case of having an isotropic point source at z_0 is the only one to be shown for sake of semplicity:

$$R(\rho,t) = -\frac{exp\left(-\mu_a vt - \frac{\rho^2}{4Dvt}\right)}{2(4\pi Dv)^{3/2}t^{5/2}} \sum_{m=-\infty}^{+\infty} \left[z_{3,m} exp\left(-\frac{z_{3,m}^2}{4Dvt}\right) - z_{4,m} exp\left(-\frac{z_{4,m}^2}{4Dvt}\right)\right] \tag{1.22}$$

where

$$\begin{cases} z_{3,m} = -2ms - 4mz_e - z_0 \\ z_{4,m} = -2ms - (4m-2)z_e + z_0 \end{cases} \tag{1.23}$$

with m, the order of the image source. In the case of a medium that is thick enough to be considered semi-infinite (i.e. $s \to \infty$), the reflectance curve is retrieved limiting the sum of 1.22 at the order m=0. The complete demonstration of the method is in the diseration performed by Zaccanti et al. [7].

1.1.5. The reflectance curves: simulations

In this section the simulated reflectance curves I retrieved implementing in a MATLAB code the theoretical model of section 1.1.4 will be shown. The aim of the simulations is showing the influence that absorption and scattering coefficients have in the DTOF of the photons along with the influence that the distance of the detector from the source point has.

Absorption effects

In fig. 1.4 the curve obtained fixing the source-detector distance ρ=30 mm and scattering coefficient $\mu_s' = 1\, mm^{-1}$ and changing the value of μ_a in a range from 0.005 to 0.025 mm^{-1} is shown.
The effect of the absorption's variation is the change in the amplitude of the curve: increasing μ_a at a fixed source detector distance, each of the photons has more probability to be absorbed before re-emerging from the slab. Looking at the different curves, it is also possible to notice that they are wider and their slope after the peak decreases for lower values of absorption: if photons have less probability to be absorbed, they have the possibility to travel for a longer path in the tissue and undergo many scattering events

which delay their arrival at the detector.

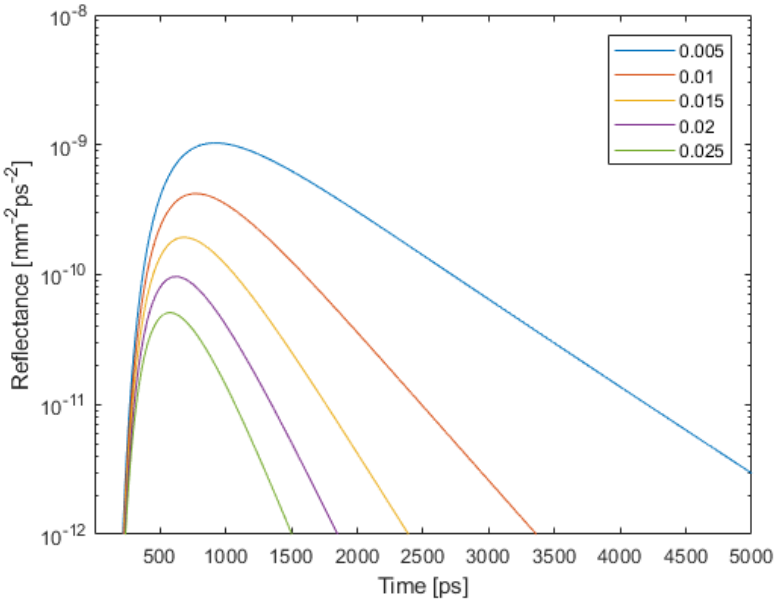

Figure 1.4: Reflectance curves obtained for variable absorption coefficients measured in mm^{-1}, fixed reduced scattering coefficient $\mu'_s = 1\,mm^{-1}$ and fixed interfiber distance $\rho = 30\,mm$.

Scattering effects

The plot in fig. 1.5 has been obtained keeping fixed the value of $\rho = 30\,mm$ and the value of $\mu_a = 0.01\,mm^{-1}$ and changing the value of the reduced scattering coefficient in a range scanning from $\mu'_s = 0.75\,mm^{-1}$ to $\mu'_s = 1.75\,mm^{-1}$. For higher values of the scattering coefficient, the curve results more delayed and this can be understood if one considers that the photons have to undergo more scattering events before arriving at the detectors. Due to the longer path length that is necessary to re-emerge from the sample, photons have also more probability to be absorbed, hence, the peaks of the curves are lower for high scattering coefficients.

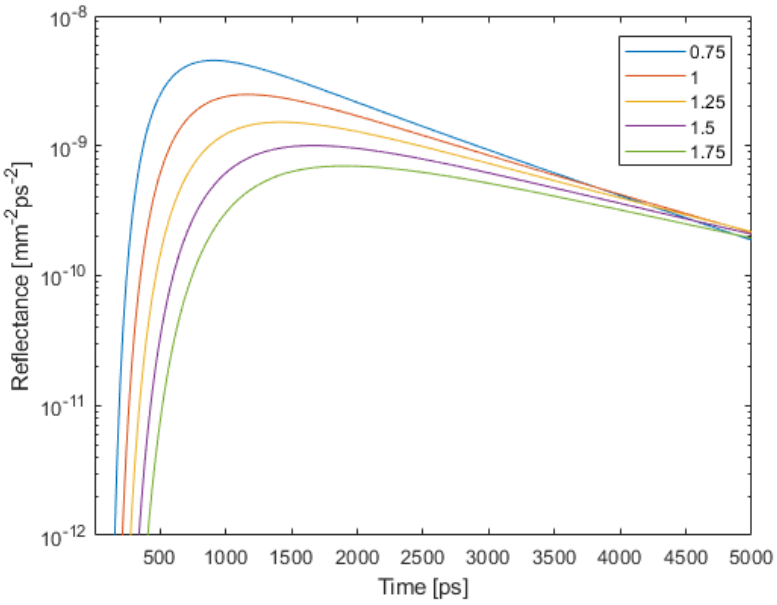

Figure 1.5: Reflectance curve obtained for variable reduced scattering coefficient measured in mm^{-1}, fixed absorption coefficient $\mu_a = 0.01\,mm^{-1}$ and fixed interfiber distance $\rho = 30\,mm$.

Source-Detector distance effects

The configuration of the source and detectors also influences the resulting reflectance curve.
In fig. 1.6, a reflectance curve with a fixed value of $\mu_a = 0.01\,mm^{-1}$ and $\mu_s' = 1\,mm^{-1}$ is shown, for intefiber distances ranging from 10 to 30 mm with steps of 5 mm. Comparing the position of the rising edge of the configuration $\rho = 10\,mm$ and the one $\rho = 30\,mm$, one can notice that the latter is delayed with respect to the former. The reason is the same given for the previous case: longer paths, longer delays to arrive at the detector. Here it's also visible that the curves corresponding to lower interfiber distances are narrower than the ones obtained increasing this distances: the curve tends to be larger in case photons are delayed by the scattering events, that can increase if a longer path is traveled. As in the previous case, the delayed curves result also lower since in longer distances they photons have more probability to be absorbed.

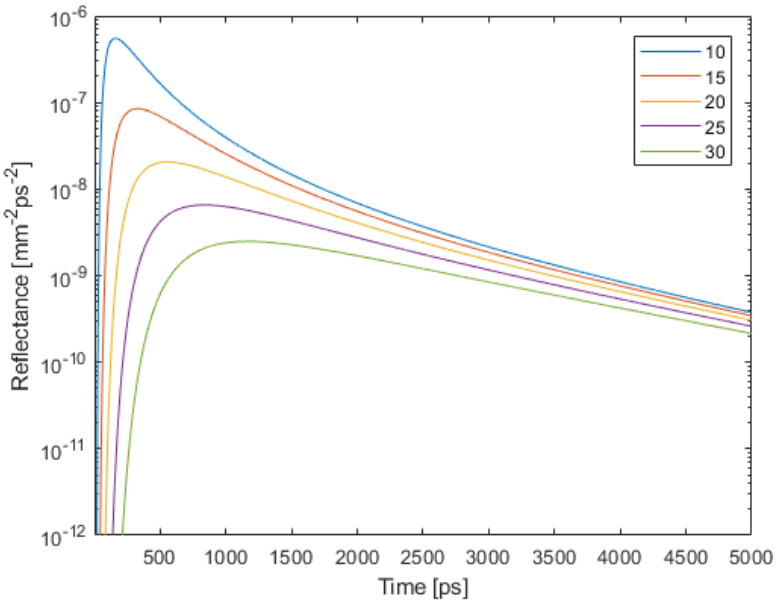

Figure 1.6: Reflectance curve obtained for fixed scattering coefficient (1 mm^{-1}), fixed absorption coefficient (0.001 mm^{-1}) and variable interfiber distance (mm).

1.2. DTOF: recording and analysis

In this section the technique of acquisition of the reflectance curve will be analysed along with the approaches used in order to extract the absolute values of the optical coefficients and their variation.

1.2.1. Time Correlated Single Photon Counting

To retrieve the photons Distribution of the Time of Flight (DTOF) the technique of Time Correlated Single Photons Counting (TCSPC) technique is implemented. The principle on which it relies is the recording of the arrival time of a single photon respect to reference signal [8]. It requires a statistically consistent number of single photons arrival events in order to correctly reconstruct the DTOF (see section 3.4.3). Each of the arrival times is stored in a histogram used to reconstruct the reflectance curve. The general principle of a TCSPC is shown in fig. 1.7. When the pulse is emitted, an electrical START signal arrives at the TCSPC board, while the STOP signal corresponds to the event of arrival of the photon after traveling in the sample. The component of the TCSPC board to which the start and stop signals are fed is the Time Amplitude Converter (TAC). The output of the TAC constitutes the input of an Analog to Digital Converter (ADC) which provides the digital time value to address the histogrammer.

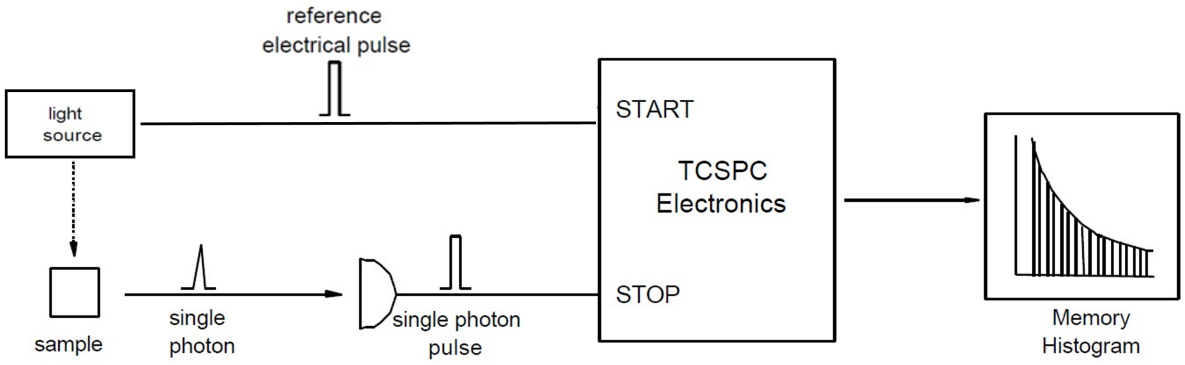

Figure 1.7: Scheme of the time correlated single photons counting working principle [9].

After an excitation cycle, sometimes photons are absorbed in the medium, so they don't arrive at the detector. In this case, at a START signal corresponds no STOP signal, so the TAC has to reset after the overflow, thus limiting the possibility to fully exploit the capabilities of the TCSPC's electronics. For this reason, at high pulses rate, the TCSPCs operates in a reverse mode: in this case, the START signal corresponds to the photon arrival, while the STOP corresponds to the emission of the light pulse: in this way, to all of the started signals will surely correspond a stop. The drawback is that the reference pulses corresponding to the light excitation events must be delayed in order to arrive after the start. The reverse modality is the one employed in the TD-NIRS instrument under analysis.

Another limit to overcome is the following: the detectors and electronics that constitute the TCSPC board have a dead time, during which they can't register a photon while they are processing the previous arrival event.

Thus, TCSPC systems are usually designed to register only one photon per excitation cycle, otherwise the first photon would be detected and the following ones wouldn't, having an effect called "pile-up" leading to a bad reconstruction of the signal because of an excess of early photons. Fig. 1.8 is a schematization of the pile-up effect.

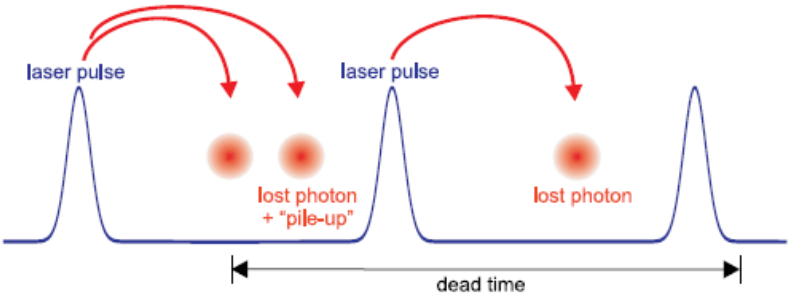

Figure 1.8: Scheme of the pile-up effect as a consequence of the dead time of TCSPC's electronics [8].

To be sure to not lose any photons arrival event, i.e. to be in the single photon statistics domain, the following rule of thumb is used: the detection rate shouldn't exceed the 5% of the emission rate of the laser source. For example, in a a system with a laser source emitting at 80 MHz, the count rate at the detector should be kept at around 4 MHz[8]. In section 3.3.2 an analysis of the maximum count rate allowing the good reconstruction of the reflectance curve for the specific case of the TD-NIRS device under analysis will be performed.

1.2.2. The fitting approach

Several ways are available in order to extract information from the TPSF: the first one ever employed is the fitting procedure.
The aim of this method is the determination of the absolute value of the optical coefficients of a medium through the minimization of the difference between the theoretical reflectance (R_{th}) curve and the experimental one (R_{exp}). The procedure looks for the best possible couple of optical coefficients μ_a and μ_s' in order to minimize the following parameter

$$\chi^2 = \sum_{i=1}^{n} \frac{(R_{th} - R_{exp})^2}{\sigma^2} \tag{1.24}$$

where σ^2 refers to the variance. The term R_{th} that appears in the previous relation is the theoretical curve obtained from the DE model for a given geometry convolved with the Instrument Response Function (IRF) of the instrument. Further explanations about the role of the IRF of the system will be provided in chapter 3.1.1.
The model used to retrieve the theoretical reflectance curves along all the data analysis of the present work is the semi-infinite homogeneous medium.

1.2.3. The gating (or time gated) approach

This approach is based on the separation of the photons DTOF in different time windows and it is aimed at assessing changes in the optical properties happening at different depths in the sample.

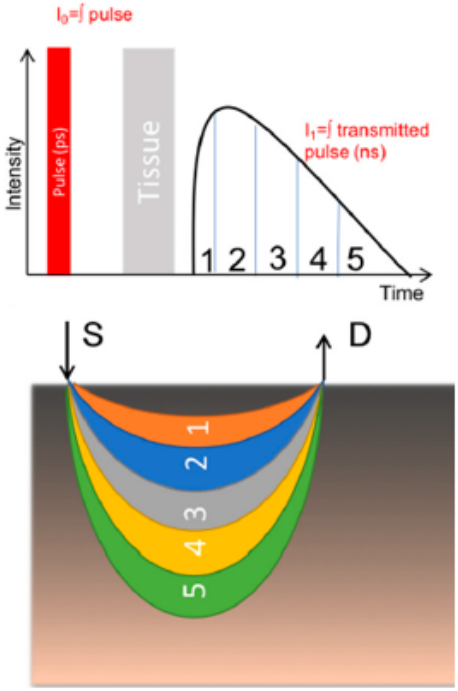

Figure 1.9: Relation between paths traveled by the photons and their arrival time at the detector. Time bins corresponding to the rising edge of the curve are referred to shallow penetration of the photon, while the ones under the falling edge are related to higher depths. The region covered by the photons during their path in the tissue is known as "banana shape" [6].

Figure 1.9 shows the link between the time of flight of the photons, i.e. the delay of their detection, and the distance that they travel inside the tissue: the longer the time of flight, the bigger the penetration depth. Thus, the reflectance curve in different time bins can allow to discriminate between early and late photons, so between shallow and deep optical properties of the sample, as it will be shown in chapter 3.7.2. In this case, the quantity under analysis becomes M:

$$M = \int_0^\infty G(t)N(t)\,dt \tag{1.25}$$

where G(t) represents the weighting function assuming value G=1 for $t_{ak} < t < t_{bk}$ and

G=0 elsewhere. The photons counts revealed at a certain time window k, defined between arrival times t_{ak} and t_{bk} is defined as follows.

$$N_k = \int_{t_{ak}}^{t_{bk}} N(t)\, dt \tag{1.26}$$

Figure 1.10 is a schematization of the data analysis methods: on the left the black dotted

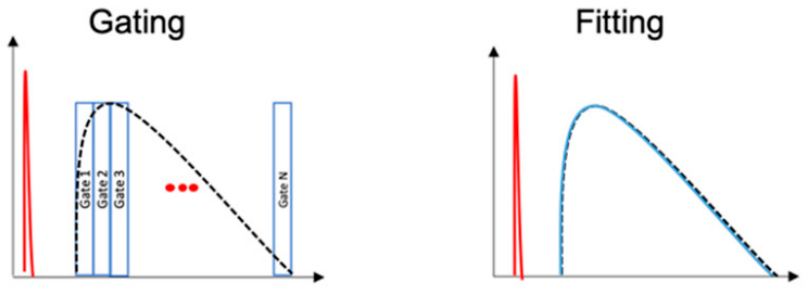

Figure 1.10: Schematizations of the fitting and time-gating approach. The red curve is the impulse response function of the system and the black dotted curve is the experimental DTOF. In the left part of the figure, the blue boxes represent the gating window, while the blue curve in the right part of the figure is the fitted curve [6].

curve is divided in time windows through temporal gates, while on the right the aim is the superposition between a theoretical curve (blue) and the real one (black dotted). The red pulses represent the IRF of the system.

1.2.4. Depth selectivity enhancement

Tasks which involve a physiological response lead to a variation of the absorption coefficient ($\delta\mu_a(\lambda, t)$) in the tissues under analysis with respect to the one related to the baseline reference ($\mu_{a,0}(\lambda, t)$):

$$\mu_a(\lambda, t) = \mu_{a,0}(\lambda, t) + \delta\mu_a(\lambda, t) \tag{1.27}$$

However, the signal coming from the tissue where the changes in the absorption coefficient want to be detected, can be contaminated by systemic phenomena occurring at the superficial layer of the part of the body under analysis. In order to correctly predict the variation of the optical coefficients happening at a specific depth, different methods can be used. In the following paragraphs I will describe the ones usually used for the data analysis of the in-vivo measurements.

Time domain contrast function correction

The first correction that will be described has been proposed in a proceeding by Contini et al. [10] and it exploits the depth information encoded by the photons arriving at different times at the detectors.
The validation of the method has been performed by Monte Carlo simulations. In this frame, the sample under analysis is modeled as a two layers (superficial and deeper) infinite medium and the variation of absorption coefficient in the tissue is modeled by an absorbing inclusion that causes an optical inhomogeneity in the deeper layer. In case the task causes a systemic variation in the absorption coefficient also of the superficial level of the sample under analysis, the time resolved intensity (TRI) can be written as follows:

$$I(t) = I_0(t)exp[-\delta\mu_{a,UP}L_{UP}(t) - \delta\mu_{a,INC}L_{INC}(t)] \tag{1.28}$$

where I_0 is the unperturbed TRI, $\delta\mu_{a,UP}$ and $\delta\mu_{a,INC}$ are the changes of the absorption coefficient both in the upper and inclusion layer and $L_{UP}(t)$ and $L_{INC}(t)$ are the mean time dependent path lengths of the photons in the upper and lower layer.
Thus:

$$I(t) = I_0(t) + \delta I_{UP}(t) + \delta I_{INC}(t) \tag{1.29}$$

The contrast function can be defined as follows:

$$C(t) = \frac{I(t) - I_0(t)}{I_0(t)} \tag{1.30}$$

and putting 1.30 into 1.29,

$$C(t) = \frac{\delta I_{UP}(t)}{I_0(t)} + \frac{\delta I_{INC}(t)}{I_0(t)} = C_{UP}(t) + C_{INC}(t) \tag{1.31}$$

Some simulations based on the diffusion approximation, show that there are suitable times windows τ_E and τ_L such as $C_{UP}(\tau_E)$=$C_{INC}(\tau_L)$ and $C_{INC}(\tau_E) = 0$ leading to:

$$\delta I_{UP}(\tau_E) = \frac{I_{INC}(\tau_L)}{I_0(\tau_L)} I_0(\tau_E) \tag{1.32}$$

$$I_{UP}(\tau_L) = 0 \tag{1.33}$$

Putting together 1.28, 1.29 and 1.32, 1.33, it's possible to discriminate the variation of absorption due to the inclusion, which is the one in which TD-NIRS is interested, from

the one of the upper layer:

$$\delta\mu_{a,INC} = -\frac{1}{L_{INC}(\tau_L)} \ln\left[1 + \frac{I(\tau_L)}{I_0(\tau_L)} - \frac{I(\tau_E)}{I_0(\tau_E)}\right] \tag{1.34}$$

The value of $L_{INC}(t)$ and $L_{UP}(t)$ is roughly estimated, knowing the speed of propagation of the light in the tissue v, as $L_{INC} = v\tau_L$ and $L_{UP} = v\tau_E$.

Mean Partial Pathlength based correction

For the data analysis of the in-vivo measures performed on the brain which will be described in chapter 4, another approach has been used.
The method is the one proposed by Zucchelli et al. [11] and, once again, it has the aim to distinguish between the contribution that each layer gives to the variation of the absorption coefficient. It is based on a more precise estimation of the time dependent mean path-length that the photon travels in each of the layers that composes the sample (e.g. scalp, brain cortex for the head and skin, lipid, surface capillary bed and muscular tissue in case of an arm).
As a consequence of a small variation of the absorption $\delta\mu_a$, the reflectance curve R changes with respect to the unperturbed case R_0 according to equation 1.35, known as modified Lambert-Beer law. Notice that R and R_0 are the time resolved reflectance curves measured by the setup. Considering j layers constituting the sample, each one with known unperturbed optical absorption coefficient and dividing the reflectance curve in k gates, it is possible to obtain, for each of the gates:

$$R_k = R_{0,k} \exp\left(\sum\nolimits_j \Delta\mu_{a,j} L_{j,k}\right) \tag{1.35}$$

where $L_{j,k}$ is the mean partial pathlength (MPP) traveled by photons of the j-th layer in the time window k. The MPP can be computed knowing the time dependent mean partial pathlenght (TMPP) $L_j(t)$ traveled by the photons detected at time t after traveling in the j-th layer. $L_j(t)$ is a parameter which only depends on the unperturbed situation and in [11] it is shown that it can be computed as:

$$L_j(t) = -\frac{1}{R_0(t)} \frac{\delta R_0(t)}{\delta\mu_{a,j}} \tag{1.36}$$

MPP, instead, is defined as:

$$L_{j,k} = \frac{\int_{t_k}^{t_{k+1}} R_0(t) L_j(t)\, dt}{\int_{t_k}^{t_{k+1}} R_0(t)\, dt} \tag{1.37}$$

Once known the MPPs, the absorption variation can be computed through the following relation:

$$ln \frac{R_k(\lambda)}{R_{0,k}(\lambda)} = -\sum_j \Delta\mu_{a,j}(\lambda) L_{k,j}(\lambda) \tag{1.38}$$

This method aimed at improving the depth selectivity of the TD instruments, allowing to reject the effects of the upper layers has been validated through numerical simulations and in-vivo analysis for the case of a two-layers model.

2 | The TD-NIRS device

Before the beginning of the present thesis work, an high power TD-NIRS instrument was already present in the Physics Department of Politecnico di Milano. However, it had some hardware defects which resulted in a bad estimation of the absolute values of the optical coefficients.

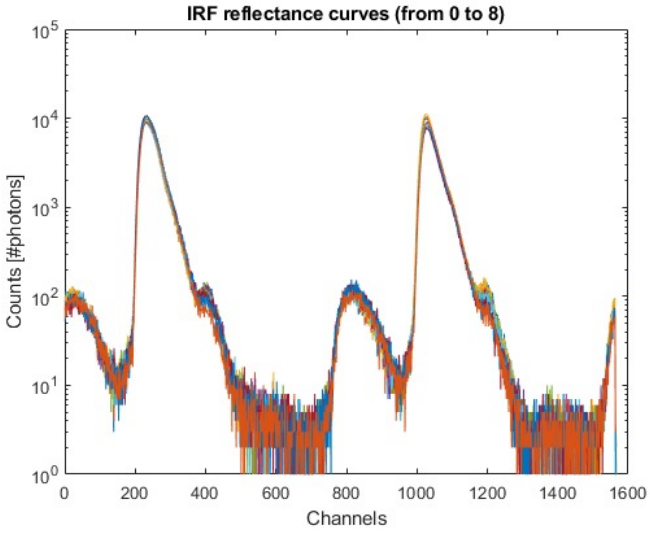

Figure 2.1: IRF curve before the changes made to the instrument [12].

The effects of the defects are visible in fig.2.1, which shows the IRF curve as it appeared before the modifications of the system. Ideally, only the main peaks placed around channels 250 and 1050 and respectively related to the red and IR pulse should be present. Instead, in fig.2.1, some secondary peaks can be seen. Computing the delay of the latter with respect to the main peaks and retrieving the space travelled by the photons in that delay, the causes of these unwanted effects have been deduced. In detail, the secondary peaks around the 400th and 1200th channels have been attributed to the reflections caused by the position of the detectors attenuators in the old setup, while the ones at the channel 0 and 800 are due to the round trip of the photons in the old collection bundles.
As a consequence, the disk attenuators of the detector stages have been tilted of about 20° with respect to the direction perpendicular to the plane of incidence of the light. In this

way, the fraction of reflected photons is deviated from the detection direction. Besides the inclination of the attenuators in the detector stage, another modification has been necessary in the TD-NIRS device: the collection bundles. In order to avoid the reflection problems, the suitable length of the bundle to be used must be an integer multiple of 1.25 m, so the first step that has been done during this thesis work has been the design of a new collection system for the device.

2.1. Collection bundles: simulations and features

The choice of the optical bundles in the detection phase is crucial for the width of the IRF curve, from which the quality of the fitted value of the optical coefficients is highly dependent. The IRF curve must be as narrow as possible in order to be the best approximation of a delta function.
In order to make the best choice in terms of bundles, a parameter that has to be taken into account is the dispersion (fig.2.2): its effect affects the multi-mode fibers, since in that kind of fibers each of the modes of the light propagates along different paths as shown in the figure 2.3. The speed of each of the modes (v) depends on the profile of the refractive index (n) of the core of the fiber:

$$v = \frac{c}{n} \tag{2.1}$$

In the case of step index fibers (2.3 (a)), the n index is the same along all the core, so is the speed, and the higher modes will just propagate for longer time than the lower ones.

Figure 2.2: Effect of dispersion [13].

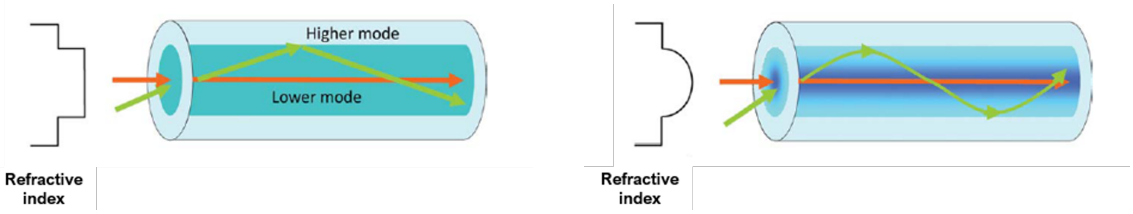

(a) (b)

Figure 2.3: Modes path in multimode fibers (a) Step index fiber, (b) Graded index fiber [14].

In the graded index fibers, instead, the velocity of the modes will depend on the position with respect to the center of the fiber's section (2.3 (b)): the modes will still propagate in different times, but the core can be designed in order to minimize the delay between the highest and lowest ones. This results in a small widening of the pulse, hence a better temporal resolution for the instrument. For this reason, the only fibers that will be taken into account to design the bundles are the graded index ones.
The factors that affect the inter-modal dispersion are the ones that appear in the following relation [13]:

$$\Delta t = \frac{L}{c}\frac{n_1^2}{n_2^2}\Delta \tag{2.2}$$

where n_1 and n_2 are respectively the core and cladding indexes, L is the fiber length and c is the speed of light in vacuum and Δ is defined as follows:

$$\Delta = \frac{n_1 - n_2}{n_1} \tag{2.3}$$

Besides the dispersion, the attenuation is another factor to take into account when choosing a fiber for a certain application. The attenuation factor is defined as follows:

$$\alpha(dB/Km) = -\frac{10}{L} log_{10} \frac{P_{out}}{P_{in}} \tag{2.4}$$

Because of the structure of a bundle, not all its surface is covered by the core of the constituting fibers, hence, not all the optical power being injected at the bundle input will be effectively coupled in its fibers.
The amount of coupled power P_{in} is dependent on the bundle structure and internal arrangement of the fibers.

The efficiency η of a bundle is the ratio between P_{out}/P'_{in}, where P'_{in} represents the input power injected at the optical fiber. An useful parameter that quantifies the packing arrangement is the bundle packing fraction (BPF) [15]. Considering A as the total bundle cross sectional area and fibers with core diameter d, the BPF can be computed as follows:

$$BPF = \frac{N\pi d^2}{4A} \tag{2.5}$$

and the efficiency can be thus expressed as

$$\eta = 10^{-\frac{\alpha L}{10}} \pi N A^2 A_{bundle} BPF \tag{2.6}$$

where NA is the numerical aperture of the optical fiber. Generally, a good way to pack fibers in a bundle, is placing rings around a central fiber, until filling the whole desired area, as shown in the figure 2.4. This results in an hexagonal structure.

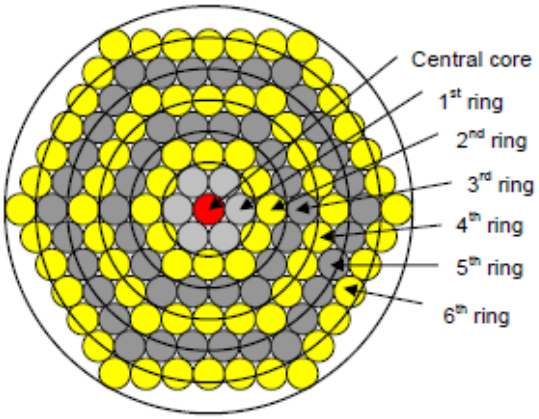

Figure 2.4: Scheme of the arrangement of the fibers in a bundle: hexagonal structure[15].

Given a total diameter D of the bundle, d' the total diameter of the fiber and being m the order of the ring around the central fiber, the total number N of fibers that can be arranged is given by:

$$N = 1 + \sum_{n=0}^{m} 6n \tag{2.7}$$

where the number of rings fitting in the section has to respect the following condition

$$D = (2m + 1)d' \tag{2.8}$$

In the case of high number of fibers packed in hexagonal configuration, N can be approximated by:

$$N = 0.7\left(\frac{D^2}{d'^2}\right) \tag{2.9}$$

In the special case of the TD-NIRS device, in order to make possible to connect them to the detector module, the bundles must have a maximum diameter of 3 mm.

In the frame of graded index fibers, different proposals by various companies have been analyzed, to choose the best option for the sample to detectors collection system.
Glass and plastic graded index fibers are the ones that have been taken in consideration to constitute our bundle. Glass fibers are suitable for long distances, presenting low attenuation for the visible and infrared light. However, they are expensive. Plastic fibers, instead, are cheaper and more flexible with respect to the glass ones. However, on long distances, they cause a high attenuation of the infrared signal. In terms of geometry, glass fibers allow a finest control on the overall section of the bundles, having smaller diameters with respect to the plastic fibers.
First, a comparison between the efficiency of the glass fibers has been performed and then the same thing has been performed for the various options of plastic fibers. Consequently, a comparison between the best options of the two groups has determined the best component to create the bundle.

Glass fibers

Table 2.1 lists all the optical parameters of the glass graded index fibers useful to compute their dispersion and efficiency.

Glass fibers			
	THORLABS 1	THORLABS 2	FiberOpticSystem
NA	0.275	0.2	0.29
Core diameter (μm)	50	62.5	100
Cladding diameter (μm)	125	125	140
Attenuation @800 nm (dB/m)	< 0.0023	< 0.0029	< 0.005
n core	1.48	1.496	1.496*

Table 2.1: Properties of the glass fibers taken into account to constitute the bundle. Please notice that the values with * have not been provided from the website [16, 17] and they constitute an assumption based on a parallelism between fibers of the same materials and providers.

Fig.2.5 shows the efficiency curve related to bundles of different diameters and made of each type of glass GI. The curves have been retrieved implementing in a MATLAB code the equations of section 2.1. As can be observed, for each considered bundle diameter, the THORLABS 1 option has a lower efficiency than the THORLABS 2 one. This is due to the fact that, in a given bundle diameter, one can find the same amount of fibers in both the cases (table 2.2), being the cladding size the same, but the light is guided inside the core, which is bigger for the THORLABS 2 fibers. Moreover, since bigger cross sections of the bundles admit an higher number of constituent fibers, it can be noticed that for each glass fiber model, an increase of the diameter size of the bundle leads to the increase of η. Looking at fig.2.5, it can be noticed that the optical properties of the FiberOptics glass fibers, allow the highest performances of the bundle.

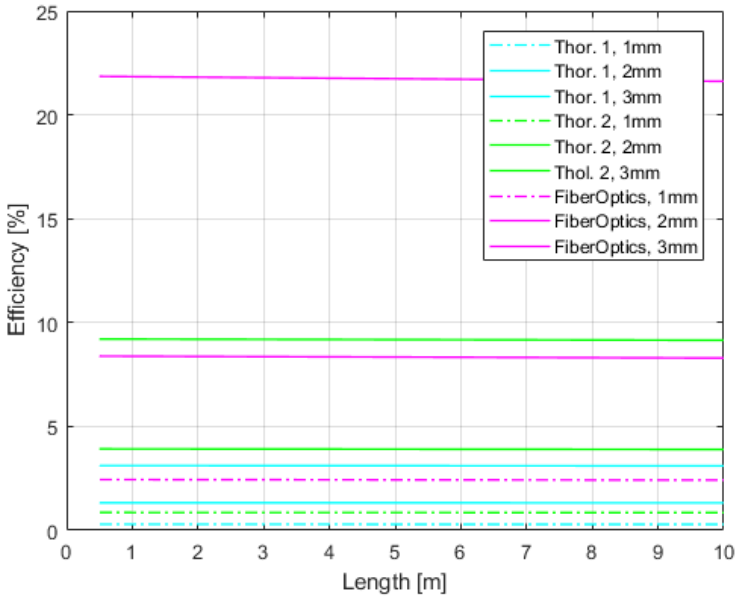

Figure 2.5: Efficiency of the considered glass bundles for different diameters of the bundle itself.

Number of fibers in the bundle			
Bundle diameter	Thor. 1	Thor. 2	FiberOptics
1 mm	37	37	37
2 mm	169	169	127
3 mm	397	397	331

Table 2.2: Number of glass fibers fitting into different bundles diameters.

The simulation of the dispersion curve related to the best glass bundle is shown against the length of the bundle in fig.2.6.

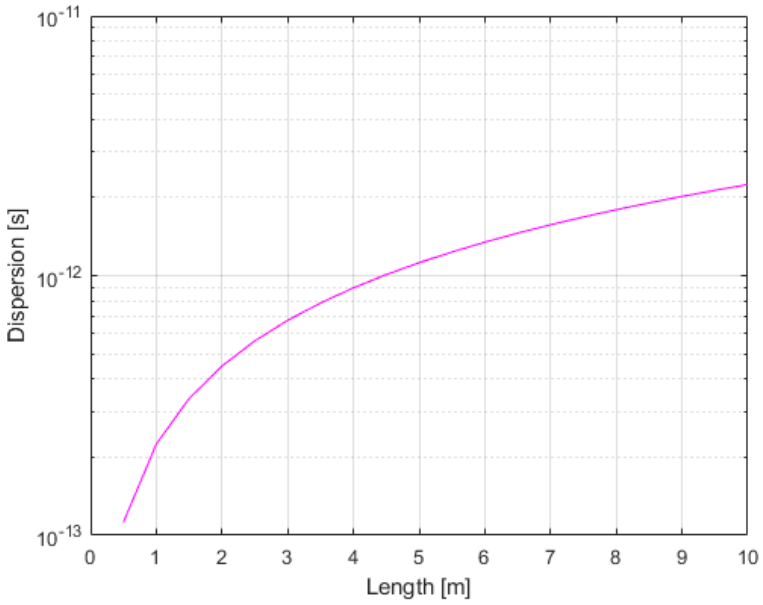

Figure 2.6: Dispersion curve of FiberOptics glass fibers.

Plastic fibers

As for the glass fibers, the optical properties that have been taken into account to evaluate the performances of the bundles are shown for the plastic optical fibers (POF) case in table 2.3.

Plastic fibers			
	Optimedia 1	Optimedia 2	Optimedia 3
NA	0.3	0.23	0.23
Core diameter (mm)	0.9	0.4	0.75
Cladding diameter (mm)	1	-	-
Attenuation @600 nm (dB/m)	< 0.2	< 0.24	< 0.2
Attenuation @800 nm (dB/m)	< 2	< 2*	< 2*
n core	1.52	1.52*	1.52*

Table 2.3: Properties of the plastic fibers taken into account to create the bundle. Please notice that the values with * have not been provided from the website [18] and they constitute an assumption based on a parallelism between fibers of the same materials and providers.

In fig.2.7 the efficiency simulated for POF bundles composed by a different number of fibers is shown. The table showing the relation of the overall bundle diameter and the number of fibers fitting in it can't be provided for the case of plastic GI bundles since, as shown in table 2.3, the total diameter of the bare fiber is provided only for OM 1. For the latter, a bundle constituted by 1, 3 and 7 fibers would result in an overall diameter of 1 mm, 2.15 mm and 3 mm respectively.

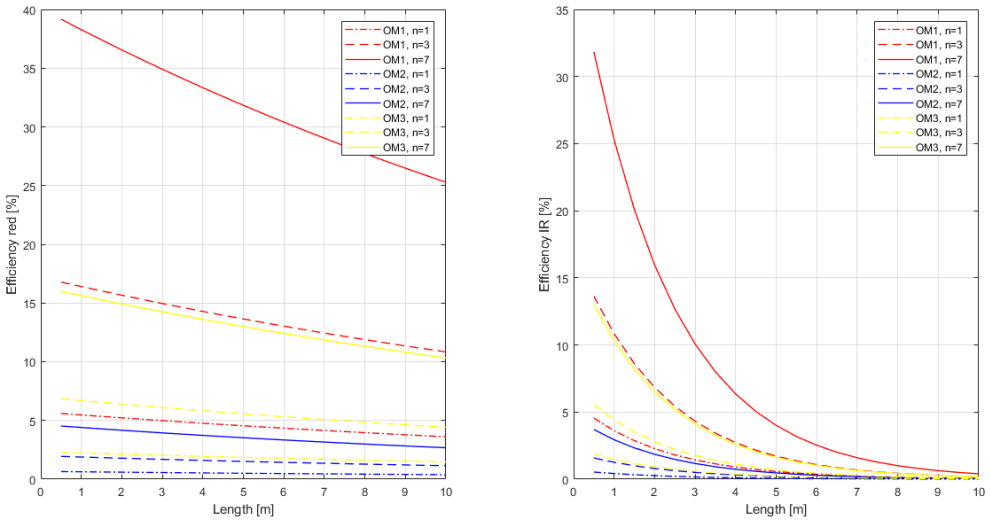

Figure 2.7: Efficiency of the considered plastic bundles for different geometries and different wavelengths.

Eq. 2.6 shows the dependence of the efficiency on the amount of cross sectional area which is useful to couple the light into the fiber, which is in turn dependent on the number of fibers that constitute the bundle (eq. 2.5). One can observe in fig. 2.7 that, as expected, increasing the number of fibers, the efficiency increases as well for all the considered bundles. However, since the BPF is also proportional to the core diameter of the constituent fibers, for a given n, the most efficient bundle is the one that has the biggest value of d, hence, OPTIMEDIA 1 is the best option among the considered ones. Then, this is the one to be compared with the FiberOptics bundle. In fig.2.8, the simulated dispersion curve is shown for the OPTIMEDIA 1 bundle of different lengths.

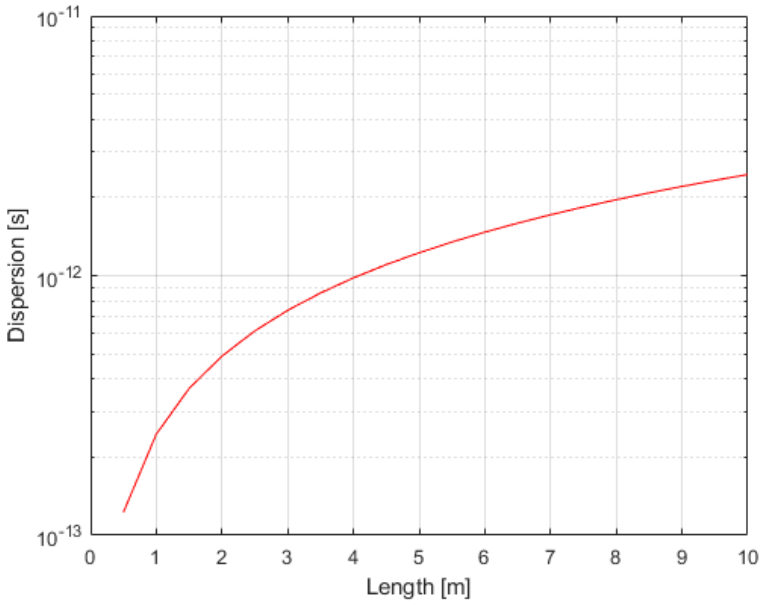

Figure 2.8: Dispersion curve for OPTIMEDIA 1 fibers.

FiberOptics and Optimedia 1: final comparison

From the previous plots, one can see that, in order to get an high power transmission, it worth keeping the diameter of the glass bundle around 3mm, which is the maximum allowed for compatibility with the detector's module. In the case of OPTIMEDIA 1, the geometries shown in fig. 2.9 allow keeping the diameter of the bundle around 3mm, then I will compare the performances of the POF bundles with this geometry with the ones of the corresponding glass FiberOptics bundles with the same diameters.

Figure 2.9: Scheme of the arrangements and respective total diameters of a OPTIMEDIA 1 bundle.

From the figure 2.10 it can be seen that the limiting feature for the POF bundle construction is the attenuation in the IR region, since it causes the rapid decay of the plastic fibers efficiency for lengths $>= 1.5m$. Below this measure, instead, the POF fibers are convenient for both the visible and IR light attenuation.

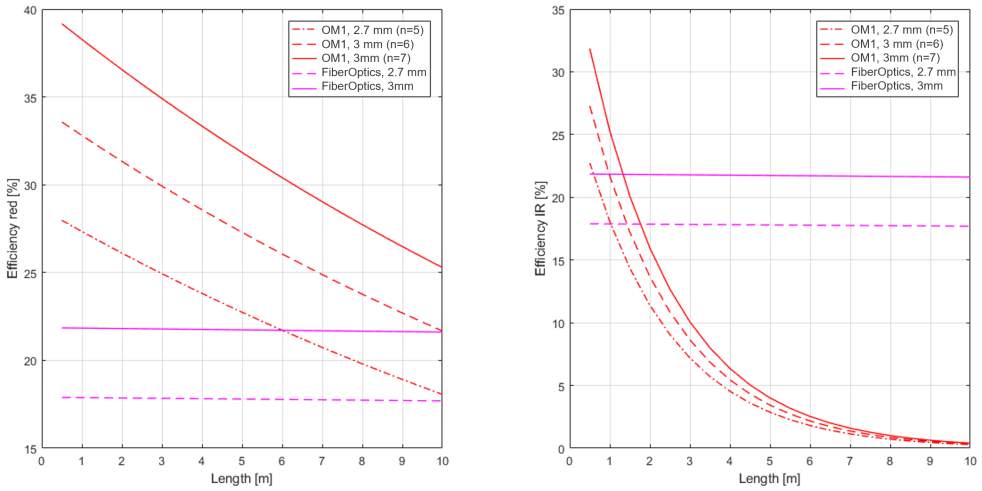

Figure 2.10: Efficiency comparison.

In terms of dispersion, fig. 2.6 and 2.8 show that, even if the dispersion is lightly shifted downwards for the FiberOptics case in comparison with OPTIMEDIA 1, the order of magnitude doesn't exceed the pico-second for both of the options, so, since 1.25 m is the minimum length that avoids the presence of undesired peaks and it is a length that keeps the efficiency in the high performances region for the POF, the choice of the fibers for the construction of the bundle has fallen on the OPTIMEDIA 1 option.

Bundle construction

The 4 bundles for our TD-NIRS system have been made arranging 7 graded index POF (Optimedia 1) in an hexagonal configuration, resulting in an overall 3 mm internal diameter and 1.25 m lenght bundles. The fibers have been glued with a bi-component glue and covered with metallic cylinders (4 mm diameter and 4 cm and 8 cm length respectively for the sample and PMT side) at both ends (fig. 2.11) and then covered in the rest of their length with a black thermo-restringent guaine (fig. 2.12).
The tips of the bundles have been lapped and polished in order to have a flat surface.

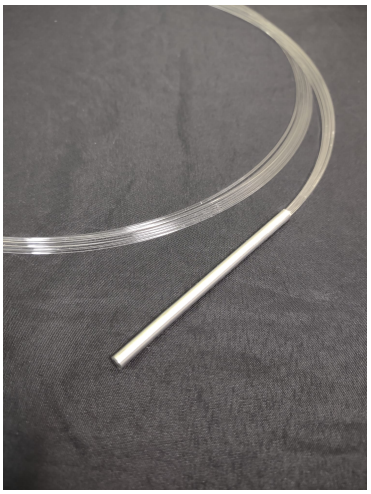

Figure 2.11: Detail of the bundle metallic end before covering it in the black thermo-restringent material.

Figure 2.12: Bundle: final result.

2.2. The probes set

Since the collection bundles have been customized, it has been necessary to design a set of suitable probes to inject and collect the light in the measurements. The probes have been designed in Autodesk Inventor and 3D-printed with a Poly lactic Acid (PLA) black filament.

Regarding the on-phantom measurements, a set of probes with source-detector inter-fiber distance from 1 to 5 cm has been realized. The structure is the same for all of them (7.6 cm x 2 cm x 1.2 cm), the only changing feature is the respective position of the fibers holders. The latter probes have been designed in order to fit in a phantom container cap that had been designed in the past and exploited as support for the probes that I've

create.
In order to avoid photons to go directly from the injection fiber to the collection bundle without entering in the phantom or sample, each of the reflectance mode probes, has been covered with a layer of black neoprene, a material that allows the absorption of the direct light.
Regarding the IRF setup, instead, I've designed a "sandwich" structure with two parallelepipeds, one for the injection fiber (7 cm x 7 cm x 0.9 cm), one for the detection bundle (7 cm x 7cm x 2 cm). Each of the parallelepipeds has a cylindrical removable fiber holder in the middle, where the fibers can be fasten through a screw. Due to the presence of the hole in which the cylindrical fiber holders can be inserted, this structure can be used for many kinds of bundles and fibers just adapting the holder to the required dimensions.
Similarly, the cylindrical adapters can be removed and integrated to already existing structures, such as the typical fNIRS caps used for the brain related adquisitions. In figure 2.13 one example of the phantom probe (a) and IRF structure are shown (b).

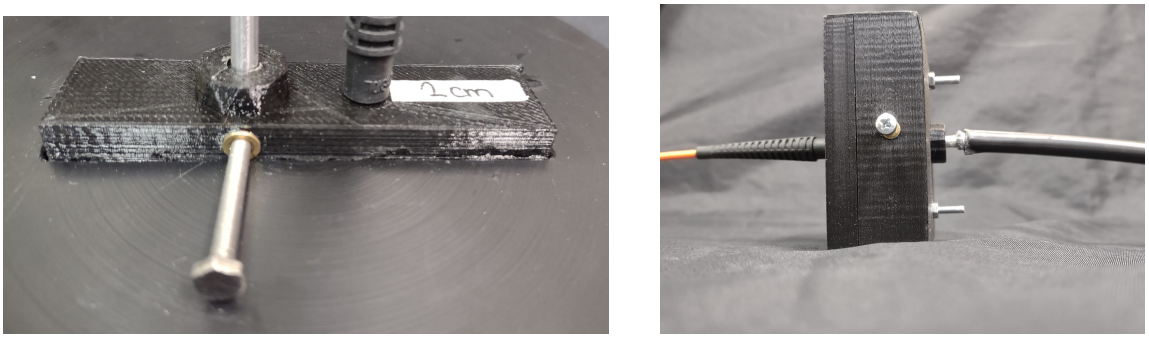

(a) (b)

Figure 2.13: (a) One of the probes used for the on-phantom acquisitions already inserted in the phantom container cap. (b) "Sandwich" setup for the IRF calculation.

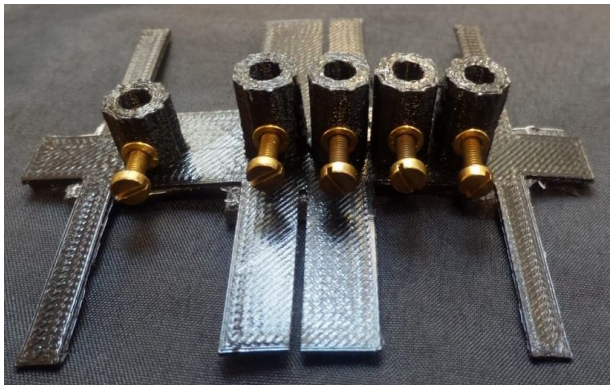

Figure 2.14: Probe used for an in-vivo measurement.

The in-vivo measurements have been realized with probes made by one holder for the source and a series of four holders for the collection bundles placed next to each other at 1 cm distance (fig. 2.14). The nearest collection point is placed at 2 cm from the source, while the farthest at 5 cm. As the on-phantom measurements probes, the ones for the in-vivo measurements have been covered with a layer of neoprene and equipped with screws to lock the fiber and the bundles during the acquisitions.

2.3. Modules

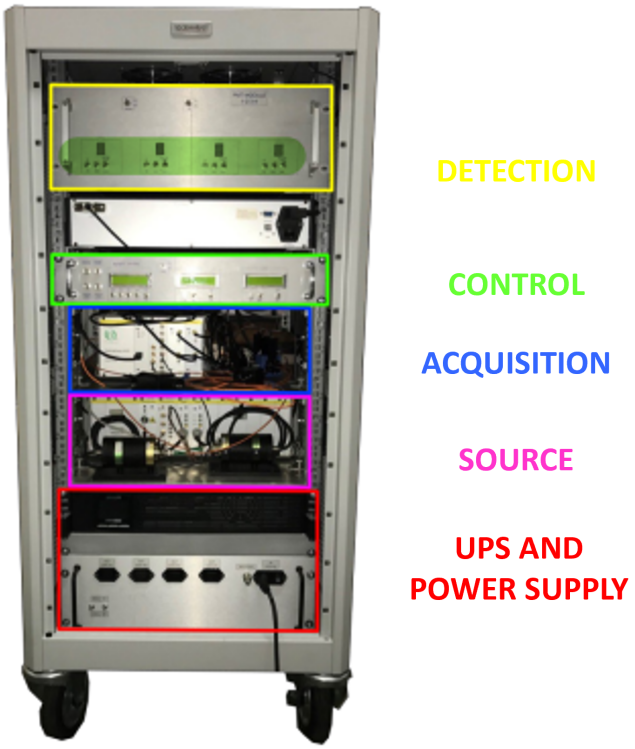

Figure 2.15: Modules of the device [12].

The instrument has a modular structure (fig. 2.15), assembled in a 19" rack equipped with wheels, useful to allow its transportation for clinical measurements.

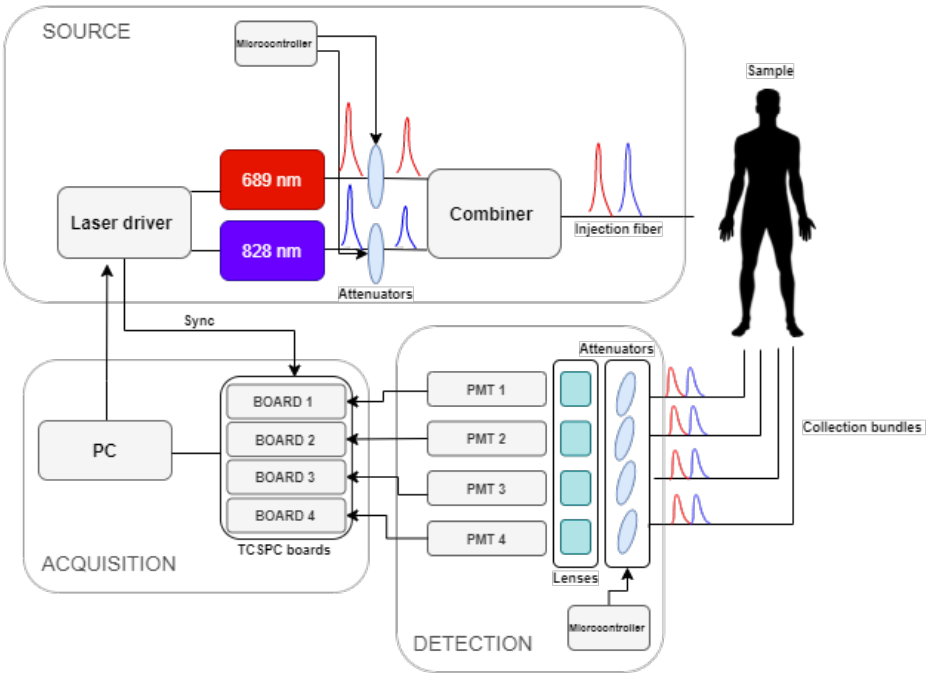

Figure 2.16: Scheme of the interaction between source, detection and acquisition modules.

Details about each of the components of the device and their interaction (fig. 2.16) will be provided below.

Power supply

The electricity network of the building in which the instrument is operating provides the power supply to the TD-NIRS device. An Interruptible Power Supply (UPS) and a de-coupler embedded in the device for safety regulations allow the system to keep on working, even in case of blackout or problems with the external electricity network. The instrument can be turned on both via remote and local control, respectively through a GSM system and a manual switch. This feature is useful in case of necessity to warm the instrument up before the arrival at the place where it is located.

Laser sources

In the sources module, two high power pulsed diode lasers (LDH-P-C PicoQuant GmbH, Berlin, Germany) working at 689±1 nm (red) and 828±1 nm (IR) are electronically driven at 80 MHz (PDL-828-L Sepia II, PicoQuant GmbH). They emit an average maximum power of 63 mW and 33 mW. The minimum width of the pulses is 72 ps for the red laser and 96 ps for the IR one, but it will temporally spread after the light travel along

the optical path leading to the sample.
The collimated beam is coupled into step index glass fibers, with a core/cladding ratio of 600/660 μm and a NA=0.22 (OZ Optics, LTD). Two electronically controlled glass variable attenuators (DDR-100, OZ Optics LTD., Ontario, Canada), one for each wavelength, are placed between the laser heads and a combiner, which is useful to perform the time multiplexing: the IR pulse is delayed with respect to the red one, so both of them can impinge on the sample in a single acquisition window and each of the pulses can be provided with independent power values because of the independent attenuation stages.

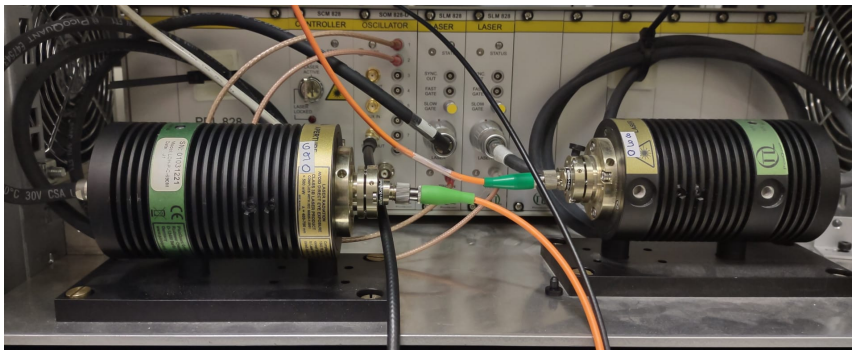

Figure 2.17: Laser sources.

Detection system

Once arrived from the sample at the detectors module via graded index plastic fiber bundles with 3 mm diameter and 1.25 m length, the beams can be attenuated by electronically controlled continuous variable attenuators (NDC-50C-4-B, Thorlabs Inc., Newton, New Jersey, United States) placed in each of the detection channels. After the attenuation stage, the beams are focused through a system of achromatic doublet lenses (AC254030B, Thorlabs Inc., Newton, New Jersey, United States) to the active area of cooled hybrid photomultipliers (PMT). Thanks to their cooling system, the detectors have a low dark count rate and a low transit time, which allows to operate in a single photon detection up to a rate of 10MHz. The PMTs transform the optical signal in input in an output electrical signal, which constitutes the input of the HydraHarp 400 system (PicoQuant GmbH), the boards that performs the TCSPC process. This component also receives a sync signal from the laser driver and computes the difference between the two, in order to create the time histogram for the DTOF. The communication with the PC is performed through an USB connection. Data is stored through a software that can control and automate the measurement process through a user friendly interface.

3 | Instrument characterization

International standard protocols are necessary in order to assess and compare the performances of different instruments or to evaluate the upgrades of the same device [19]. In this chapter, the instrument will be characterized according to three standard protocols aimed at investigating the key features of diffuse optics instruments: BIP, MEDPHOT and nEUROPt. Some custom made protocols will be presented as well to assess the limits of the device and its operating conditions.

3.1. BIP PROTOCOL

The first standard protocol exploited in order to validate the optical system is the Basic Instrument Performace (BIP) protocol, which evaluates the basic characteristic of the device, without focusing on the sample with whom it is interacting. In the following sections, the specific parameters that were measured will be illustrated with the respective results. The aim of this work was the characterization of the four detectors and the choice of the best one in order to perform the further characterizations. For sake of completeness it is important to notice that, in this phase of the work, the same bundle of fibers was used for all the detection lines in order to focus the attention on the detector itself.

3.1.1. Instrument Response Function

The IRF (Instrument Response Function) measures the DTOF of the photons when the pulse exiting from the injection fiber is directly collected by the detection bundles. It is an useful parameter to evaluate how the pulses exiting from the laser sources, which already have a non-null width, are broaened because of the path that they travel in the optical and electronics components. The IRF curve, then, is the result of the contribution of the width and shape of the laser pulses, of the dispersion caused by the optical fibers and the broadening of the pulse given by the electronics and the detectors. The crucial characteristic of the IRF is its full width at half maximum (FWHM) and the goodness of the fitting procedure highly depends on this parameter, since the result of the convolution of the IRF with the theoretical reflectance curve is the one that is fitted with

the measured curve. In order to measure the IRF of the instrument, the IRF cube that was described in the chapter 2.2, which allows to position the injection fiber in front of the detection bundle, is used. A 100 μm of TEFLON is placed between the fiber and the bundle. TEFLON is an highly scattering material useful to mimic the diffusion regime. In this way, the DTOF which is retrieved only depends on the influence of the instrument on the path of the photons.
As previously mentioned, the device has partially been modified in order to solve some of the problems that caused the presence of unwanted secondary peaks in the IRF (see fig. 2.1). For sake of completeness, the FWHM of the IRF before the modifications is shown in table 3.1.

FWHM (ps)		
Channel	Red	IR
1	375	330
2	379	330
3	433	396
4	417	390

Table 3.1: FWHM of the IRF referred to the old setup.

The new set of collection bundles, due to its suitable length of 1.25 m and dispersion characteristics, along with the new inclination of the detectors attenuators, have improved the quality of the IRF curve, removing the unwanted peaks and narrowing its width.
In fig.3.1 an example of IRF curve is shown. Two peaks are observable. The first one, around channel 150 is related to the red pulse, while the one around channel 950, corresponds to the IR pulse.

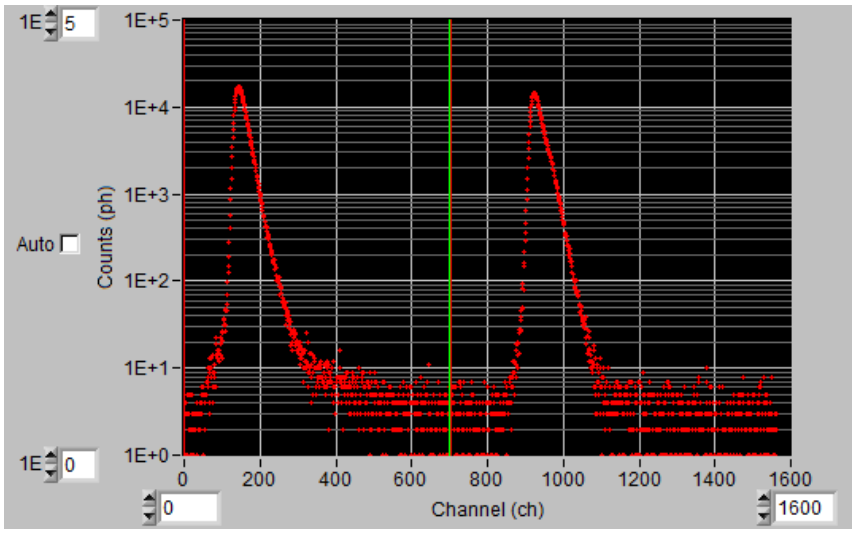

Figure 3.1: Example of the IRF curve. The first peak refers to the red pulse, the second one refers to the IR pulse, which is delayed through the action of the combiner.

The FWHM of the IRF is smaller with respect to the one related to the previous setup. Table 3.2 shows this parameter for each of the detection channels and for each of the two wavelengths.

FWHM (ps)		
Channel	Red	IR
1	225	218
2	242	240
3	252	246
4	243	239

Table 3.2: FWHM of the IRF after the hardware improvements.

This is the evidence of the resolution of all the problems related to the old setting of the TD-NIRS instrument, so, to avoid redundance, in the next sections all the characterizations of the modified device will be shown without the comparison with the previous situation.

3.1.2. Responsivity

The responsivity parameter gives information about the magnitude of the measured signal when impinging on a target with a certain number of photons. In order to do so, the standard target used for the characterization is a phantom with known optical properties ($\mu_a = 0.01\,mm^{-1}, \mu_s' = 1\,mm^{-1}$), capable of transforming a collimated beam of light impinging on one of its surfaces in a known radiance profile emerging from the opposite one: the transmittance modality was used for this measurements.
The relation between input power and responsivity is the following one:

$$s_{det}^{L}(\lambda) = \frac{N_{tot}}{t_{meas}\kappa_p(\lambda)P_{in}(\lambda)} \tag{3.1}$$

where κ_p is a phantom-specific transmittance factor [19], N_{tot} is the number of collected photons at the detector module, P_{in} is the power impinging on the phantom and t_{meas} represents how long the measurement lasts.
30 repetitions of 1 s were carried out with 10^6 photon/s for the responsivity measurements. The regulation of the count rate was performed through the source attenuators and then the power impinging on the sample was measured. No attenuation was set at the detectors stage.

Responsivity ($10^{-8}m^2sr$)		
Channel	690 nm	830 nm
1	2.28	1.27
2	4.41	2.20
3	1.24	0.655
4	3.32	1.96

Table 3.3: Responsivity of the four channels.

The results that have been found are comparable, in order of magnitude, with the channel responsivity of other time domain systems based on hybrid PMT [20]. The previous table shows that, among the four channels, the 2nd and 4th are the best ones in terms of responsivity.

3.1.3. Afterpulsing ratio

The IRF can be affected by PMT signal dependent afterpulses, given by the emission of positive ions tens of microseconds after the single-photon pulse. The accumulation of afterpulses can cause a background signal that can be quantified through the following relation:

$$R_{ap} = \frac{N_{mean,bkg} - N_{mean,dark}}{N_{tot,IRF}} \frac{T_{laser}}{\Delta t} \tag{3.2}$$

where $N_{mean,bkg}$, $N_{mean,dark}$ and $N_{tot,IRF}$ are the mean value of the backgrounds counts of the IRF, the one of the dark adquisition and the total counts of the IRF curve respectively, T_{laser} is the inverse of the repetition rate of the laser (80 MHz) and Δt is the width of each detection channel (8 ps).

In the following table, the results obtained by 10 acquisitions (1s each) with a goal of 10^6 counts per board in the IRF curve are shown.

$R_{ap}(\%)$		
Channel	690 nm	830 nm
1	2.29	2.08
2	1.06	0.69
3	0.47	0.38
4	0.93	0.77

Table 3.4: Afterpulsing ratio of the channels.

The last three channels are pretty homogeneous in terms of afterpulsing ratio, while the first line results the worst under this point of view. However, considering its absolute value, this represents a low percentage and doesn't affects the performances of the system.

3.1.4. DNL

The non-uniformity between all the time channels of a TCSPC has to be assessed. Ideally, each of the channel width should be the same: otherwise, this would lead to a variability

in the number of collected photons and their erroneous recorded distribution.
The Differential Non Linearity is the parameter that must be analysed to guarantee the correct performance of the system, sometimes affected by the cross-talk or mistaken pick-up of start and stop signal.
In order to do so, it's necessary illuminate the detector with a non coherent light illumination and a number of counts $>= 10^5$.
In this way the DNL can be calculated as:

$$\epsilon_{DNL} = \frac{N_{DNL,max} - N_{DNL,min}}{\overline{N_{tot,DNL}}} \cdot 100 \tag{3.3}$$

where $N_{DNL,max}$ and $N_{DNL,min}$ are the highest and lowest number of photons collected in a channel and $\overline{N_{tot,DNL}}$ is the average number of photons collected in the total number of acquisitions.

ϵ_{DNL} (%)			
Channel 1	Channel 2	Channel 3	Channel 4
6.14	5.72	6.36	5.40

Table 3.5: DNL of the four channels.

The retrieved values for the DNL are the result of 20 acquisitions of 1 s, each one with a goal of one million counts on the board. The attenuators of the detection stage were set to the zero attenuation level. The results don't exceed a value of 7% and these values are acceptable to our purposes.
The channel 4 is the one that shows the best DNL, besides the good responsivity and afterpulsing assessment, so it is the one to be chosen for the further characterizations of the system, which, as said, was performed on a single line.

3.2. Power assessment

The FWHM of the IRF depends on some freely settable parameters. It cannot be narrower than the pulse emitted at the laser heads, but the width of the latter depends in turn on the amount of emitted power.
In section 2.3, the maximum nominal values of power emitted at the laser head are defined. Practically, the power has been changed in order to find a trade-off between the temporal resolution of the system and the power arriving at the sample: the higher is the power, the wider is the pulse at the laser heads. In our case, the emitted has been set to

39% of the maximum available for the red laser and 71% for the IR one.
In table 3.6, the values of the power measured at the input of the combiner and of the sample, with a fiber of two different lengths connecting the latter, are shown.

P_{in}	690 nm	830 nm
Combiner input	3.36 mW	9.50 mW
Sample input (1.25 m)	1.91 mW	7.94 mW
Sample input (2.50 m)	1.83 mW	7.86 mW

Table 3.6: Power measurements at the output of the combiner and at the input of the sample with injection fibers of different lengths.

It can be noticed that, an higher length of the injection fiber, determines a larger attenuation of the beam, as stated by the Lambert Beer's equation (see chapter 1), but, in this case, due to the attenuation properties of the glass fiber, the loss of power switching from a 1.25 m length fiber to a 2.50 m one is negligible, hence, when necessary it is possible to use a larger injection fiber to make the measurements easier.

3.3. Further characterizations

Before proceeding with the standardized protocol's characterization measurements, it's been necessary to perform some preliminary analysis, in order to understand:

- the influence of the attenuation stage of the detectors in the fitting procedure (section 3.3.1);
- the maximum reachable count rate that is possible to establish in order to have a good fit of the data (section 3.3.2);
- the minimum acquisition time to collect enough photons to correctly retrieve μ_a and μ_s' (section 3.3.3).

3.3.1. Detection attenuators characterization

As mentioned in section 2.3, the detection module have one circular glass attenuator per channel. Each of them can be controlled by a micro controller which allows to set the attenuators in 10 different positions going from 0 (maximum attenuation level) to 9 (zero attenuation). Hence, the light coming from the collection bundles comes at the detectors

with the possibility to be more or less attenuated, giving the chance to optimize and equalize the signal arriving at the different detectors in case of simultaneous multiple ρ acquisitions.

Previous characterizations of the instrument [12] have shown that the error predicting μ_a and μ'_s increased when the detection attenuation for the IRF and sample measurements was different, thus leading to a necessity of setting, for both the acquisitions, the same value of attenuation in the detectors.
Actually, to acquire an IRF curve each time that the situation requires a change in the level of the detection attenuation has the disadvantage of slowing down the measurement procedure. In fact, in this case, the setup must be changed twice, to switch from the sample measurement configuration to the IRF one and viceversa.
Moreover, the possibility of freely changing the level of attenuation at the detection stage, gives one more degree of freedom in the regulation of the number of photons arriving at the detector in a measurement. Probably, the problem was due to undesired effects of reflection given by the deposited layer of the attenuators and , in order to verify whether tilting the position of the disks fixed the problem, the following characterization has been performed.
10 acquisition of 1 s each made on the T_a phantom ($\mu_a = 0.1\,cm^{-1}$, $\mu'_s = 10\,cm^{-1}$), at 3 cm interfiber distance, counts goal of $10^6\,cps$ and attenuation level 9, have been fitted with 10 IRF curves taken with attenuations varying from 9 to 0 level.
The results in fig. 3.2 show that the error on the fitted optical parameters doesn't exceed the 3% for any of the attenuation levels with respect to the zero attenuation case, taken as ideal one. This result suggests that, no matter what is the value of the attenuation of the IRF with respect to the sample's one we have, the fit can lead to a good result and the measurement process can be speeded up.

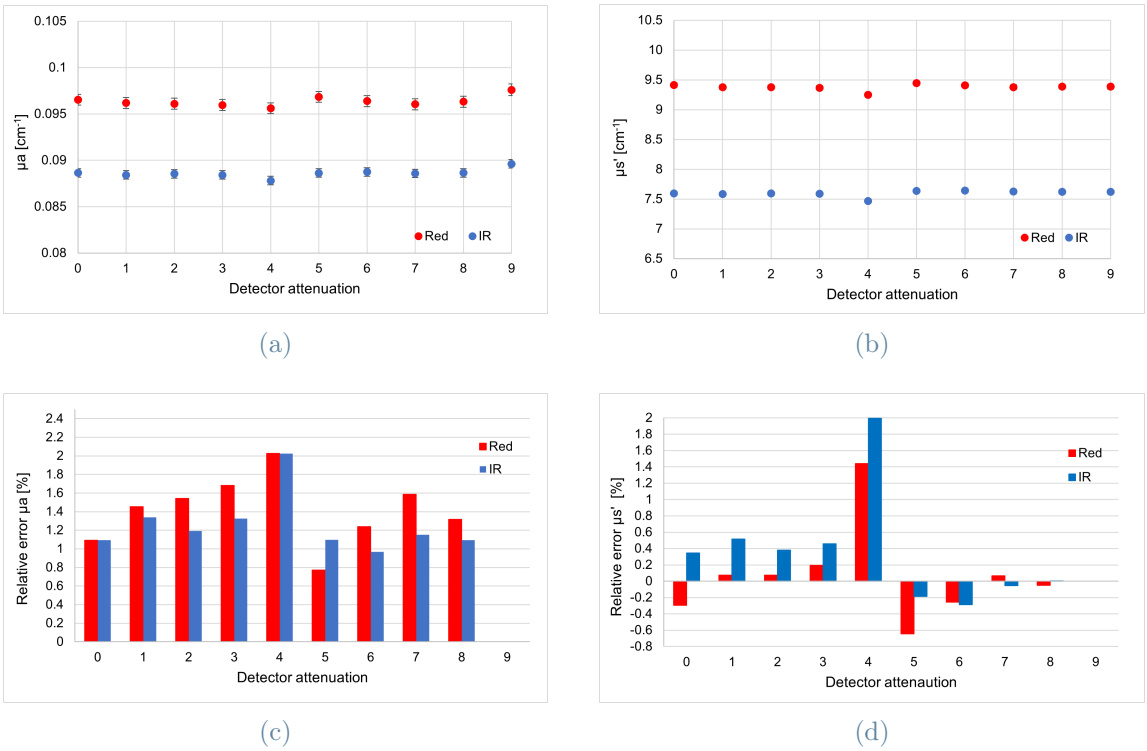

Figure 3.2: Figures (a) and (b) show the average values over the 10 repetitions of μ_a and μ_s' obtained varying the IRF attenuation in the fitting stage. (c) and (d) show the error with respect to the zero attenuation (level 9) case.

3.3.2. Maximum count rate

The nominal limit in terms of count rate for the detector is 12 millions counts/s before activating the shut down procedure to preserve the hybrid PMT from damages. This doesn't necessarily mean that, at those count rates, the single photon statistics is still respected, hence the devices could not be capable to well determine the optical coefficients of a medium. As mentioned in section 1.2.1, a rule of thumb in order to be in the single photon statistics is to keep the count rate below 5% of the pulse rate (4MHz in case of lasers emitting at 80 MHz), but it is interesting to evaluate which is the real limit of the TD-NIRS device under analysis. In order to understand up to which count rate the detectors can be pushed still being able to correctly detect single photon arrival events, a check on the fitted value of the optical coefficients can be performed. It can be assumed that the count rate doesn't exceed the one suitable for the single photon statistics when the error on the coefficients doesn't exceed more than the 3% with respect to the optical value found for low count rates, where the statistics of the single photon is surely applicable. In order to do that, the acquisitions that have been performed span a count rate from

$500 \cdot 10^3/s$ to $11 \cdot 10^6/s$ on the board, with the minimum level of attenuation at the detector (e.g. value 9). The number of 1s acquisition is 10 for each count rate.

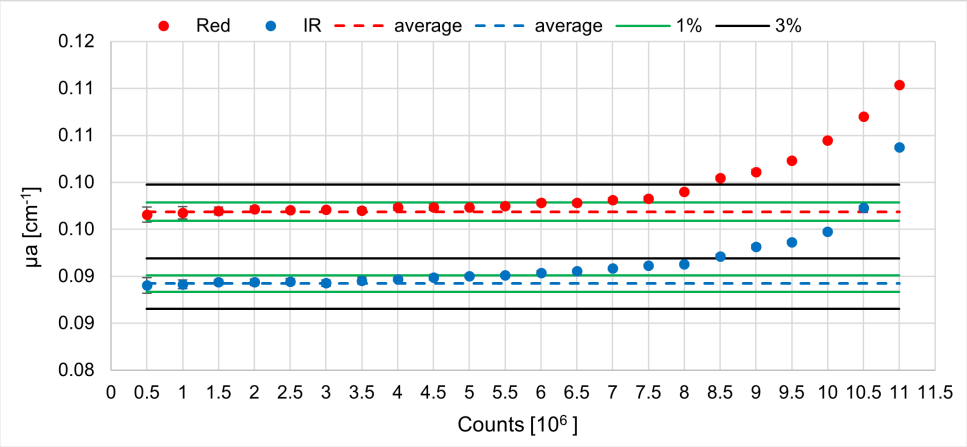

Figure 3.3: Average of the absorption coefficient over the 10 repetitions (and relative error bars) for different count rates. The horizontal axis is referred to the counts per second on the board. The dashed line is referred to the average of μ_a retrieved from 0.5 to 4 millions total counts. The green and black line represent the 1 and 3 % error regions.

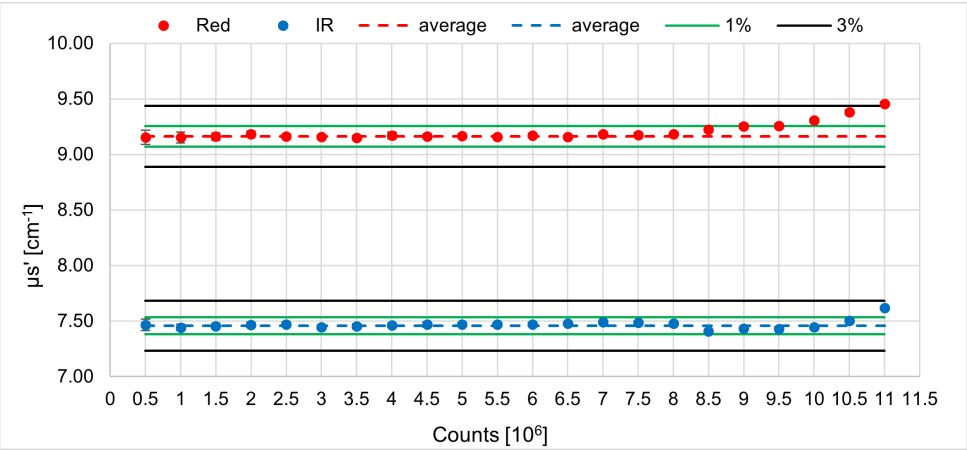

Figure 3.4: Average reduced scattering coefficient over the 10 repetitions (and relative error bars) values for different count rates. The horizontal axis is referred to the counts per second on the board. The dashed line is referred to the average of μ_s' retrieved from 0.5 to 4 millions total counts. The green and black line represent the 1 and 3 % error regions.

Figures 3.3 and 3.4 show the variation of the retrieved absorption and reduced scattering coefficients for different count rates, along with their average found for count rates spanning from 0.5 to 4 million counts/s (dashed lines) and the error regions of 1 and

3% with respect to these averages. The reduced scattering coefficient values undergoes a small variation with the increase of the count rate and never exceeds the 3% of error with respect to the average. Thus, the critical measurand in this case is the absorption coefficient, which rapidly increases both for 690 and 830 nm with the rise of the count rate. We can say that 8 millions photons per second on the board is the maximum count rate leading to acceptable estimations of the optical coefficients.

3.3.3. Variable acquisition time

The high power of the TD-NIRS device under analysis can be exploited in order to perform fast acquisitions. The typical sampling rate for the TD-NIRS devices, as most of the characterization measurements presented in this thesis work, is 1 Hz. In the state of the art, the maximum sampling rate that has been possible to reach for some in-vivo applications is 10 Hz [6][21]. Performing acquisitions with short duration could be interesting in order to follow fast changes in the values of the optical coefficients. Moreover, it could provide a tool to characterize the oscillation spectrum of the muscles and the brain cortex, which can be exploited to evaluate the effects of diseases such as brain autoregulation deficit [22].
Reducing the acquisition time, the number of photons arriving at the detector decreases, thus the minimum acquisition time to have enough photons to perform the fitting procedure and correctly retrieve μ_a and μ_s' has to be assessed. 10 repetitions have been performed on a phantom with known optical properties: $\mu_a = 0.1\,cm^{-1}$ and $\mu_s' = 10\,cm^{-1}$ at $\rho = 3\,cm$. The count rate has been set to a low value ($2 \cdot 10^8$ counts/s) first and then to an higher one ($7 \cdot 10^8$ counts/s) and then the time of acquisition has been modified in the following order: 1, 0.1, 0.05, 0.01, 0.005, 0.004, 0.003, 0.002, 0.001 s.

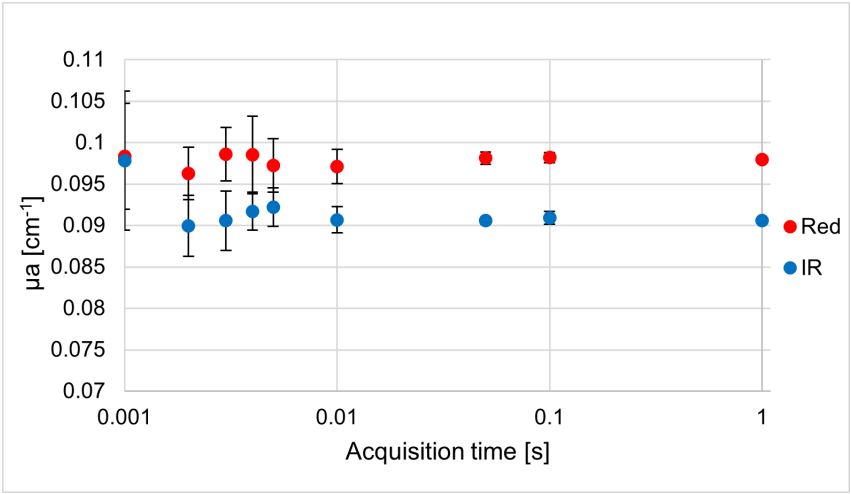

(a)

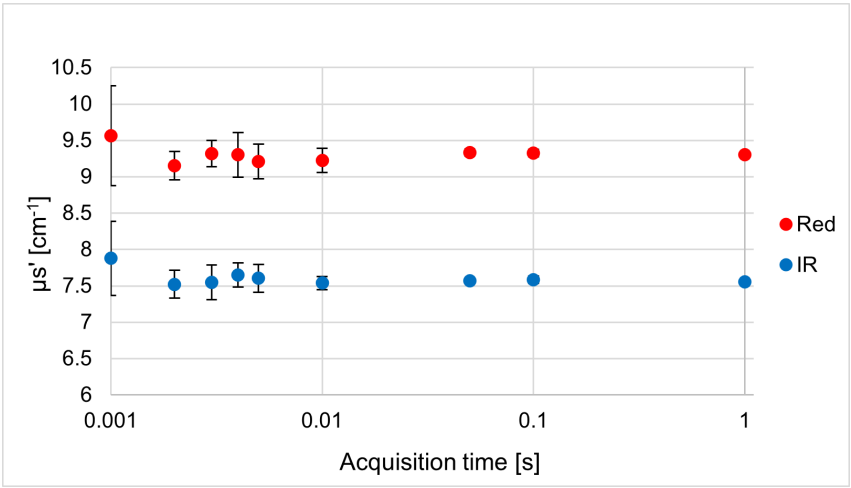

(b)

Figure 3.5: Average fitted values of μ_a (a) and μ_s' (b) over the 10 repetitions (with the relative error bars) when the acquisition time changes from 0.001 to 1s for an initial count rate of $7 \cdot 10^6$ counts/s.

Figure 3.5 shows the average fitted value of μ_a (a) and μ_s' (b) for different acquisition times and initial count rate of $7 \cdot 10^8$ counts/s. The error bars in the plot are referred to the standard deviation of the optical coefficients over the 10 repetitions. It can be noticed that, decreasing the acquisition time, the standard deviation increases, since less photons are collected and the effect of random fluctuations due to the noise becomes predominant.

To quantify the variability due to these fluctuations, the coefficient of variation CV is defined as follows:

$$CV = \frac{\sigma(\mu)}{< \mu >} \tag{3.4}$$

In eq. 3.4, σ represents the standard deviation of the measurand, while the $< \mu >$ is its average value. Generally, the maximum value accepted for the coefficient of variation is 1%.

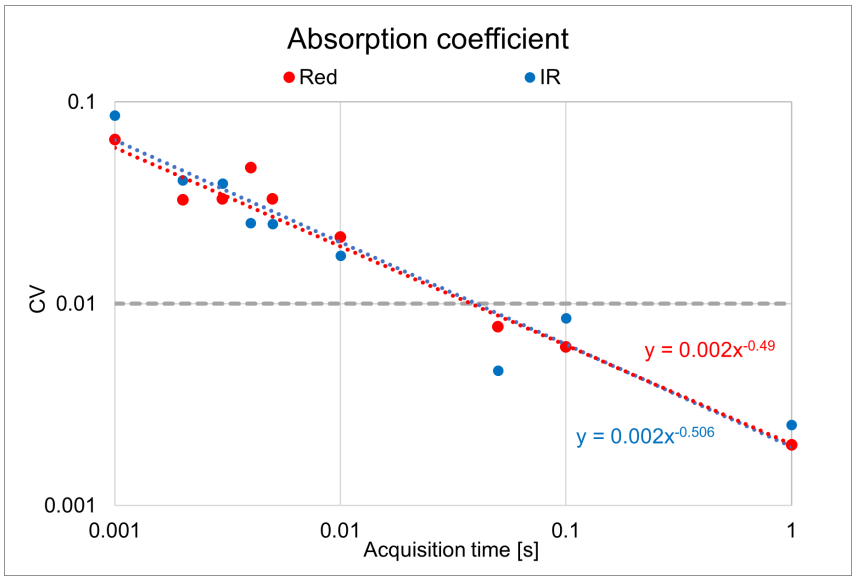

(a)

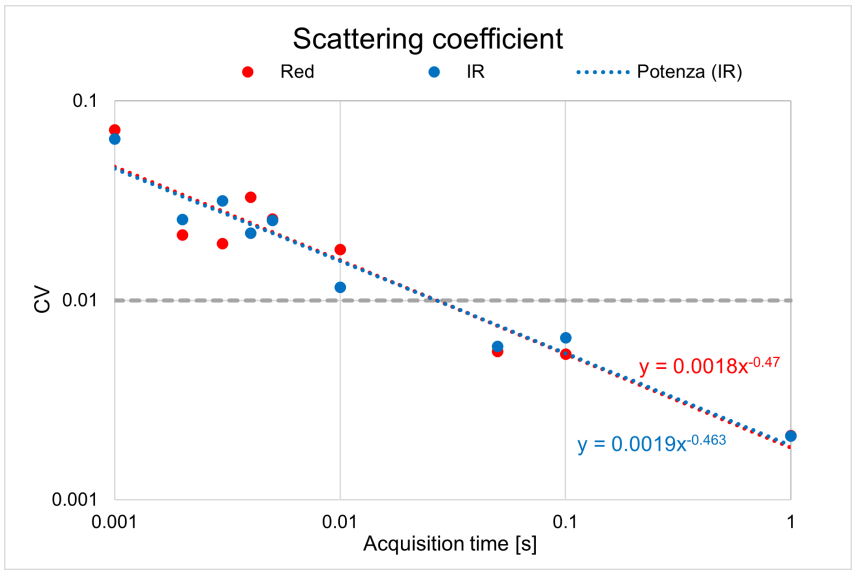

(b)

Figure 3.6: CV values for μ_a (a) and μ_s' (b) at different acquisition times and initial count rate of $7 \cdot 10^8$ counts/s. The dotted lines are the interpolation curves. The horizontal grey one, instead, refers to a 1% value of CV.

Fig. 3.6 represents the CV of μ_a (a) and μ_s' (b) versus the acquisition time and the related interpolation curves for the high count rate. The grey line, instead, represents the CV

acceptable limit. It's interesting to notice that the equations of the interpolation curves show a Poisson trend ($x^{-0.5}$) since it's known that the dominant noise in the TCSPC instruments is given by the shot noise. Qualitatively, the results found for the initial low count rate are similar, so the related plots won't be shown. As can be seen in the figures, in order to be under value of 1% CV for the two wavelengths and both μ_a and μ'_s, the required acquisition time is 0.05 s (0.1 s for the low count rate case). Acquiring for 0.05 s means that the sampling frequency on phantoms or biological tissues can be pushed up to 20 Hz. Then, the TD-NIRS device under analysis is capable of overcoming the limits of speed of the state of the art devices.

3.4. MEDPHOT

The MEDPHOT protocol has been designed in order to validate the performaces of photons migration instruments on the basis of the quality of the measurands μ_a and μ'_s. The protocol is conventionally composed by five assays:

- stability
- noise
- reproducibility
- linearity
- accuracy

Each of the steps and the relative results will be provided in the following sections.
The validation of the linearity and accuracy has been done using a set of 32 phantoms, labeled with a letter (A-D) and a number (1-8). They are cylinders (4.5 cm height, 10.5 cm diameter) and were constructed combining 4 concentrations of TiO_2 powder with 8 concentrations of toner. In this way, the values (validated at 660 nm) of μ'_s span from 5 to 20 cm^{-1} with steps of 5 cm^{-1} (phantoms from A to D) and the values of μ_a are in a range of values from 0 to 0.49 cm^{-1} with steps of 0.07 cm^{-1} (phantoms labeled from 1 to 8). In the following sections I will refer to these values of μ_a and μ'_s as nominal.
For the rest of the MEDPHOT tests, instead, a phantom labeled as T_a has been exploited: it's been prepared with the same geometry mentioned before, but with a quantity of TiO_2 and toner such as to reach the values of 0.1 and 10 cm^{-1} respectively for absorption and scattering coefficient (at 800 nm) [23].
All the phantoms have been used in reflectance geometry.

3.4.1. Stability: the warm-up time

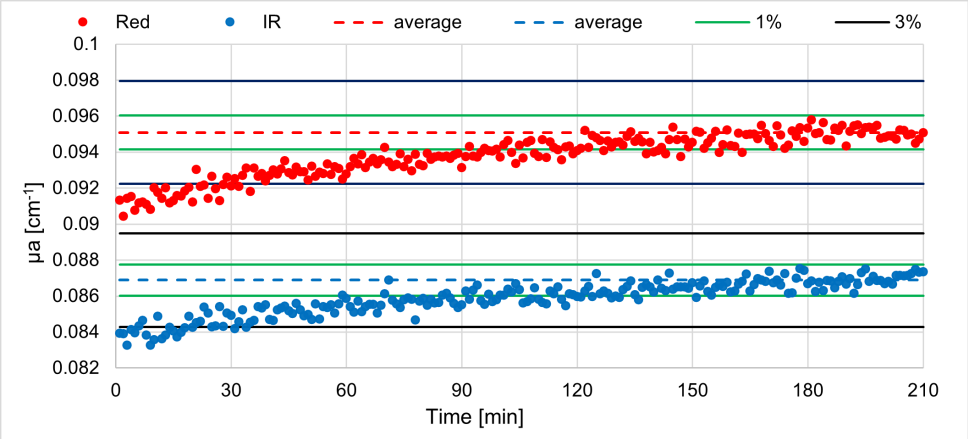

(a)

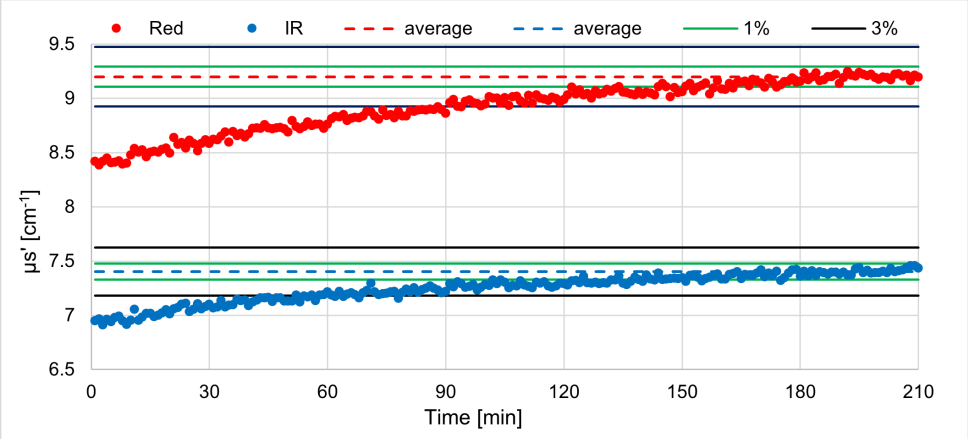

(b)

Figure 3.7: Fitted values of μ_a (a) and μ_s' (b) along 210 minutes of acquisitions after turning the instrument on. The dotted lines refer to the average over the last 30 minutes. The continuous green and black lines refer to the 1% and 3% error regions respectively.

The components that constitute the TD-NIRS device have a warm-up time, necessary to reach the stability. The main contributions to the period of warm-up is given by the detectors and by the laser sources, which are the components that take more time to reach stability. This has to be known in order to know how much in advance it is necessary to turn the instrument on before an on phantom or in-vivo measurement. The machine can be used to correctly estimate μ_a and μ_s' when the fitted values for the optical parameters are near (inside of a 3% range of variability) to the values retrieved when the instrument is stable.

In order to assess the stability of the machine, a 1 s acquisition each 60 s, for a total

duration of 210 minutes, was performed on the T_a phantom. The count rate was set at 1.5 millions counts on the board and the interfiber distance at 3 cm. In the figure 3.7 the fitted values of μ_a and μ'_s along the total duration of the acquisition are shown. The dashed lines represent the average values of the optical coefficients during the last 30 minutes of acquisition. The 1% and 3% error regions are displayed as well. It can be seen that the system requires about 125 minutes in order to reach the 1% error region for both μ_a and μ'_s, hence, the warm-up time that has been considered before all the measurements was this.

3.4.2. Reproducibility

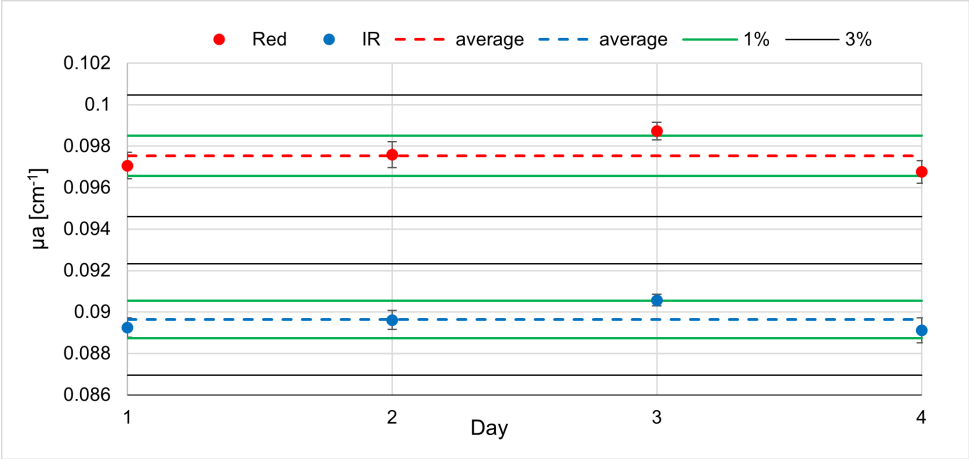

(a)

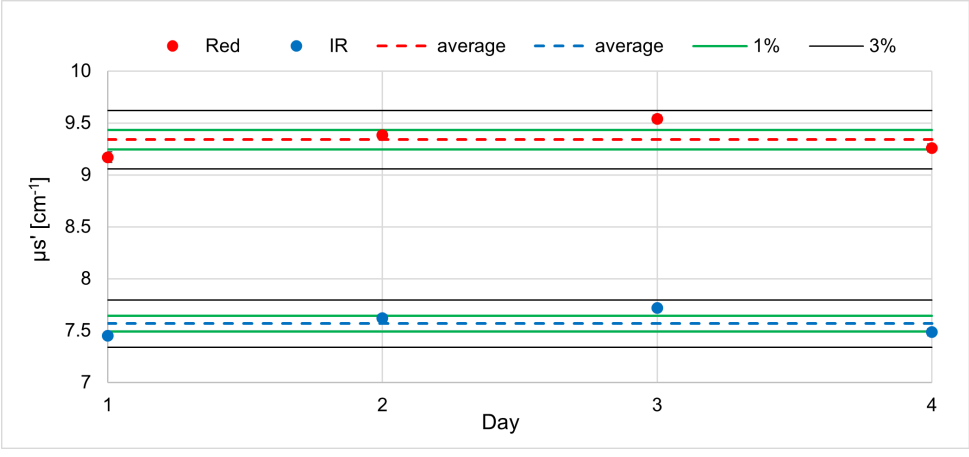

(b)

Figure 3.8: Average values of μ_a (a) and μ'_s (b) over the 10 repetitions during the four days. The dotted lines refer to the average over the whole period and repetitions. The continuous green and black lines refer, respectively, to the 1% and 3% error regions.

The reproducibility assessment is useful in order to evaluate the self consistence of the instrument with itself during different days and it is crucial if it is necessary to correlate data collected through weeks or years, for example in the case of clinical studies.

10 repetitions of 1 second each on the same phantom (T_a) were repeated in four different days, removing at the end of each 10 s measurement the probe from the phantom and placing it in the same position before each new set of acquisitions.
Fig. 3.8 shows the average on the 10 repetitions both for the absorption (a) and reduced scattering (b) coefficients. They don't exceed the average value computed along the four days and the repetitions (dashed lines) of a factor 3%.

3.4.3. Noise

The noise assessment has the goal to determine the minimum count rate needed in order to overcome the variability of the measurements due to the noise effects. For this assay, 10 acquisitions of 1 s have been performed on the phantom T_a, at interfiber distance of 3 cm with a goal in terms of count rate of 1, 2.5, 5, 7.5, 10, 12.5, 25, 50, $100 \cdot 10^4$ counts/s on the board. However, the desired goal has not always been reached because of the quantized attenuation in the detection lines, which doesn't allow a fine regulation of the number of photons arriving at the detector, especially for low count rates.
Fig.3.9 shows the average fitted values of μ_a (a) and μ_s' (b) for different count rates. The error bars in the plot are referred to the standard deviation of the optical coefficients over the 10 repetitions. It can be noticed that, decreasing the count rate, the standard deviation increases, since less photons are collected and the effect of random fluctuations due to the noise becomes predominant.

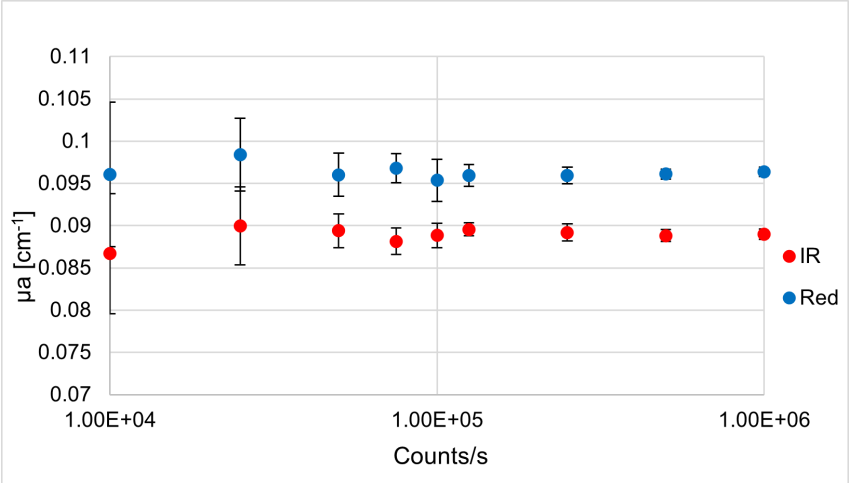

(a)

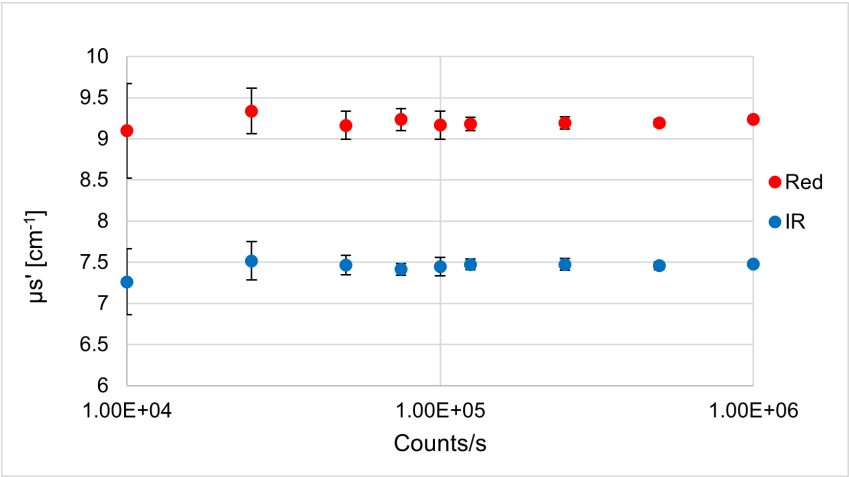

(b)

Figure 3.9: Average fitted values of μ_a (a) and μ_s' (b) over the 10 repetitions (with the relative error bars) when the count rate increases from 10^4 *to* 10^6.

To quantify the variability due to these fluctuations, the CV, already defined in section 3.3.3, has been calculated for different count rates, in order to determine which one was the minimum acceptable to perform a correct measurement. Generally, the maximum value accepted for the coefficient of variation is 1%.

Fig. 3.10 represents the CV of μ_a (a) and μ_s' (b) versus the count rate and the related interpolation curves. The grey line, instead, represents the CV acceptable limit. Clearly, the CV decreases with the increasing of the count rate, since the ratio between photons and noise is high enough to make the random fluctuations negligible. For count rates higher than 10^5 counts/s, the CV is lower than 1% for both μ_a and μ_s' at the two wavelengths. It's interesting to note that the equations of the interpolation curves shows a Poisson

trend ($x^{-0.5}$) since it's known that the dominant noise in the TCSPC instruments is given by the shot noise.

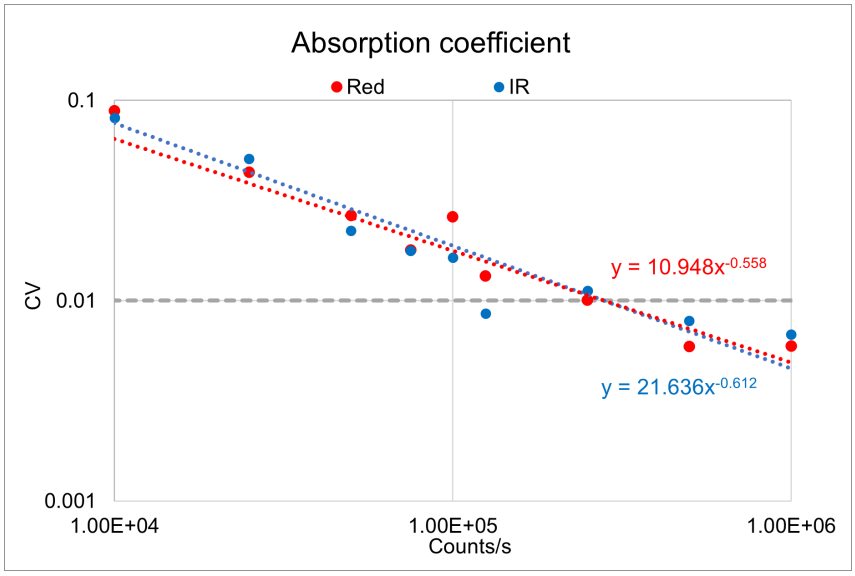

(a)

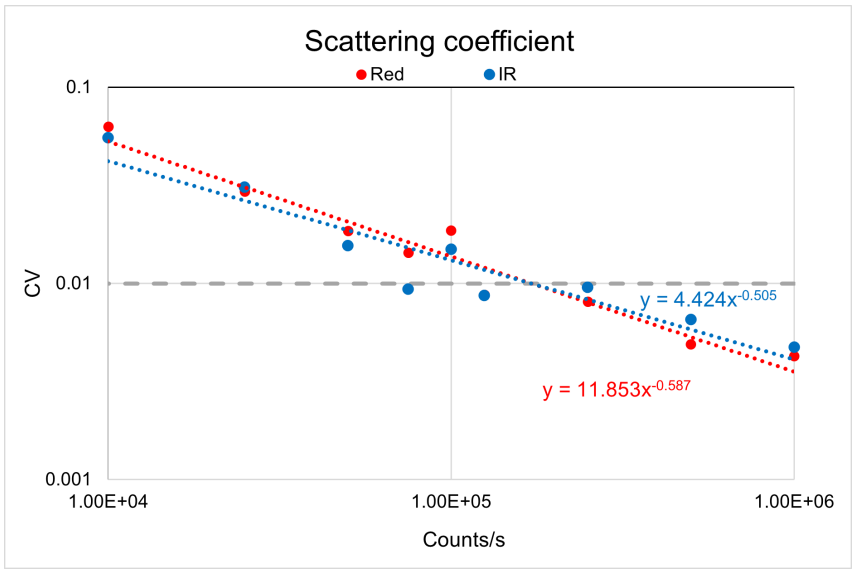

(b)

Figure 3.10: CV value of μ_a (a) and μ_s' (b) when the total count rate increases from 10^4 *to* 10^6. The dotted lines are the interpolation curves. The horizontal grey one, instead, refers to a 1% value of CV.

3.4.4. Linearity

The study of linearity tells if the TD-NIRS device is capable of linearly follow linear changes of μ_a and μ_s'.

To obtain the results shown in this section, the study of linearity has been realized performing 10 acquisitions of 1 s in reflectance geometry using all the phantoms of the MEDPHOT protocol with an interfiber distance of 3 cm. The detectors and injection attenuators have been set, for each phantom, in order to obtain a goal of $1.5 \cdot 10^6$ counts/s on the board. The acquired data have been fitted in order to retrieve, for each phantom, the wavelength dependent optical coefficients. Then, the latter have been combined into plots showing the variation of the measured coefficients versus the nominal ones ($\mu_{a,nominal}$ spanning from 0 to 0.49 cm^{-1} in steps of 0.07 cm^{-1} and $\mu_{s',nominal}$ spanning from 5 to 20 cm^{-1} in steps of 5 cm^{-1}).

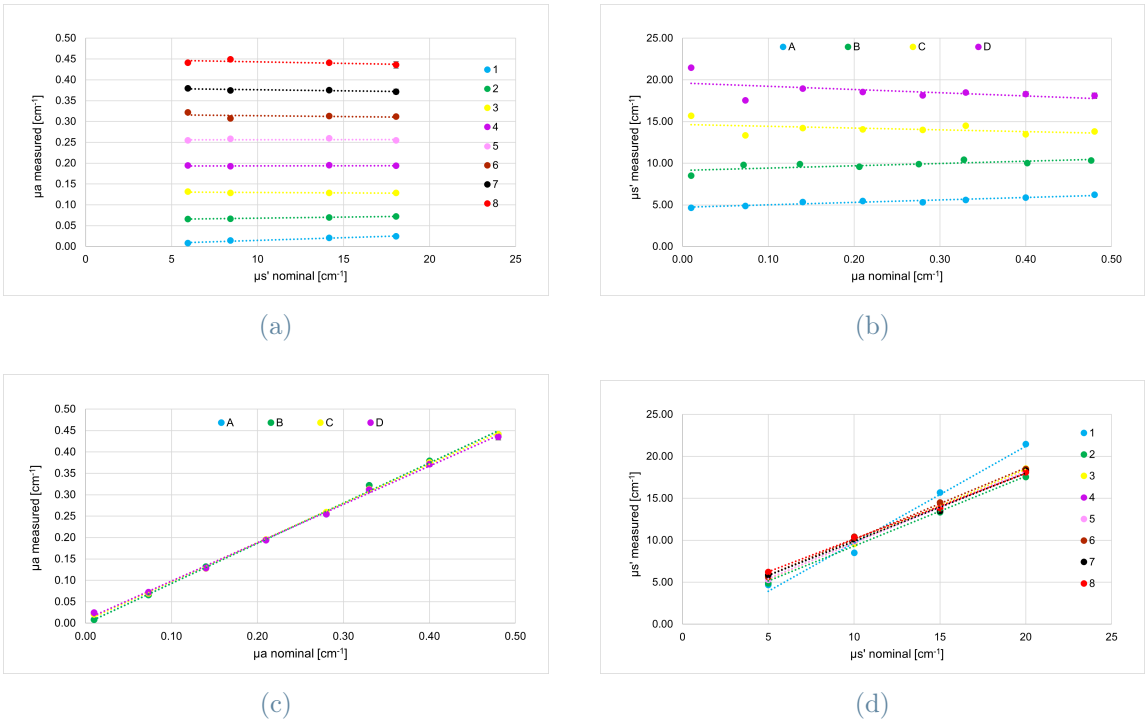

Figure 3.11: Linearity plots at 690 nm. The points represent the retrieved optical coefficients averaged on the 10 repetitions, while the straight dotted lines represent the linear interpolation of the data. Letters and numbers represent the identification labels of the phantoms.

The plots depicting μ_a versus μ_s' and vice versa are useful in order to show any presence of coupling between the two optical coefficients. Ideally, all the lines should be perfectly horizontal. In fig. 3.11 for all of the series, from 1 to 8 (a) and A to D (b), no coupling between the coefficients is observed.
The plots that show the trend of $\mu_{a,measured}$ and $\mu_{s',measured}$ respectively versus $\mu_{a,nominal}$ and $\mu_{s',nominal}$, instead, are useful to check whether the system is able to linearly follow

the changes in the absorption and reduced scattering coefficients when the values of μ_a and μ_s' are linearly increased.
In the plots in fig. 3.11 (c) and (d), these data are shown and interpolated with a linear curve. It can be observed that the measured coefficients follow the dotted lines without dispersing around them.
Similar conclusions can be drawn looking at the 830 nm case depicted in fig. 3.12.

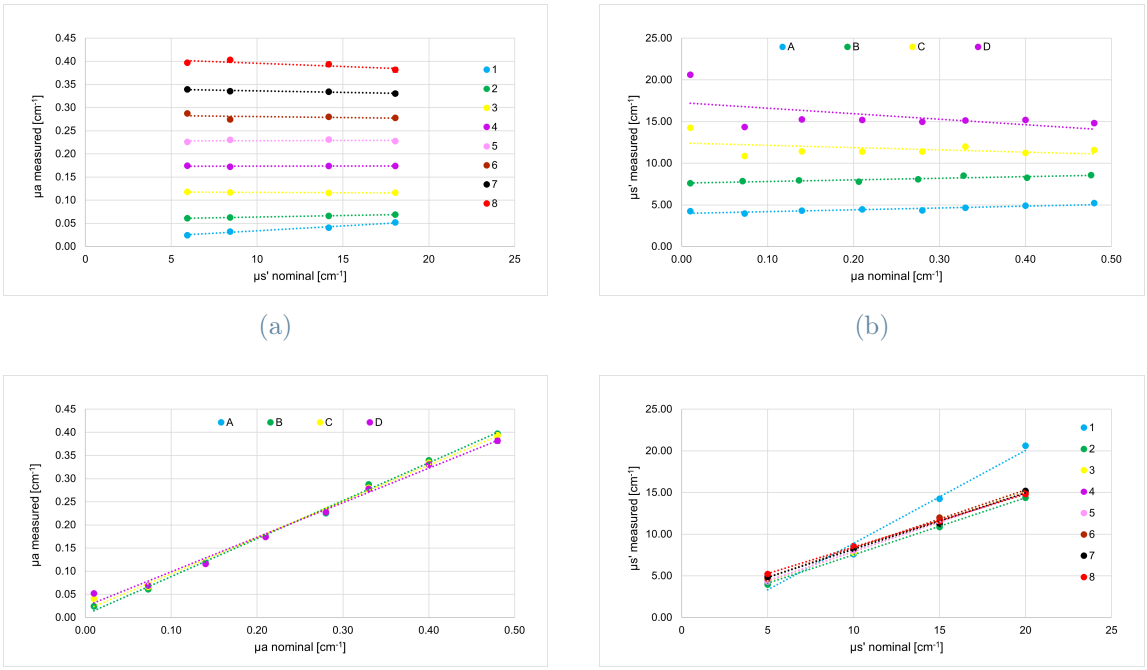

Figure 3.12: Linearity plots at 830 nm. The points represent the retrieved optical coefficients averaged over the 10 repetitions, while the straight dotted lines represent the linear interpolation of the data. Letters and numbers represent the identification labels of the phantoms.

To give a quantitative hint about the linearity of the fitted values of μ_a and μ_s', the R^2 coefficient related to the linear interpolations of figure 3.11 and 3.12 (c) and (d) are shown in tables 3.7 and 3.8 for 690 nm and 830 nm.

R^2 ($\mu_{a,measured}$ vs $\mu_{a,nominal}$)				
	A	B	C	D
690 nm	0.9982	0.09982	0.9992	0.9939
830 nm	0.9979	0.9946	0.9985	0.9573

Table 3.7: R^2 related to the linear interpolation of $\mu_{a,measured}$ vs $\mu_{a,nominal}$ for 690 nm and 830 nm.

R^2 ($\mu_{s',measured}$ vs $\mu_{s',nominal}$)								
	1	2	3	4	5	6	7	8
690 nm	0.9976	0.9962	0.9997	0.9995	0.9994	0.9978	0.9962	0.9987
830 nm	0.9816	0.9977	0.9997	0.9991	0.9997	0.9979	0.9970	0.9996

Table 3.8: R^2 related to the linear interpolation of $\mu_{s',measured}$ vs $\mu_{s',nominal}$ for 690 nm and 830 nm.

The R^2 parameter can have a maximum value of 1 in the case of total overlapping of the experimental data to the linear interpolation. It can be observed that, in the two cases shown, the coefficient is very close to 1 both for the red and IR case.
Looking at the reduced scattering coefficients in fig.3.11(b) and 3.12(b), it can be seen that they have lower values for 830 nm, as expected. In the range of 600-1000 nm, indeed, the scatteing coefficient has a decreasing trend with the increase of the wavelength [23].

3.4.5. Accuracy

In order to assess the capability of the system to well determine the optical coefficients of a sample, the relative error ϵ is used. It describes how far is the measured value from the conventionally true one.

$$\epsilon = \frac{\mu_{meas} - \mu_{conv}}{\mu_{conv}} \cdot 100 \tag{3.5}$$

Since the label values of the phantoms are validated only at 660 nm, the conventional values that have been used for the comparison are the ones retrieved from a campaign of characterization of the phantoms performed with a TD-NIRS device with a high time resolution (IRF's FWHM $\sim 200ps$) [24].

For the considered wavelengths, though, only the B series has been totally characterized, along with the phantoms A2, C2, D2 and D8 (see tables 3.9 and 3.10).

690 nm												
	B1	B2	B3	B4	B5	B6	B7	B8	A2	C2	D2	D8
μ_a	0.01	0.07	0.14	0.21	0.28	0.33	0.40	0.48	0.07	0.07	0.07	0.45
μ'_s	8.42	10.72	11.41	11.10	11.90	12.52	12.60	12.98	5.94	14.17	18.05	20.59

Table 3.9: Conventional values of μ_a and μ'_s for 690 nm.

830 nm												
	B1	B2	B3	B4	B5	B6	B7	B8	A2	C2	D2	D8
μ_a	0.01	0.07	0.12	0.18	0.23	0.27	0.31	0.38	0.06	0.07	0.07	0.39
μ'_s	6.98	8.72	9.17	8.79	9.37	9.66	9.66	9.88	4.67	11.75	14.92	16.63

Table 3.10: Conventional values of μ_a and μ'_s for 830 nm.

Hence, an assumption has been necessary: the scattering coefficients respectively of A2, C2 and D2 have been extended to all the phantoms of the corresponding series (A, C, D) and the absorption coefficients of the phantoms from B1 to B8 have been extended to the missing values of the other series from 1 to 8 (e.g. all the phantoms labeled with 1 have been assumed with the same μ_a as B1).
Tables 3.11, 3.12 and 3.13 show the relative errors of all the MEDPHOT set. The values in blue are related to the real μ, while the white ones are related to the comparison with the assumed μ.

ϵ_{sca}(%), 690 nm				
	A	B	C	D
1	-21.46	0.88	10.70	18.94
2	-17.86	-8.62	-5.81	-2.75
3	-10.08	-13.50	0.30	5.08
4	-7.87	-13.76	-0.75	2.75
5	-10.58	-16.98	-1.22	0.47
6	-5.64	-16.72	2.27	2.35
7	-0.97	-20.62	-4.86	1.38
8	4.78	-20.54	-2.45	-12.14

ϵ_{sca}(%), 830 nm				
	A	B	C	D
1	-8.91	8.93	21.37	38.18
2	-15.46	-10.01	-7.68	-3.76
3	-7.57	-13.50	-2.81	2.17
4	-4.68	-11.54	-3.03	1.79
5	-6.85	-13.99	-2.95	0.39
6	-0.58	-11.79	1.92	1.49
7	4.66	-14.47	-4.35	1.76
8	11.46	-13.30	-1.38	-10.93

Table 3.11: Relative errors of the measured reduced scattering coefficients with respect to the conventional ones. The values in blue are related to the real μ'_s, while the white ones are related to the comparison with the assumed μ'_s.

ϵ_{abs}(%), 690 nm								
	1	2	3	4	5	6	7	8
A	-16.37	-10.00	-6.04	-7.32	-9.05	-2.51	-5.16	-8.05
B	43.04	-6.16	-5.81	-6.42	-6.16	-6.29	-6.73	-5.59
C	106.68	1.19	-8.29	-7.15	-7.33	-5.18	-6.17	-8.13
D	144.03	1.91	-8.20	-7.71	-9.06	-5.45	-7.07	-3.14

Table 3.12: Relative errors of the measured absorption coefficients at 690 nm with respect to the conventional ones. The values in blue are related to the real μ_a, while the white ones are related to the comparison with the assumed μ_a.

ϵ_{abs}(%), 830 nm								
	1	2	3	4	5	6	7	8
A	143.81	-4.22	-1.69	-2.98	-1.89	6.51	9.56	4.47
B	223.98	-6.33	-4.34	-2.28	0.53	0.54	6.67	5.01
C	306.45	-0.56	-3.39	-3.25	0.37	3.69	7.78	3.55
D	421.12	3.57	-3.28	-3.43	-1.01	2.83	6.59	-1.45

Table 3.13: Relative errors of the measured absorption coefficients at 830 nm with respect to the conventional ones. The values in blue are related to the real μ_a, while the white ones are related to the comparison with the assumed μ_a.

The relative errors shown in the previous tables don't exceed the 10% in the case of the absorption coefficient of the series from 2 to 8 for both the λ and, in particular are under 7% for the phantoms that mimic the optical properties of the biological tissues (B2, B3). For the same phantoms, the errors related to the reduced scattering, instead, are higher, but still under 14%. Worse estimations of μ_s' with respect to μ_a had already been observed on previously developed TD-NIRS instruments [20].
The characterization of the whole set of phantom is still an open issue, hence it would be better for the future to refer the accuracy to real values of the optical coefficients, instead of comparing the estimations of the μ with assumed ones.

3.5. Channels homogeneity

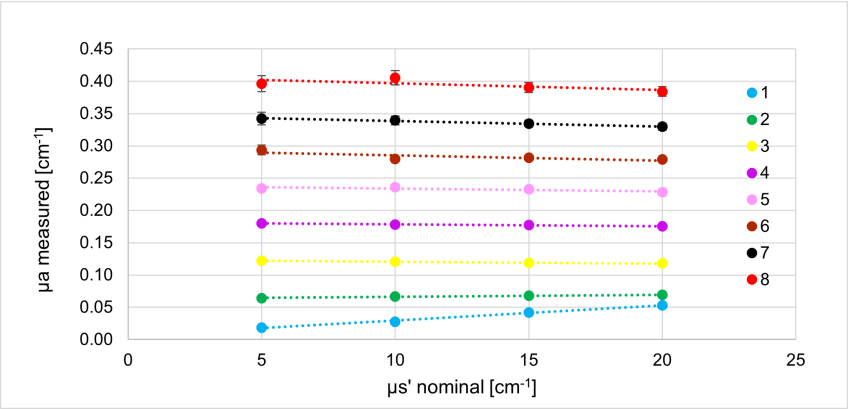

(a)

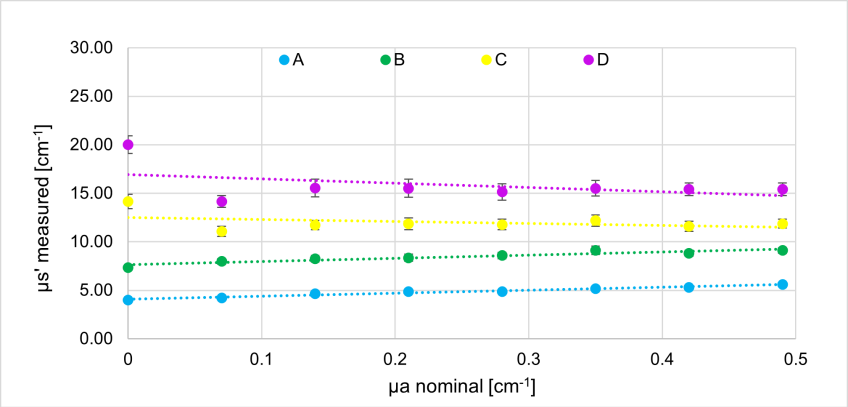

(b)

Figure 3.13: The figure refers to the average of μ_a measured with the 4 lines versus the nominal μ'_s (a) and to the average of the μ'_s measured with the 4 lines versus the nominal μ_a (b). The dotted lines are the linear interpolation of each series of coefficients. The error bars are related to the dispersion of the coefficients provided with the single lines around their average (830 nm case).

The TD-nIRS instrument under investigation has four detection lines. The previous tests have been performed only on the 4th channel, but the expectation is that all of them can be able to measure the optical coefficients with no consistent differences among each other. To check whether this is true, the acquisitions on the 32 phantoms of the MED-PHOT have been repeated for each of the detection lines at 3 cm inter fiber distance.
The goal was to assess the capability of the instrument to well predict μ_a and μ'_s independently from the chosen detector.
So, the μ_a and μ'_s of each phantom have been retrieved with the same procedure explained

in the previous sections and the average of the coefficients measured with the 4 lines is displayed in figure 3.13. The error bars which represent the dispersion of the coefficients obtained by the 4 acquisition lines around the average value are also shown. The results are shown for the 830 nm wavelength, but similar results have been obtained for the 690 nm one.

In order to quantify the homogeneity of the channels, the dispersion of the optical coefficients retrieved by the 4 lines around their average has been evaluated through the CV parameter. The latter is low for the low scattering and absorption phantoms. More specifically, taking into account the dispersion related to μ_a of the subset of phantoms from 2 to 7, the CV value is kept under 3% and around 1% for the phantoms B2, B3, B4 and C2, C3 and C4. This is a good result that, once again, confirms the performances of the instrument, mostly in the scattering and absorption values that are similar to the ones of the biological tissues.

The CV values of μ_s' don't exceed 4% for the A and B series, 5 and 6 % respectively for the C and D ones. Even if still satisfying, these results are barely worse than the ones retrieved for the absorption, but it worth taking into account that the lapping process of the collection bundles has been done manually and small differences in terms of surface of the 4 bundles could have influenced the scattering process.

3.6. Further measurements: variable inter fiber distance

Due to the good results obtained with the 3 cm ρ, it has been decided to make some acquisitions on a portion of the MEDPHOT set at different inter fiber distances to test whether, increasing the ρ, it was still possible to have enough photons at the detectors. As explained in section 1.2.3 increasing the interfiber distance can increase the probability to collect photons that have reached higher depths in the tissue, thus allowing being more sensitive to perturbations of the optical coefficients that happen in the deep regions of the sample. The distances that have been used span from 1 to 5 cm , with steps of 1 cm. Even if the goal for the measurements has been kept at $750 \cdot 10^3$ counts/s for each wavelength, the main challenge was to obtain enough counts in order to be over the noise threshold (10^5 counts/s) even at high inter fiber distances.
The bar plots in figure 3.14 show the counts obtained for each of the inter fiber distance and each of the subset of phantom that has been used.

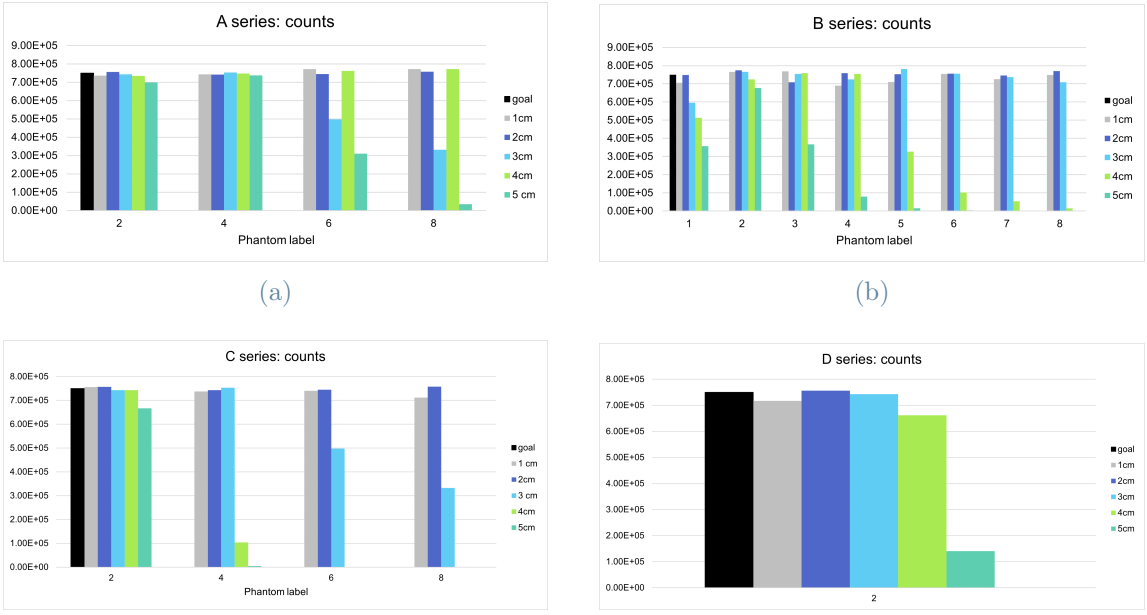

(a) (b) (c) (d)

Figure 3.14: Count rate retrieved at each source detector distance on the subset of phantoms under analysis. The black bar represents the fixed goal in terms of count rate. Bars are missing if the measure at a specific ρ and on a specific phantom didn't allow collecting photons.

It's shown that, in the case of big scattering and absorption coefficients, it's difficult for

the photons to "survive" until reaching detection points located at a longer distances than 3 cm from the injection point. So, for these samples, it's impossible to have enough counts (more than $10^5 counts/s$) to perform the fitting procedure since, as seen in 3.4.3, it wouldn't be consistent. In figure 3.14, for ρ<4 cm, the count reached is shown to be lower than the one reached at higher ρ on some phantoms (e.g. phantom A6, A8 at 3 cm). This is not due to the impossibility to reach higher count rates: it has been done on purpose to allow a better equalization between the red and IR signal (not shown here).

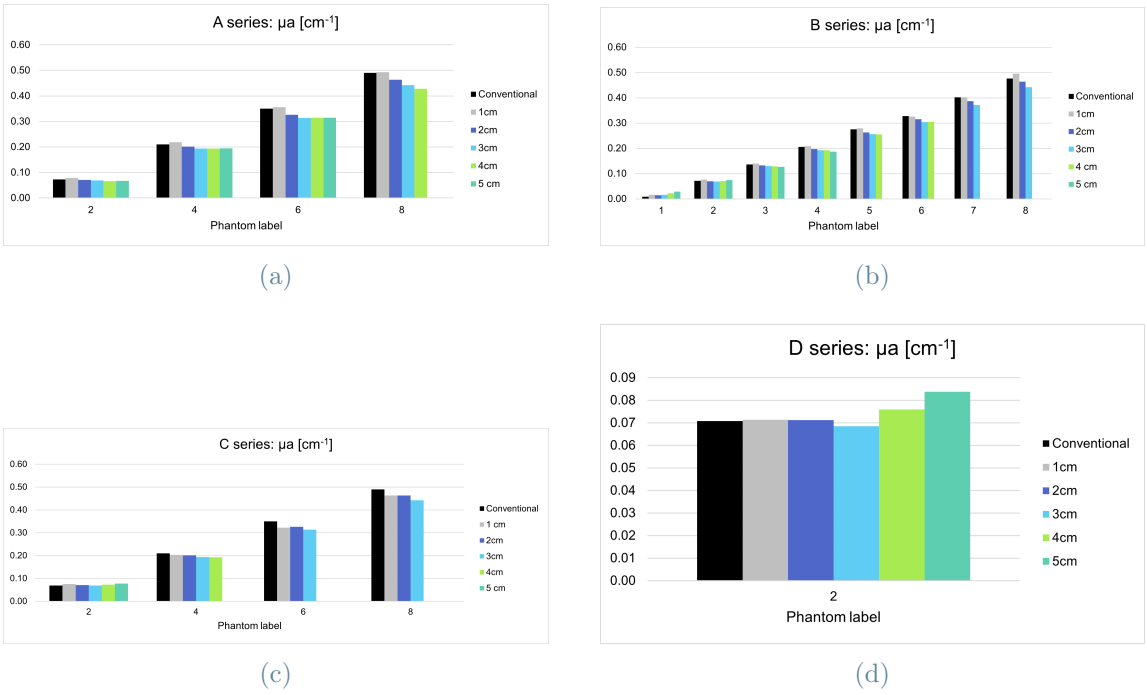

Figure 3.15: Absorption coefficients measured for 690 nm at variable inter fiber distances for a subset of phantoms compared with the conventional μ_a. Bars are missing if the measure at a specific ρ and on a specific phantom didn't allow collecting enough photons to retrieve the coefficient.

The values of μ_a and μ_s', instead, have been retrieved for those phantoms where the number of photons emerging from the phantom was enough to overcome the noise limitations. It can be noticed that, for inter fiber distances longer than 1 cm, there is an underestimation of the absorption coefficients for most of the phantom series, while the values measured at 1 cm are always the highest, overestimating sometimes even the conventional ones, as it happens for A and B series.

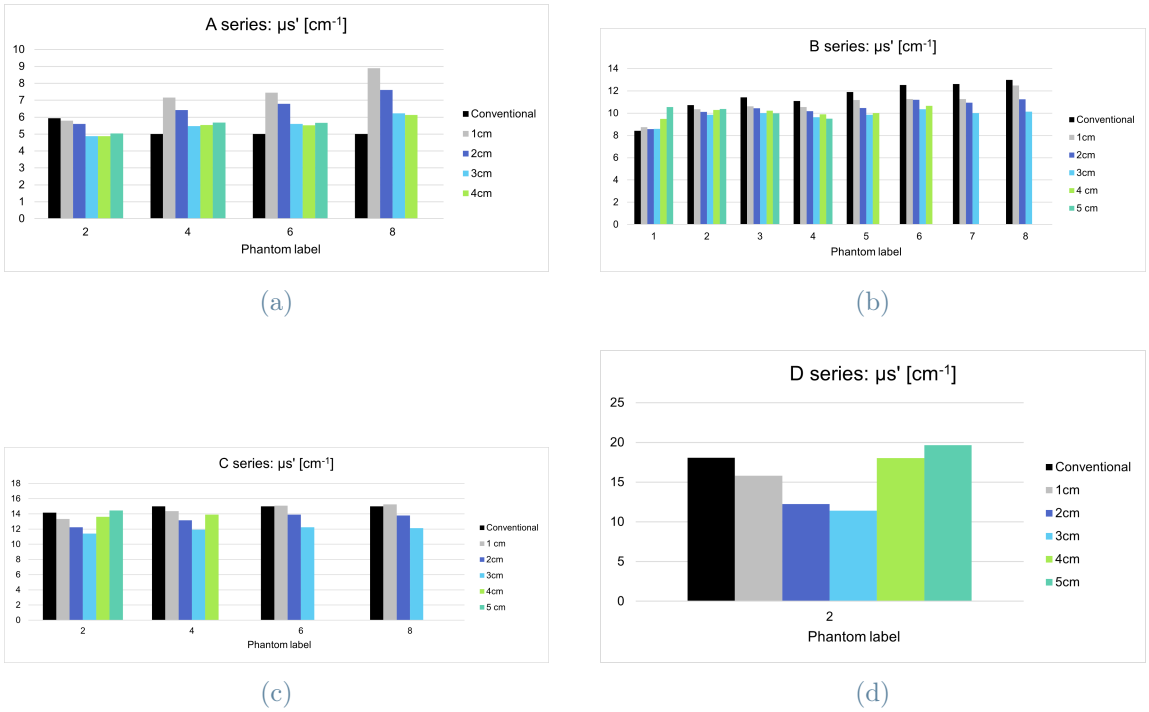

Figure 3.16: Reduced scattering coefficients measured for 690 nm at variable inter fiber distances for a subset of phantoms compared with the conventional μ_s'. Bars are missing if the measure at a specific ρ and on a specific phantom didn't allow collecting enough photons to retrieve the coefficient.

Focusing on the B series of fig. 3.16 one can notice that, for all the phantoms except B1, the fitted value of the reduced scattering coefficient is lower than the conventional one. To give a quantitative hint of the accuracy of the instrument working at all the designed configurations, the relative errors for the estimation of the absorption coefficients will be shown in the following tables for the phantoms on which the ρ allowed reaching 10^5 count/s. They will display only the errors for the B series, since, as previously said, it is the only one to be fully characterized with an high precision instrument at Politecnico di Milano.

Relative error μ_a (%) - B series								
	1	**2**	**3**	**4**	**5**	**6**	**7**	**8**
1 cm	96.9	7.7	2.1	1.3	1.4	-0.5	0.1	4.1
2 cm	67.9	-1.8	-2.8	-4.2	-4.3	-3.8	-3.7	-2.6
3 cm	91.7	-3.8	-5.1	-6.5	-6.9	-7.3	-7.6	-7.1
4 cm	159.1	-0.9	-5.9	-6.7	-7.2	-6.9		
5 cm	239.8	4.1	-7.0	-9.2				

Table 3.14: Relative errors for the μ_a of the B series at variable inter fiber distance. The empty cells refers to phantoms on which the specified inter fiber distance has made impossible to retrieve a sufficient count rate to extract the optical coefficient.Values related to 690 nm.

Relative error μ_a (%) - B series								
	1	**2**	**3**	**4**	**5**	**6**	**7**	**8**
1 cm	55.7	10.1	8	10.2	14.3	12.3	19.3	15.6
2 cm	57.9	-2.8	-1.7	-0.2	2.4	2.9	9.8	8.3
3 cm	122.6	-3.4	-3.3	-2.2	0	-0.5	5.3	3.1
4 cm	206.7	0	-4.1	-2.3	-0.7	-0.5		
5 cm	386.7	8.2	-4.1	-3.3				

Table 3.15: Relative errors for the μ_a of the B series at variable inter fiber distance. The empty cells refers to phantoms on which the specified inter fiber distance has made impossible to retrieve a sufficient count rate to extract the optical coefficient. Values related to 830 nm.

Please notice that the relative errors displayed here for the 3 cm case are different from the ones displayed in tables 3.12 and 3.13, since they refer to acquisitions performed in different days. However, their variation doesn't overcome the limits of reproducibility that has been assessed for the TD-NIRS instrument (3.4.2).

3.7. NEUROPT

The most powerful capability of a TD-NIRS instrument is the one to be able to detect, localize and measure the variation of the absorption coefficient in the human tissues under analysis. Knowing this variation can be useful to treat a signal, removing the influence of the surrounding medium. After describing the Basic Performances of the Instrument

with the BIP protocol and the capability of correctly measure the optical coefficients of an homogeneous medium through the MEDPHOT, nEUROPt is the following step to assess the sensitivity of an optical imager to $\Delta\mu_a$. Among the parameters that can be quantified in the frame of this protocol, the one that will be mainly investigated is the contrast (section 3.7.2).

3.7.1. The liquid phantom and inclusions

To perform nEUROPt protocol, a liquid phantom has been used. It is made by a liquid solution with the desired optical properties in which a solid inclusion of variable dimensions is inserted. The advantages of using a liquid phantom are [25]:

- Ease of simulating different geometries, thanks to the possibility of gradually and freely moving the absorbing inclusion in the liquid;
- The optical propeties of the liquid phantom is easily reproducible, since it is made with well known constituents whose optical coefficients remain stable for a long time.

In our specific case, the phantom has been made with the following components and quantities:

- Distilled water: 5892 ml
- Intralipid solution (Fresenius Kabi, 20%): 265 ml
- Black Ink (Diluition factor: 7.09210^{-3}): 48 ml

in order to obtain the following optical values for the homogeneous phantom: $\mu_a = 0.19\,cm^{-1}$ and $\mu_s' = 10.09\,cm^{-1}$ at 690 nm. The actual value of coefficients that has been retrieved is, instead, $\mu_a = 0.19\,cm^{-1}$ and $\mu_s' = 10.82\,cm^{-1}$. This value has been calculated in the first day of measurements, when the phantom had recently been prepared, in order to avoid the influence of contaminations that could have occurred because of the measurements and because of the process to store the phantom in the tanks to keep them in the fridge between two subsequent days. The difference between the desired and retrieved value of the absorption coefficient of the homogeneous phantom is 2%, while for the reduced scattering one it is about 7%, which are comparable with the values of accuracy found for the B series (similar for optical coefficients to the liquid phantom) in section 3.4.5.
The obtained solution has been placed in a 17cm x 25cm x 20cm glass tub with a customized system of fiber holders placed at various inter fiber distances, according to the

requirement of the measurement.
The role of the inclusions, instead, is to simulate a perturbation in the absorption. The principle which is used is the one of the EBV (equivalent black volume): it has been shown [26] that there is an equivalent relation in the changes of the photon time distribution produced by a realistic inclusion and a total absorbing object with a specific volume.
Two totally absorbing PVC inclusions of different sizes have been used separately, each one with the diameter equal to the height:

- Inclusion A: $4\,mm$ size, 50 mm^3 and $\Delta\mu_a = 0.0087\,mm^{-1}$
- Inclusion B: $8.6mm$ size, 500 mm^3 and $\Delta\mu_a = 0.094\,mm^{-1}$

They were connected to a slit through thin and rigid metallic wires, with diameter of 0.5 mm painted with white colour in order to not affect the measurements. The slit was electronically controlled by an USB connection to the PC. It allowed precise movements in x, y and z direction and, its integration in the software, allowed the automatization of the measurement along many discrete positions.
The acquisitions were taken in different positions, scanning a wide region starting from the level of the optical fiber tips and going down for the first 3 cm along the z direction (e.g. perpendicularly to the fiber holder basis) with steps of 1 mm and for further 3 cm with steps of 2 mm.
Since the MEDPHOT revealed good results for inter fiber distances from 1 to 5 cm, the same ρ have been used in this protocol. The goal for the count rate was set to 2 and 8 millions counts/s per board on the homogeneous phantom. Clearly, this was possible only for the first three source-detector distances, while it wasn't possible to reach the goal in the case of 4 and 5 cm.

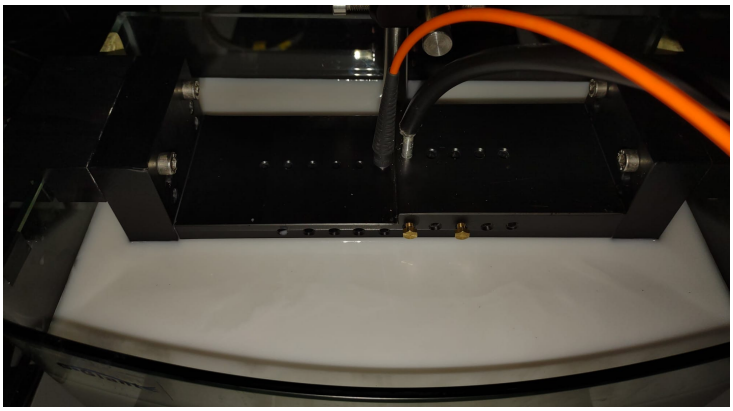

Figure 3.17: Detail of the fiber holder for the NEUROPT measurements.

3.7.2. Contrast

The measurand on which the attention will be focused for the characterization of this TD-NIRS instrument is the number of collected photons N. It will depend on the depth z of the inclusion with respect to the source and detector fibers. The contrast depends on the ratio between $N(z)$ and N_0, which is the number of photons arriving at the detector when the inclusion is far enough to consider the phantom homogeneous.

$$C(z) = -\ln \frac{N(z)}{N_0} \tag{3.6}$$

Observing the number of photons arriving at the detector as a function of the depth of the inclusion (fig. 3.18), it's possible to see that count rate is constant when the depth is higher than 3 cm. As a consequence, the N_0 value is the average between the N collected along the acquisitions performed at the last 2 centimeters of depth.

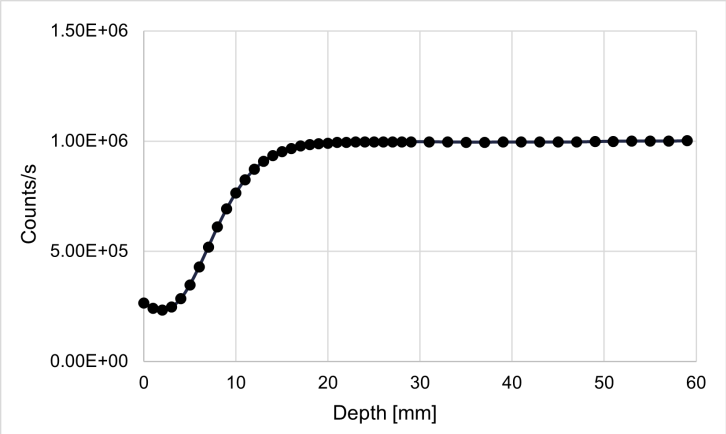

Figure 3.18: Counts/s versus depth of the inclusion.

Figure 3.19 depicts an example of contrast for the B inclusion, $\rho = 3\,cm$ set at a count rate of $2 \cdot 10^6$ counts/s on the homogeneous phantom. Each of the gates (7 in total) is large 500 ps and all of them span a temporal window that starts from 500 ps before the peak of the IRF and 3000 ps after it.
The width and the number of gates that has been chosen is large enough to follow the dynamics of the photons for all the inter fiber distances.
The yellow curve of fig. 3.19 represents a single gate spanning all the time window that the sum of the 7 gates span. It has been displayed in order to make visible the enhancement offered in the time gating approach. The higher order gates see a non null contrast for higher depths of the black volume than the single gate case.

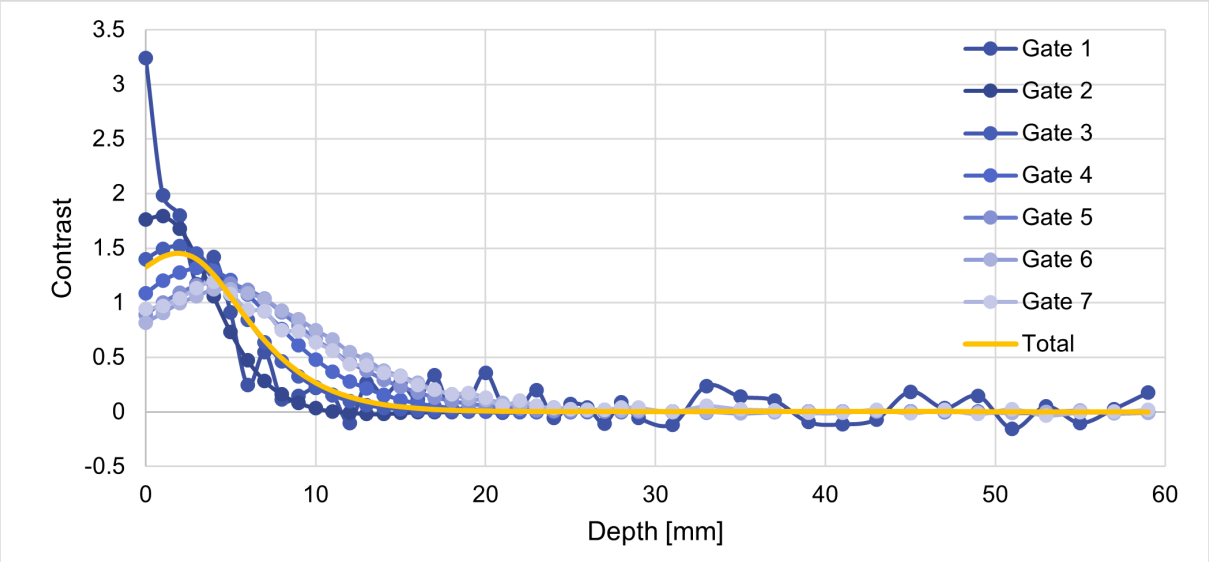

Figure 3.19: Example of contrast obtained with the inclusion B at ρ=3cm. The blue curves represent the contrast for each of the chosen time gates. The yellow curve, instead, represents the contrast computed on a single large gate covering the same time window of the sum of the narrower 7.

As shown in chapter 1, the IRF peak position depends on the ρ of the acquisition. The larger the inter fiber distance, the more delayed is the maximum of the reflectance curve and with it, also its rising edge, since photons have to travel along a longer path in order to reach the detector.

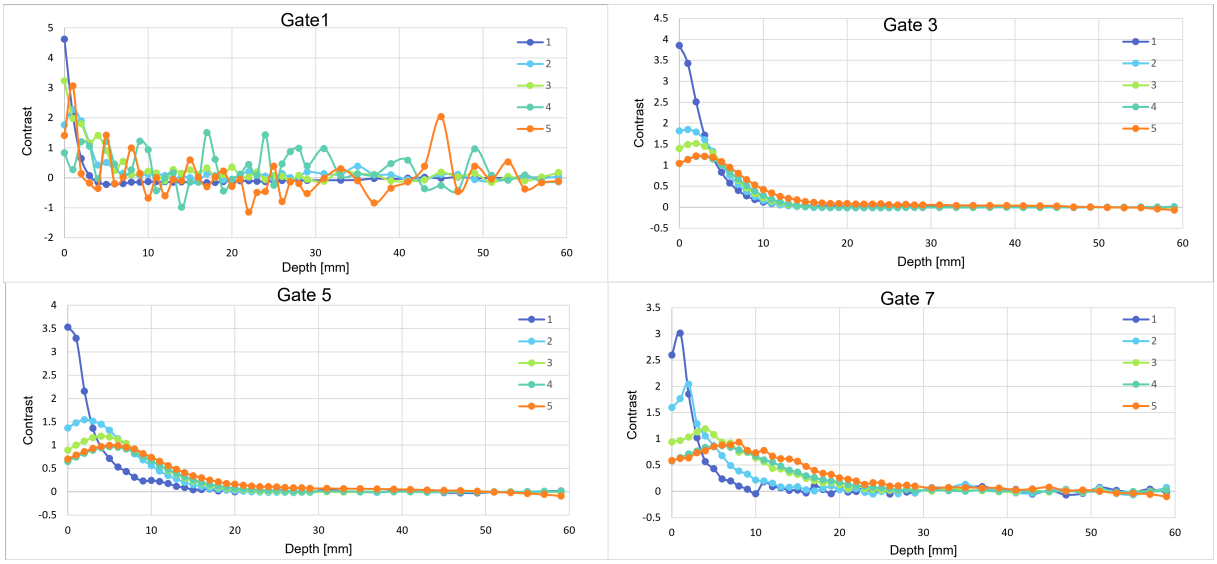

Figure 3.20: Gates at all the inter fiber distances shown for the B inclusion. Curves referred to 690 nm.

This can explain why in fig. 3.20, the first gate shows a noisy curve for the two largest ρ: in the corresponding amount of time, the number of photons arriving at the detector is still buried into noise.
With the same principle the reason why in the last gate the most noisy curves are the 1 and 2 cm ones can be explained: the overall reflectance profile is shifted to smaller delays, so in the position of the last gate the curve has already decreased enough to be disturbed by the noise.

Late gates refer to photons with a longer time of flight than the ones collected in the early gates. Traveling for a longer path, these photons have more probability to reach higher depths in the sample, thus reporting the presence of deep absorbing objects. This can be noticed in the plots of fig. 3.20 observing the depth where the contrast curve settles to 0. The orange curve of the gate 3, for example, shows a null value of contrast from about 15 mm depth, then this depth increases respectively to about 20 and 25 mm for the gates 5 and 7.
If the attention is focused on a single gate, for example GATE 3, where none of the curves is noisy, one can see that for small depths, the ρ equal to 1 and 2 cm show a better contrast than the bigger ones, while the curves obtained at 4 and 5 cm decay more slowly to 0 going toward the increasing direction of the depth axis. This is due to the fact that, if the detector is near the source, it has more probability to collect photons with a small time of flight with respect to a configuration where the detector is away from the source. Photons with a small time of flight reach shallow depths, so they notice the change in absorption if it happens near the surface of the liquid. The photons that go deep in it, instead, undergo more scattering events, arriving at an higher distance from the source position with a large delay: they are sensitive to deep changes of absorption and they are more probably collected at higher ρ.

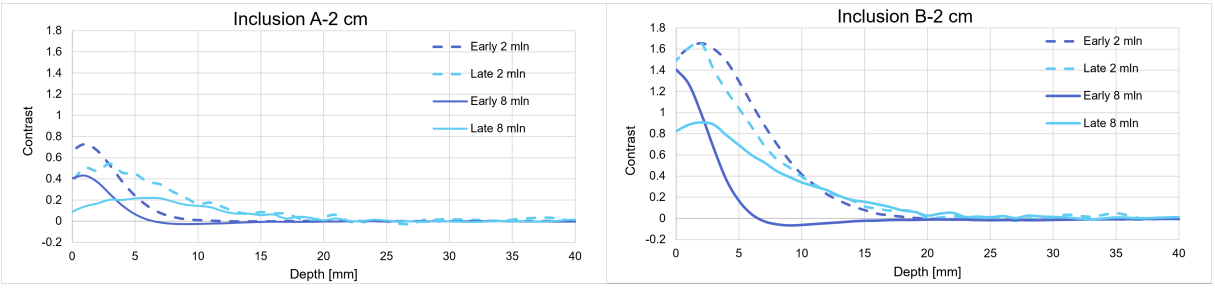

Figure 3.21: Contrast shown at 2 cm inter fiber distance for both the inclusions at high and low count rates. Early refers to photons collected in the 1 ns time window of the first two gates and late to the ones reaching the detector in 1 ps of the last two gates.

As said, inserting a black volume in the homogeneous phantom simulates a variation of the absorption coefficient. Clearly, a bigger inclusion determines a bigger variation and consequently a bigger contrast. In fig. 3.21, the original first and last two gates have been joined together to display the behaviour of the contrast for the early and late photons. One can observe that, for a fixed position of the black volume, the A inclusion determines smaller values of contrast than the B one, as expected.
The unexpected behaviour is the negative contrast that can be observed for both the inclusions in the early curve at 8 million counts/s. Even if it hasn't been shown, this occurs for all the high count rate acquisitions at all the source detector distances between the region of depth 6-15 mm. This could be caused by both unwanted effects happening at the interface between the white wire and PVC or reflection events due to some component of the metallic support. Further investigations are needed.
Another unexpected result is the difference of contrast observed for the same inclusion, at the same ρ, the same depth of the absorption variation for low ($2 \cdot 10^6$ counts/s) and high ($8 \cdot 10^6$ counts/s) count rates. At $8 \cdot 10^6$ counts/s we are in the limit of counts to prevent the signal from the distortion due to the pile up effect. In order to verify whether to attribute the difference of observed contrast to a distortion of the DTOF curve, it may be necessary to perform the nEUROPt protocol measurements setting the count rate at variable values below $8 \cdot 10^6$ counts/s.

4 | In vivo measurements

After the assessments of the TD-NIRS device through the standard and addictional protocols described in chapter 3, some preliminary in-vivo measurements were carried out in order to validate the performances of the instruments tracking the hemodynamics. Two experiments were conducted on the forearm, in order to follow the hemodyamics in the muscle during a baseline state and arterial cuff occlusion. Other measurements were performed on the head to follow the variation of HHb and O_2Hb concentration in the brain cortex during a resting state and a motor activity. Measurements were done on a male healthy volunteer, in accordance with the declaration of Helsinki.

4.1. Muscle

Two measurements were performed on the internal side of the left forearm of the volunteer: a baseline state measurement and an arterial occlusion.

Figure 4.1: Setup for the acquisition performed on the arm.

The volunteer was asked to seat and rest with the arm under measurement placed approximately at the height of the heart and the probe was fixed through black self adhesive bandages to the internal side of the forearm as shown in fig. 4.1.
Both the measurements had a total duration of 600 s at a sampling rate of 20 Hz. The probe that was used allowed the simultaneous acquisition of 4 different interfiber distances: from 2 to 5 cm with steps of 1 cm. As seen in chapter 3.1.2 and 3.6, the number of photons arriving at the detector depends on the responsivity of the channel and also on the source-detector distance: e.g. longer ρ or channels with lower responsivity collect less photons. The collection bundles of the detection lines have been placed at the four inter-

fiber distances taking into account the previous considerations to equalize and optimize the number of photons being detected through each channel.

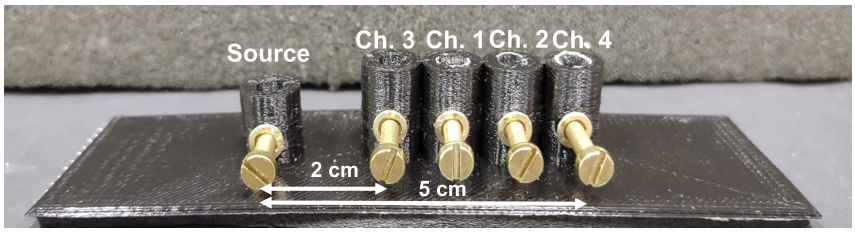

Figure 4.2: Configuration of the probe in the in-vivo measurements.

Thus, channel 3, which showed the worst responsivity (chapter 3.1.2), has been placed at the shorter distance (2 cm) from the source, channel 1 at a distance 3 cm and channels 2 and 4, the two best channels in terms of responsivity, at 4 and 5 cm respectively (fig. 4.2). As a result, the count rate reached on the total board has been of about $7 \cdot 10^6$ counts/s for channel 1, $5 \cdot 10^6$ counts/s for channels 2 and 3 and $7 \cdot 10^5$ counts/s for channel 4. The data have been fitted through an homogeneous model to get μ_a and μ_s' and then, implementing through a MATLAB code the relations of chapter 1.1.3, the concentrations of O_2Hb, HHb and tHB and the parameter SO_2 have been retrieved.
A moving average of order 20 has been applied to the retrieved hemodynamic parameters.

4.1.1. Baseline acquisition

The first acquisition was performed on the arm being still and non contracted for the whole duration of the experiment. No external pressures or stimuli were applied.

Average baseline values				
ρ	$O_2Hb\,[\mu M]$	$HHb\,[\mu M]$	$tHb\,[\mu M]$	$SO_2\,[\%]$
2 cm	102.7	44.0	146.8	70.0
3 cm	118.6	50.2	168.8	70.3
4 cm	103.7	46.3	150.0	69.1
5 cm	88.5	39.0	127.5	69.4

Table 4.1: Average of the concentration of O_2Hb, HHb, tHb and saturation SO_2 over the first 120 s of the baseline acquisition at the four ρ.

Table 4.1 shows the average concentrations of O_2Hb, HHb, tHb and SO_2 during the first 120 s of the baseline acquisition. The value of the average baselines is provided for each of the ρ. Looking at the values of concentration of oxy, deoxy and total hemoglobin, it

can be seen that these parameters present the same variability among them. In the case of 2,3 and 4 cm this variability is comparable with the one retrieved for the assessment of the channel homogeneity (chapter 3.5). The case of 5 cm, instead, will be treated in detail in section 4.1.2. SO_2 is less variable for all the detection lines, being the ratio between the concentrations of O_2Hb and tHb.

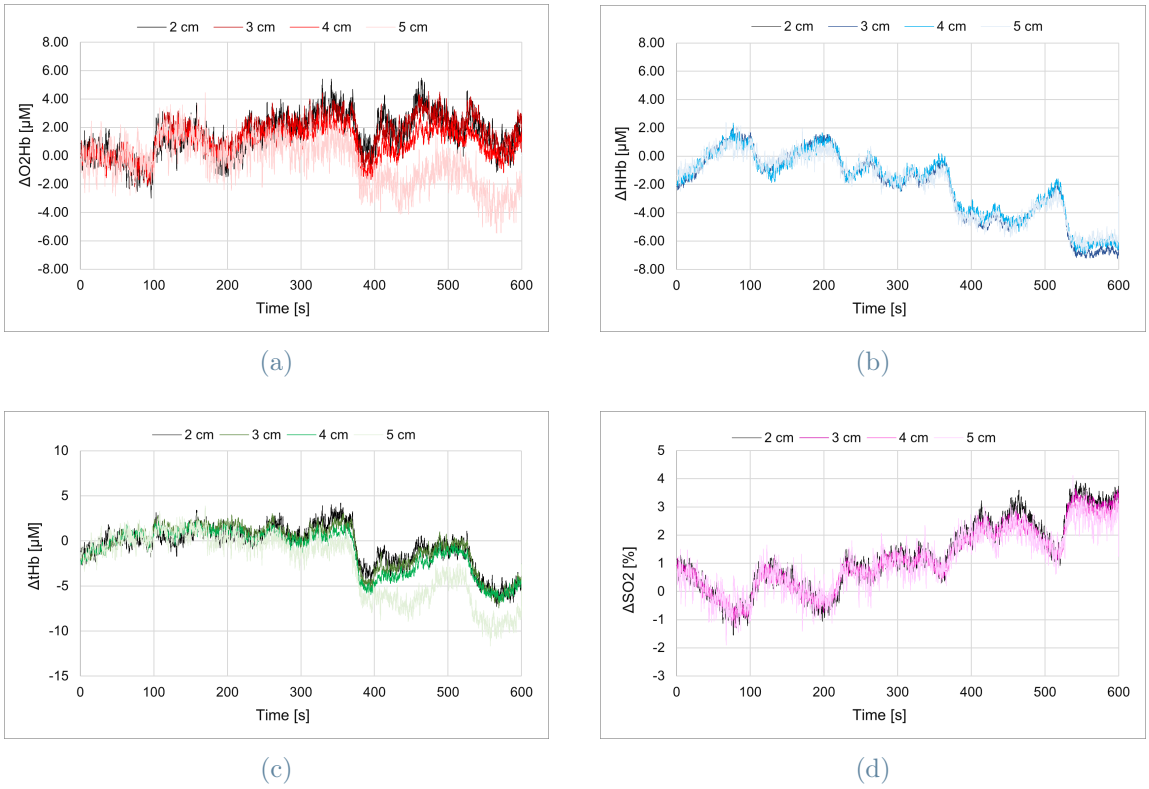

Figure 4.3: Variation of concentration of O_2Hb (a), HHb (b), tHb (c) and saturation SO_2 (d) during the resting state of the arm. Variations related to the average value of the parameters in the first 120 s of acquisition.

Figure 4.3 shows the relative variation of the concentration of O_2Hb (a), HHb (b) and tHb (c), along with SO_2(d). The variations are calculated with respect to the average values assumed by these parameters in the first 120 s of acquisition, assumed as baseline. It's interesting to notice how the values of the concentrations oscillate around the baseline with low frequencies. These fluctuations could be closely related to autonomic physiological processes, i.e. changes in cardiac rate, respiratory volume or systemic modulation of the blood flow [27].
Regardless of the fluctuations, the expectation is that the variations of the parameters keep around the 0 value for the whole duration of the experiment, since no external stimuli are being applied. However, around 350 s, an unexpected variation of the oxy and

deoxy-hemoglobin concentrations, with consequences on the values of total hemoglobin concentration and saturation is recorded. An active contraction of the muscle by the volunteer would have led to an decrease of the O_2Hb and an increase of HHb. Since after 350 s this is not verified, the active contraction is excluded. A pressure exerted by the probe on the arm due to an unwanted change of its position or a passive response to a physiological extra-muscular stimulus can be possible explanations of the variation of the parameters. Another observation to make is that the maximum amplitude of the variation for 5 cm is higher with respect to shorter ρ. A possible explanation to this behaviour will be provied in section 4.1.2.

4.1.2. Muscle: occlusion

A standard arterial cuff occlusion was performed on the volunteer. The occlusion was executed on the left arm with a pressure value of 250 mmHg.

The measure was composed by 120 s baseline, 180 s occlusion and 300 s recovery.

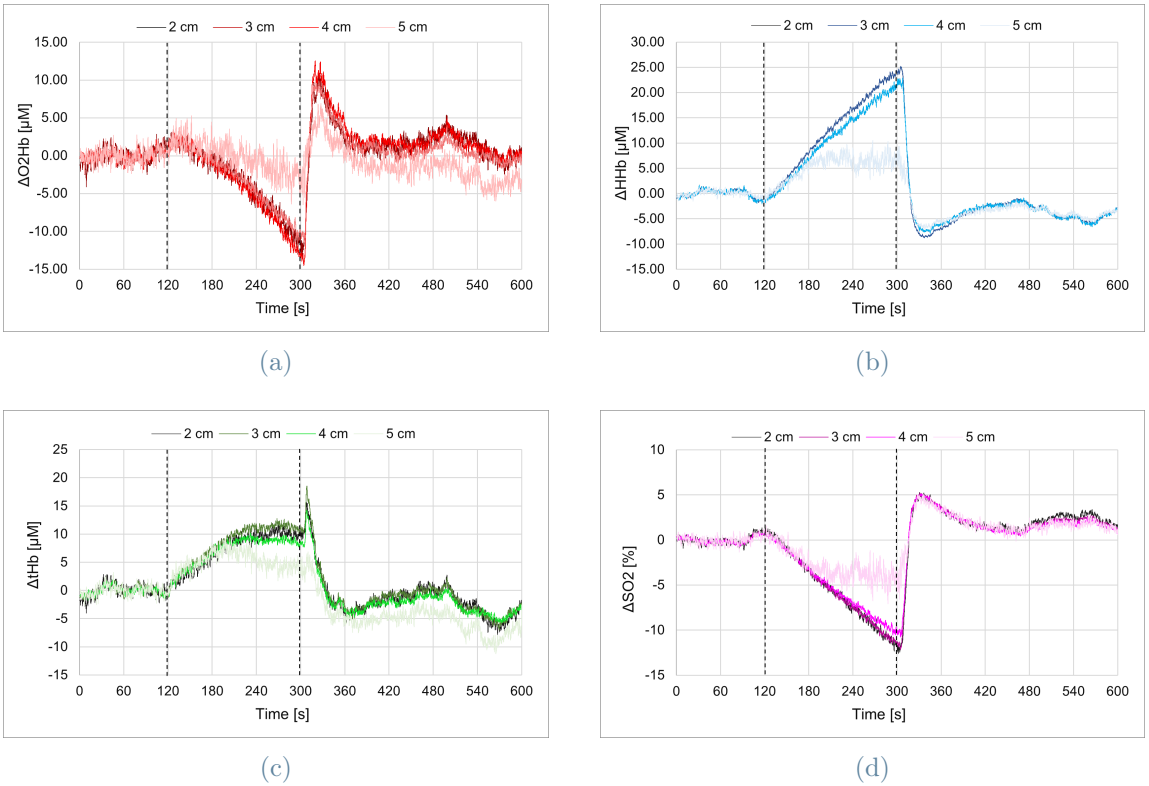

Figure 4.4: Relative variation of concentration of O_2Hb (a), HHb (b), tHb (c) and SO_2 (d) during the occlusion experiment. Variations respect to the average value of the parameters in the first 120 s of acquisition in the three stages of measurement: baseline from 0 to 120 s, occlusion from 120 to 300 s and recovery from 300 to 600 s.

In fig.4.4 the relative variations of the concentrations for O_2Hb, HHb, tHB and of SO_2 are represented in the three different phases of the protocol for all the interfiber distances: baseline from 0 to 120 s, occlusion from 120 to 300 s and recovery from 300 to 600 s. These variations are referred to the the baseline values, retrieved averaging the concentrations and saturation values found in the first 120 s of experiment, i.e. before practising the occlusion. The absolute baseline values of the occlusion measurement don't differ from the ones in table 4.1 so, for sake of simplicity, they will be omitted. Figure 4.4 (a) and (b) show that before 120 s, the variation of the concentration of O_2Hb and HHb is oscillating around the null value. During the occlusion, the flow of arterial (venous) blood is inhibited. Hence, the oxygenated (deoxygenated) blood cannot reach (leave) the muscle, thus resulting in a decrease (increase) of the value of O_2Hb (HHb). After releasing the cuff at 300 s, a peak, known as hyperemia, is observed before the variations go toward the baseline value again. Figure 4.4 (c) shows the variation related to the total concentration of hemoglobin. When the cuff is inflated, this value increases since, even if no oxy-hemoglobin can enter the tissue through the arteries, the deoxy-hemoglobin doesn't leave through the veins, thus resulting in an overall increasing of the total concentration. For the same reason, the ratio between O_2Hb and tHb decreases during the arterial occlusion, as shown in fig. 4.4 (d).

It can be observed that the curve referring to 5 cm is the most noisy one, due to the lower count rate that has been reached. Moreover, even if this curve follows the qualitative trend relative to shorter interfiber distances, the maximum variation of the hemodynamics parameters is smaller than the ones retrieved for smaller ρ. The count rate at the 5 cm configuration is lower than the others, and for each acquisition of 50 ms, the collected photons are about $35 \cdot 10^3$ on the board, less than the minimum required to make a correct prediction of the optical parameters (10^5). To check whether the different behaviour of the hemodynamics parameters at this ρ depends on a bad estimation of the μ_a and μ_s', the curves have been compacted in step of 20, in order to retrieve the count rate that it would be obtained with 1 s acquisition (about $7 \cdot 10^5$). The result is shown in figure 4.5.

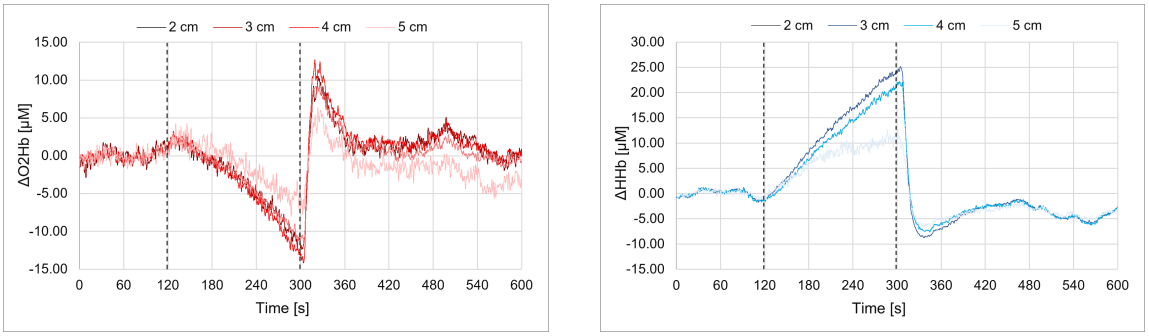

(a) (b)

Figure 4.5: Relative variation of concentration of O_2Hb (a), HHb (b), tHb (c) and SO_2 (d) during the occlusion experiment, in the case of 1 Hz sampling rate. Variations respect to the average value of the parameters in the first 120 s of acquisition in the three stages of measurement: baseline from 0 to 120 s, occlusion from 120 to 300 s and recovery from 300 to 600 s.

Even if, in this case, the curve for 5 cm becomes less noisy, the maximum variation of the hemodynamics parameters is still lower with respect to shorter ρ. A possible explanation about this phenomenon could be provided considering that, when the source detector distance is higher, the collected photons have more probability to have reached higher depths in the tissue, thus the variation of concentration which is displayed could be related to a region which is different from the one reachable by lower interfiber distances. An ecography, performed on the forearm of the volunteer (see fig. 4.6), shows that, in the region between the injection fiber and the ρ=5 cm collection bundle, the investigated tissue appears different in the regions above and below $\sim 2.5cm$.

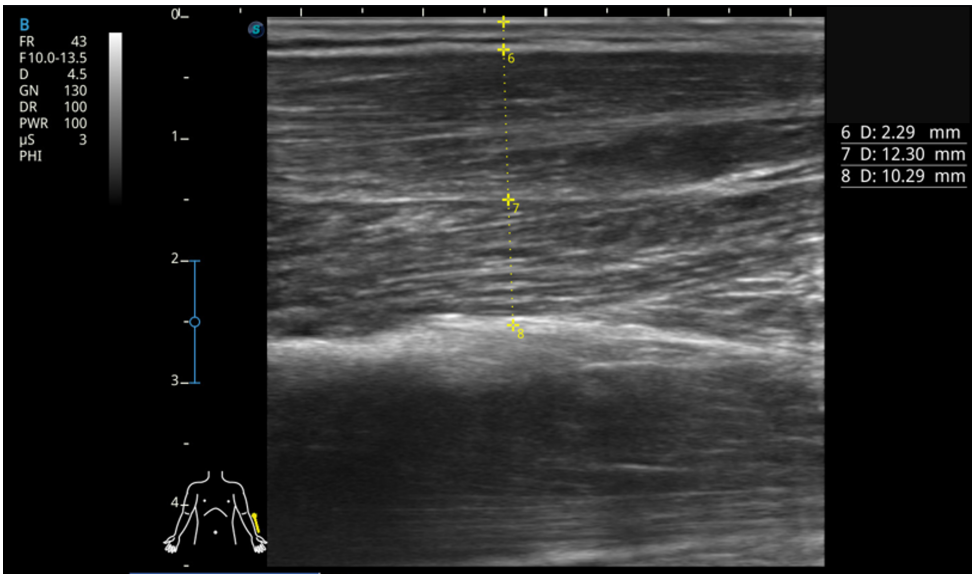

Figure 4.6: Ecography performed on the forearm of the volunteer. The D related to the points labeled as 6,7, and 8 are referred to the relative distance of the corresponding yellow crosses with respect to the previous one.

This clearly shows that there could be an advantage measuring at high interfiber distances (even if at lower sampling rates): it is possible to have a better understanding of parts of the body which are located at high depths ($\sim 2.5cm$).

4.2. Brain cortex

The hemodynamics of the brain motor cortex was followed both in a condition of resting state and during a motor activity.

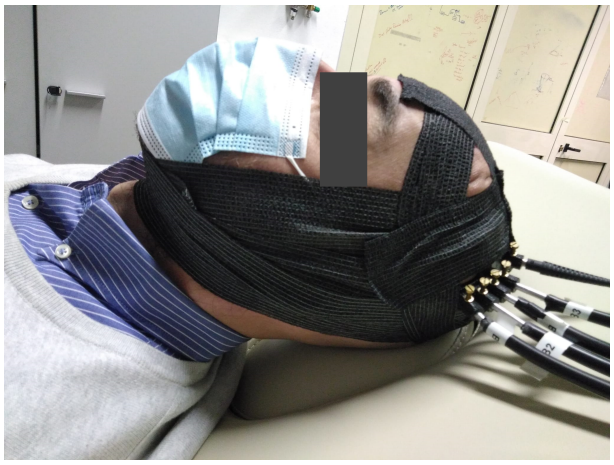

Figure 4.7: Detail of the setup for the occlusion related acquisition.

The volunteer was asked to lie supine and the probe was placed on the scalp in correspondence of the focal point for hand movements (C3 position as defined by 10/20 EEG International System [5]) and fixed at the head through black self-adhesive bandages (fig. 4.7). The total duration of the measurement was 300 s at a sampling rate of 20 Hz. The probe configuration was the same described in section 4.1.2, allowing to reach count rates on the board of about $6 \cdot 10^6$ counts/s for channel 1, $5 \cdot 10^6$ counts/s for channels 2 and 3 and $7 \cdot 10^5$ counts/s for channel 4. To discriminate between the variation of the optical coefficients in superficial layers, such as the scalp, and the ones happening in the brain cortex, the data have been analysed implementing the depth selectivity enhancement method based on the computation of the MPP (described in chapter 1.2.4), making the assumption of having the upper layer of the head 1 cm thick. Then, in order to retrieve the concentrations of the O_2Hb and HHb along with the tHb concentration and SO_2, a MATLAB code implementing the relations of chapter 1.1.3 was used. The results that will be shown are all referred to the region of cortex under the upper layer. As for the muscle acquisition case, the curves that will be shown in the next paragraphs have been filtered through a moving average of order 20.

4.2.1. Resting state

A first acquisition was performed while the subject were still and in absence of any kind of stimuli.

Average baseline values				
ρ	$O_2Hb\,[\mu M]$	$HHb\,[\mu M]$	$tHb\,[\mu M]$	$SO_2\,[\%]$
2 cm	38.0	14.0	52.0	73.1
3 cm	44.6	17.6	62.2	71.6
4 cm	50.4	20.6	71.0	71.0
5 cm	51.0	21.4	72.4	70.5

Table 4.2: Average of the concentration of O_2Hb, HHb, tHb and SO_2 over the first 20 s of resting state for the 4 channels.

Table 4.2 shows the values of the average of the parameters computed in the first 20 s of the resting state acquisition for the 4 channels. Also in this case, the values of oxy, deoxy and total hemoglobin concentrations present an high variability among them. In the case of 1,2 and 3 cm this variability is comparable with the one retrieved for the assessment of the channel homogeneity (chapter 3.5). SO_2, instead, is less variable for all the detection lines, being the ratio between the concentrations of O_2Hb and tHb.

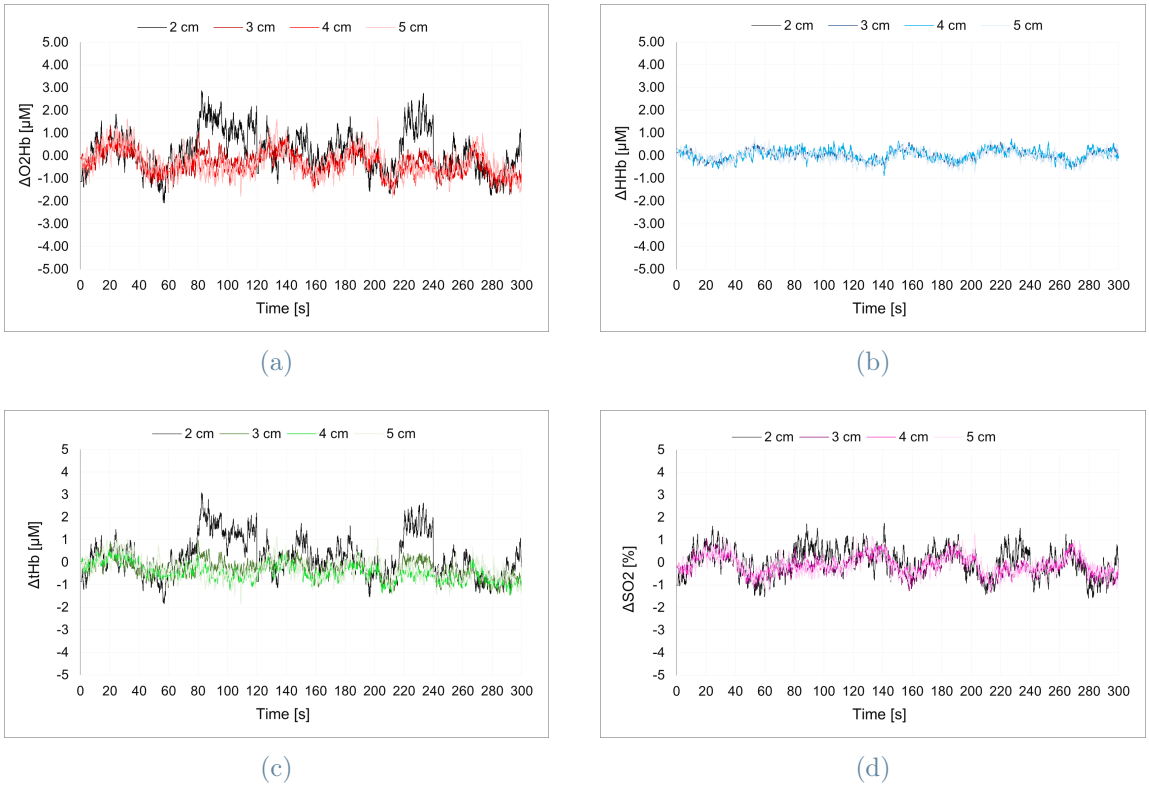

Figure 4.8: Relative variation of concentration of O_2Hb (a), HHb (b), tHb (c) and SO_2 (d) in the brain cortex during the resting state. Variations related to the average value of the parameters in the first 20 s of acquisition.

The black curve of fig. 4.8, relative to ρ=2 cm shows, between 80 and 140 s and 220-240 s a different trend with respect to the other interfiber distance, with wider oscillations. A probable explanation is that the assumed thickness of the superficial part of the head (1 cm) is erroneous, hence, even after the implementation of the method of MPP, the detector at 2 cm is more sensitive to a different region of the head (more superficial) than the detectors placed at higher ρ. Observing fig. 4.8, oscillations of the four signals can be noticed at low frequencies (about 0.02 Hz). These fluctuations are among the ones defined as low frequency oscillations (LFOs), which are below 0.1 Hz, the typical value assumed by the Mayer oscillations. The range of 0.01-0.1 Hz have been broadly observed through the use of functional magnetic resonance imaging (fMRI) approaches and direct current coupled electroencephalographic scalp recording [28] both in the resting state and active-task conditions. Some of them are related to fluctuation of the cardiovascular system or respiration. More studies are being conducted in order to define whether some of the low frequency oscillations are related to neuronal activity [22].

4.2.2. Motor activity

The stimulation of the cortex happened via sequential finger tapping. The activity protocol was composed by 20 s baseline acquisition, 20 s right hand finger tapping and 20 s recovery. This sequence was repeated 5 times for a total duration of the measure of 300 s. Then, the exercise was repeated with the left hand.

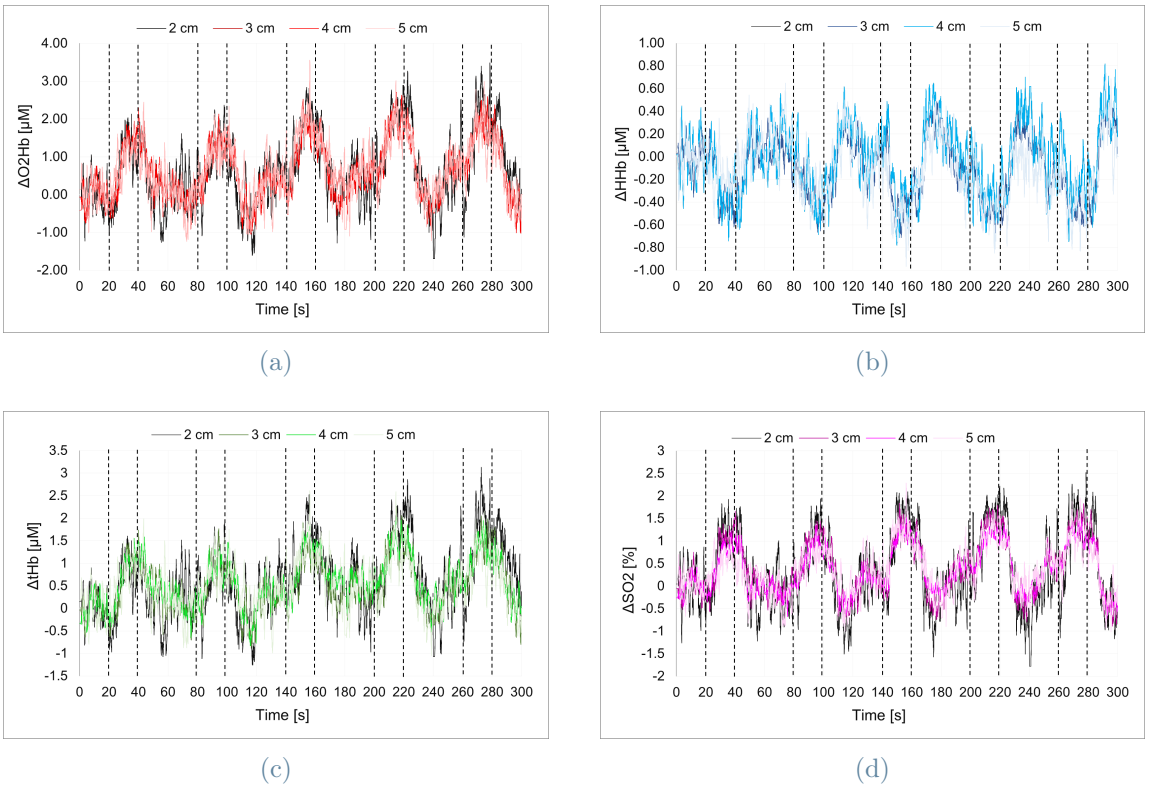

Figure 4.9: Relative variation of concentration of O_2Hb (a), HHb (b), tHb (c) and SO_2 (d) in the brain cortex during the motor stimulation, right hand. Variations related to the average value of the parameters in the first 20 s of acquisition. The sequence is made by a baseline period of 20 s, 20 s of finger tapping and 20 s of recovery repeated for 5 times. The dashed lines represent the start and stop instants of the motor activity.

The hemodynamics response for the finger tapping exercise is shown in fig. 4.9 in terms of variation with respect to the baseline values.

It can be noticed that in the first 20 seconds of each of the five repetitions, the hemodynamics parameters oscillate around the baseline value, hence the Δ is near the 0 value. At the beginning of the finger tapping, the O_2Hb (HHb) starts to increase (decrease) until the stop time. In the plots, the period between start and stop of the motor activity is indicated by vertical dashed black lines. After the motor activity, the value returns to

the baseline in a time of around 20 s. The curves given by each detection channel are well overlapped, thus this confirms the capability of the TD-instrument in the performance at higher interfiber distances.

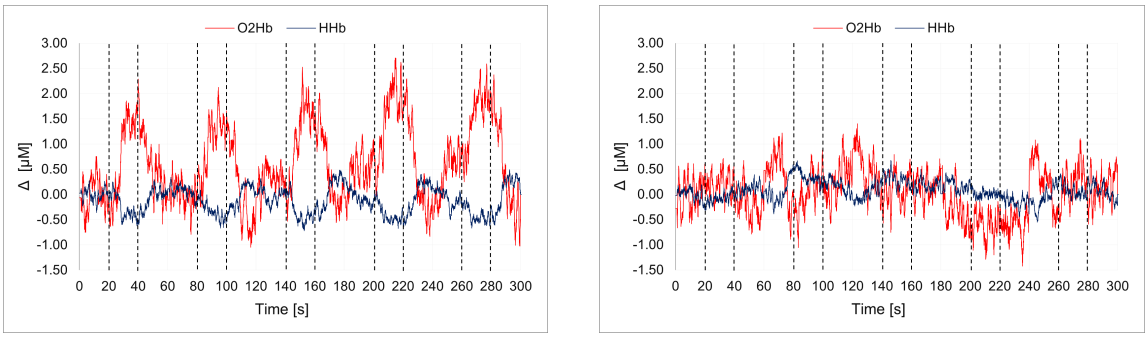

(a) (b)

Figure 4.10: Variation of concentration of O_2Hb, HHb in the left hemisphere of the brain cortex during the finger tapping with the right (a) and left (b) hand. Variations related to the average value of the parameters in the first 20 s of acquisition. The sequence is made by a baseline period of 20 s, 20 s of finger tapping and 20 s of recovery repeated 5 times.The dashed lines represent the start and stop instants of the motor activity.

Being the measurements performed placing the probe on the left hemisfere of the head, the task related hemodynamics variation should be seen only when the movement is performed with the right hand. The volunteer has been asked to repeat the finger tapping exercise both with the right and the left hand. For sake of semplicity, fig. 4.10 shows the only variations in O_2Hb (red curve) and HHb (blue curve) for ρ=3 cm when the motor activity is performed with the right (a) and left hand (b). No task related changes are shown in the curves of fig. 4.10 (b), as expected.
The preliminar measurements in-vivo confirmed the improvements of the system in the acquisitions performed at high interfiber distances (4-5 cm), which makes the device capable of better detecting changes in the hemodynamics related to deeper ($\sim 2cm$) parts of the body. Even if, for $\rho = 5\,cm$ the minimum number of photons (10^5) to have a CV<1% is not reachable at 20 Hz, high sampling frequency acquisitions are possible for $\rho < 5\,cm$. This could be an useful tool to assess oscillations in brain and microcirculation. A recent study by Kacprzak et al. [28] showed how the spectral analysis of the cerebral hemodynamics gives information about the quality of the brain autoregulation, which can show consistent differences in healty subjects and patients with neurovascular disorders.

5 | Conclusion and future perspectives

The first aim of the present work was to overcome the limitations of the setup that was previously developed in the Department of Physics and then to asses its capability to perform high ρ and sampling rate acquisitions. The variations of the experimental setup with respect to the previous configuration were described. The latter caused unwanted reflection peaks due to the position of the circular attenuators of the detection stage and the length of the collection fibers, whose influence caused an incorrect prediction of the absolute values of the optical coefficients. These two elements were the ones to be changed: the detection attenuators were tilted and the collection bundles were re-designed. In particular, plastic graded index optical fibers bundles were chosen since they resulted the best ones in terms of dispersion (few ps) and efficiency with respect to glass fibers for the chosen length (1.25 m) and diameter (3 mm). Moreover, a new set of probes has been designed to perform both on-phantom and in-vivo acquisitions.
In the frame of BIP protocol, where the IRF was evaluated, the length of the fibers of 1.25 m was revealed to solve all the problems of unwanted reflections. Before the improvements, both because of the step index fibers constituting the bundles and the reflection peaks, the IRF of the device's channels showed FWHM values above 330 ps. The improvements of the hardware allowed to retrieve IRF with FWHM values below 252 ps for all the detection channels and both the 690 and 830 nm wavelengths. The BIP protocol showed that the responsivity of the experimental setup in the order of $10^{-8}m^2sr$. The time channel width of the TCSPC resulted to be uniform and the afterpulsing ratio low enough to not compromise the DTOF. The maximum count rate at the detector in order to not have a distorsion of the reflectance curve due to the pile-up error has been found to be 8 millions counts/s. Moreover, it has been shown how it's possible to push the acquisition frequency until 20 Hz with a count rate set to 7 millions counts/s to keep the CV parameter $< 1\%$. To the best of our knowledge, the maximum acquisition rate of the state of the art devices is 10 Hz [6], thus this result constitute an interesting achievement for the presented TD-NIRS device. Among other parameters, through MEDPHOT protocol,

the minimum count rate to reach in order to overcome the noise limitations and to have a CV<1% has been assessed. The minimum count rate for the stated purpose must be 10^5 counts/s on the board. The linearity has been assessed for the 3 cm interfiber distance, no coupling between μ_s' and μ_a has been noticed. The accuracy of the measured values with respect to the conventional ones (measured with a TD-NIRS instrument with a 200 ps IRF) is below 10% for μa and below 20% for $\mu s'$ considering the whole set of phantoms with labels from A to D and from 2 to 8 at $\rho = 3\,cm$. The precise determination of the optical coefficients of all the MEDPHOT phantom series is still an open issue, thus most of the values of accuracy that have been shown in 3.4.5 are referred to an assumption. To better assess this parameter, it will be necessary to re-compute these values according to the real μ_a and μ_s' of the phantoms, once they will all be available. For the phantoms which mimic the optical properties of the human biological tissues, the minimum count rate required to have a consistent measurement and a CV<1% can be reached up to ρ=5 cm, thus confirming the capability of the instrument to perform acquisitions at high interfiber distances, which constitutes an innovation of the TD-NIRS device.
nEUROPt protocol measurements were performed in order to validate the sensitivity of the instrument to deep variation of the absorption coefficient. Variations happening up to $\sim 2\,cm$ depth are detected. As expected, the sensitivity at high depths has been shown to be higher for photons collected at late temporal gates. Since increasing the ρ allows to collect photons that travel longer paths and consequently whose delay for arriving at the detector is longer, performing measurements up to $\rho = 5\,cm$ constitutes an advantage for the depth sensitivity. Preliminar in-vivo measurements on the muscle and brain cortex for both the baseline state and the stimulation or occlusion at sample frequency 20 Hz have been made. Sampling at the latter frequency is possible up to a ρ=4 cm, while at 5 cm the number of collected photons is not enough to overcome the influence of the noise and have a CV<1%. However, after having completed the in-vivo measurements campaign, it has been noticed that the bundle corresponding to $\rho = 5\,cm$ was not firmly fixed to the detection module and this may have caused coupling problems compromising the acquisitions. Further investigations are required to understand whether fixing this problem can improve the count rate at 5 cm interfiber distance.
In the curves related to the hemoglobin concentrations variation during the baseline of the muscle and the resting state of the brain, low frequency oscillations can be appreciated. More in-vivo measurements could be conducted in order to validate in a more robust way the capability of following the hemodynamics at high sampling frequencies and to collect enough data to perform an analysis of the spectrum. This could be done in order to assess via TD-NIRS the frequencies of systemic oscillations due to cerebral autoregulation or neuronal activity in the brain or to better understand the baseline os-

cillation of the muscle hemodynamics. The results of the present thesis show how the TD-NIRS device under analysis alone or combined with other techniques, such as MRI, electroencephalographic scalp recording or ecography can constitute a powerful tool to extract physiological information of the brain and the skeletal muscle.

Bibliography

[1] Alessandro Torricelli, Davide Contini, Antonio Pifferi, Matteo Caffini, Rebecca Re, Lucia Zucchelli, and Lorenzo Spinelli. Time domain functional nirs imaging for human brain mapping. *Neuroimage*, 85:28–50, 2014.

[2] Ileana Pirovano. *Time Domain Near Infrared Spectroscopy for muscle and cerebral oxygenation*. PhD thesis, Politecnico di Milano, Department of Physics, 2020.

[3] URL `https://omlc.org/spectra/hemoglobin/`.

[4] *Light Propagation Through Biological Tissue and Other Diffusive Media: Theory, Solutions, and Software*. Society of Photo Optical, 2010. ISBN 0819476587; 978-0819476586.

[5] Rebecca Re. *Development and applications of a Time Domain Near Infrared Spectroscopy instrument based on wavelength space multiplexing*. PhD thesis, Politecnico di Milano, Department of Physics, 2011.

[6] Frédéric Lange and Ilias Tachtsidis. Clinical brain monitoring with time domain nirs: A review and future perspectives. *Applied Sciences*, 9(8):1612, 2019.

[7] Daniele Contini, Fabrizio Martelli, and Giovanni Zaccanti. Photon migration through a turbid slab described by a model based on diffusion approximation. i. theory. *Applied optics*, 36(19):4587–4599, 1997.

[8] Michael Wahl. Time correlated single photon count. Technical report, PicoQuant GmbH, 2014.

[9] Edinburgh Photonics. What is tcspc? time-correlated single-photon counting. , 2012.

[10] Davide Contini, Lorenzo Spinelli, Alessandro Torricelli, Antonio Pifferi, and Rinaldo Cubeddu. Novel method for depth-resolved brain functional imaging by time-domain nirs. In *European Conference on Biomedical Optics*, page 6629_7. Optical Society of America, 2007.

[11] Lucia Zucchelli, Davide Contini, Rebecca Re, Alessandro Torricelli, and Lorenzo Spinelli. Method for the discrimination of superficial and deep absorption variations by time domain fnirs. *Biomedical optics express*, 4(12):2893–2910, 2013.

[12] Giorgio Migliori. Characterization of a high power time-domain nirs device: towards faster and deeper investigation of biological tissues. Master's thesis, Politecnico di Milano, Italy, 2018-2019.

[13] Govind P. Agrawal. *Fiber-Optic Communications Systems*. John Wiley Sons, Inc., 2002. ISBN 0-471-21571-6 (Hardback); 0-471-22114-7 (Electronic).

[14] Yasuhiro Koike and Kotaro Koike. Progress in low-loss and high-bandwidth plastic optical fibers. *Journal of Polymer Science Part B: Polymer Physics*, 49(1):2–17, 2011.

[15] D. Volpt B. Vojnovic. Notes on optical fibres and fibre bundles, December 2012.

[16] URL `https://www.thorlabs.com/newgrouppage9.cfm?objectgroup_id=358`.

[17] URL `https://www.fiberopticsystems.com/bulk-fiber/`.

[18] URL `https://fiberfin.com/product-category/fiber-cable/`.

[19] Heidrun Wabnitz, Dieter R Taubert, Mikhail Mazurenka, Oliver Steinkellner, Alexander Jelzow, Rainer Macdonald, Daniel Milej, Piotr Sawosz, Michał Kacprzak, Adam Liebert, et al. Performance assessment of time-domain optical brain imagers, part 1: basic instrumental performance protocol. *Journal of biomedical optics*, 19(8):086010, 2014.

[20] Rebecca Re, Davide Contini, Massimo Turola, Lorenzo Spinelli, Lucia Zucchelli, Matteo Caffini, Rinaldo Cubeddu, and Alessandro Torricelli. Multi-channel medical device for time domain functional near infrared spectroscopy based on wavelength space multiplexing. *Biomedical optics express*, 4(10):2231–2246, 2013.

[21] Mauro Buttafava, Edoardo Martinenghi, Davide Tamborini, Davide Contini, Alberto Dalla Mora, Marco Renna, Alessandro Torricelli, Antonio Pifferi, Franco Zappa, and Alberto Tosi. A compact two-wavelength time-domain nirs system based on sipm and pulsed diode lasers. *IEEE Photonics Journal*, 9(1):1–14, 2016.

[22] Xi-Nian Zuo, Adriana Di Martino, Clare Kelly, Zarrar E Shehzad, Dylan G Gee, Donald F Klein, F Xavier Castellanos, Bharat B Biswal, and Michael P Milham. The oscillating brain: complex and reliable. *Neuroimage*, 49(2):1432–1445, 2010.

[23] Antonio Pifferi, Alessandro Torricelli, Andrea Bassi, Paola Taroni, Rinaldo Cubeddu,

Heidrun Wabnitz, Dirk Grosenick, Michael Möller, Rainer Macdonald, Johannes Swartling, et al. Performance assessment of photon migration instruments: the medphot protocol. *Applied optics*, 44(11):2104–2114, 2005.

[24] L Spinelli, A Rizzolo, M Vanoli, M Grassi, PC Eccher Zerbini, A Meirelles de Azevedo Pementel, and A Torricelli. Nondestructive assessment of fruit biological age in brazilian mangoes by time-resolved reflectance spectroscopy in the 540-900 nm spectral range. 2013.

[25] Heidrun Wabnitz, Alexander Jelzow, Mikhail Mazurenka, Oliver Steinkellner, Rainer Macdonald, Daniel Milej, Norbert Żołek, Michał Kacprzak, Piotr Sawosz, Roman Maniewski, et al. Performance assessment of time-domain optical brain imagers, part 2: neuropt protocol. *Journal of biomedical optics*, 19(8):086012, 2014.

[26] Fabrizio Martelli, Antonio Pifferi, Davide Contini, Lorenzo Spinelli, Alessandro Torricelli, Mikhail Mazurenka, Heidrun Wabnitz, Rainer Macdonald, Angelo Sassaroli, Paola Di Ninni, et al. Realistic inhomogeneous phantoms using an equivalent black volume. In *Neurophotonics*, volume 8804, page 88040F. International Society for Optics and Photonics, 2013.

[27] Yunjie Tong, Lia Maria Hocke, Stephanie C Licata, and Blaise deB Frederick. Low-frequency oscillations measured in the periphery with near-infrared spectroscopy are strongly correlated with blood oxygen level-dependent functional magnetic resonance imaging signals. *Journal of biomedical optics*, 17(10):106004, 2012.

[28] Michal Kacprzak, Piotr Sawosz, Wojciech Weigl, Daniel Milej, Anna Gerega, and Adam Liebert. Frequency analysis of oscillations in cerebral hemodynamics measured by time domain near infrared spectroscopy. *Biomedical optics express*, 10(2):761–771, 2019.

List of Figures

List of Tables